

**Ultra High Q Resonators and  
Very Low Phase Noise  
Measurement Systems for Low  
Noise Oscillators**

Simon Jonathan Bale

Thesis submitted for the degree of Doctor of Philosophy

University of York  
Department of Electronics

April 2012

# Abstract

This thesis describes research into ultra high Q Bragg resonators, low phase noise measurement systems and low noise oscillators.

The thesis is divided into three parts. The first is concerned with the modelling, design and implementation of an extremely high quality factor Bragg resonator. This resonator utilises an aperiodic arrangement of non  $\lambda/4$  low loss alumina plates mounted in a cylindrical waveguide. An ABCD parameter waveguide model is developed to simulate and optimise the cavity. The dielectric plates and air waveguide dimensions are optimised using a genetic algorithm to achieve maximum quality factor by redistributing the energy loss within the cavity. An unloaded quality factor ( $Q_0$ ) of 196,000 was demonstrated at 9.93 GHz.

In the second part the design, implementation and measurement results for an ultra-low noise floor cross correlation residual phase noise measurement system are shown. A measurement noise floor of -200 dBc/Hz is achieved for 100,000 correlations. Residual phase noise measurements are also performed on low noise L-Band microwave amplifiers. The key features of the cross correlation technique and the different window functions required during measurement are discussed.

In the third part the residual phase noise performance of several microwave components is evaluated in order to establish their potential utility in a low phase noise oscillator. In the first part of the chapter the designs for a Gallium Nitride (GaN) power amplifier are presented along with the measurements of its noise figure and residual phase noise performance. In the second part of the chapter the designs and performance of an emitter coupled logic (ECL) static digital frequency divider are presented.

# Contents

<b>1</b>	<b>Introduction</b>	<b>14</b>
1.1	Background . . . . .	14
1.2	Thesis Structure . . . . .	15
<b>2</b>	<b>Oscillators and Phase Noise</b>	<b>17</b>
2.1	Feedback Oscillators . . . . .	17
2.2	Negative Resistance Oscillators . . . . .	18
2.3	Ideal Oscillator Characteristics . . . . .	20
2.4	Oscillator Phase Noise . . . . .	21
2.4.1	Thermal Noise . . . . .	23
2.4.2	Shot Noise . . . . .	24
2.4.3	Flicker Noise . . . . .	25
2.4.4	Oscillator Phase Noise Spectrum . . . . .	26
2.5	Oscillator Phase Noise Model . . . . .	27
<b>3</b>	<b>High Q Distributed Bragg Resonator</b>	<b>34</b>
3.1	Microwave Resonators . . . . .	34
3.1.1	The Distributed Bragg Structure . . . . .	35
3.2	ABCD Parameter Model . . . . .	36
3.2.1	Air Section Attenuation . . . . .	38
3.2.2	Dielectric Sections . . . . .	39
3.2.3	Metal End Walls . . . . .	39
3.2.4	Periodic Resonator Simulation . . . . .	41
3.3	Resonator Optimisation . . . . .	44
3.3.1	Genetic Algorithm . . . . .	45
3.3.1.1	Genotype Encoding . . . . .	46
3.3.1.2	Selection Operator . . . . .	46
3.3.1.3	Crossover and Mutation . . . . .	47
3.3.1.4	Fitness Function . . . . .	48

3.3.2	Optimised Aperiodic Resonator . . . . .	50
3.4	Measurement Results . . . . .	54
3.4.1	Tuneable Bragg Resonator . . . . .	57
3.5	Numerical Field Solver . . . . .	59
3.5.1	The Body of Revolution FD-TD Algorithm . . . . .	60
3.5.2	Quality Factor Computation . . . . .	62
3.5.3	Simulation Procedure . . . . .	64
3.5.4	Simulator Verification . . . . .	67
3.5.5	Periodic Bragg Resonator Field Simulation . . . . .	72
3.5.6	aPeriodic Bragg Resonator Field Simulation . . . . .	76
<b>4</b>	<b>Cross Correlation Residual Phase Noise Measurement System</b>	<b>82</b>
4.1	Introduction . . . . .	82
4.2	Residual Phase Noise Measurement . . . . .	83
4.3	The Cross Correlation Technique . . . . .	86
4.3.1	Data Windowing . . . . .	87
4.4	Measurement Apparatus . . . . .	91
4.4.1	System Calibration . . . . .	93
4.5	System Noise Floor Measurements . . . . .	95
4.6	Low Noise Amplifier Measurements . . . . .	100
4.7	Conclusions . . . . .	104
<b>5</b>	<b>Residual Phase Noise Measurements of Microwave Components</b>	<b>105</b>
5.1	Gallium Nitride Amplifier . . . . .	105
5.1.1	Amplifier Design . . . . .	106
5.1.2	Measured Performance . . . . .	110
5.1.3	Residual Phase Noise Measurement . . . . .	112
5.2	Digital Frequency Divider . . . . .	114
5.2.1	Residual Phase Noise Measurements . . . . .	119
<b>6</b>	<b>Conclusions and Further Work</b>	<b>122</b>
6.1	High Q Distributed Bragg Resonator . . . . .	122
6.2	Cross Correlation . . . . .	123
6.3	Residual Phase Noise Measurements of Microwave Components	124
6.4	General Research Recommendations . . . . .	124
<b>A</b>	<b>List of Publications</b>	<b>133</b>

# List of Figures

2.1	Simplified Positive Feedback Oscillator . . . . .	17
2.2	Negative resistance oscillator model . . . . .	19
2.3	Ideal oscillator spectrum. . . . .	20
2.4	Typical oscillator spectrum. . . . .	20
2.5	Oscillator Output - Power Spectral Density . . . . .	22
2.6	Thévenin and Norton Equivalent Circuits for a Noisy Resistor .	24
2.7	Simplified noise model of a Silicon Bipolar transistor. . . . .	25
2.8	Typical residual phase noise plot for a silicon bipolar transistor amplifier with a 40 kHz flicker noise corner. . . . .	25
2.9	Typical oscillator phase noise spectrum. . . . .	26
2.10	Equivalent circuit model for an oscillator. . . . .	27
3.1	The structure of a periodic Bragg reflector resonator. The di- electric plates and air sections are one quarter of the guide wave- length in thickness, where $\lambda_{ga}$ and $\lambda_{gd}$ are the guide wavelength in air and dielectric respectively. . . . .	35
3.2	A 2-Port network represented using ABCD parameters. . . . .	37
3.3	A cascade connection of two 2-Port network represented using ABCD parameters. . . . .	37
3.4	A waveguide ABCD parameter model for a two plate periodic Bragg resonator. . . . .	41
3.5	An aperiodic Bragg resonator consisting of two identical dis- tributed Bragg reflectors. The widths of the dielectric and air sections can be optimised in order to maximise the magnitude of the input reflection coefficient ( $\Gamma_{in}$ ) . . . . .	44
3.6	Bragg resonator genotype encoding, three bit sub-strings are shown in this figure. The actual optimisation algorithm used 26 bit sub-strings for increased accuracy. . . . .	46

3.7	A single point crossover operation applied to a pair of binary strings. All data beyond the crossover point is swapped. . . . .	47
3.8	Flowchart for the genetic algorithm used to optimise the input reflection coefficient of the Bragg reflectors. . . . .	49
3.9	A waveguide ABCD parameter model for one half of a six plate Bragg resonator. The length of the air and dielectric sections of this s structure are optimised to maximise the magnitude of the input reflection coefficient ( $S_{11}$ ). . . . .	50
3.10	Voltage standing wave distribution inside the 6 plate periodic Bragg resonator. . . . .	53
3.11	Voltage standing wave distribution inside the 6 plate aperiodic Bragg resonator. . . . .	53
3.12	A cross section view of the six plate aperiodic Bragg resonator .	54
3.13	A-periodic Bragg resonator with the lid removed. . . . .	54
3.14	A plot of the forward transmission coefficient ( $S_{21}$ ) for the 6 plate aperiodic Bragg resonator. A frequency span of 1 GHz is shown. . . . .	55
3.15	A narrow band plot of the forward transmission coefficient ( $S_{21}$ ) for the 6 plate aperiodic Bragg resonator. A frequency span of 500 kHz is shown. . . . .	56
3.16	Quality factor and resonant frequency for the $TE_{011}$ mode in the 6-plate aperiodic Bragg resonator as a function of the central section length. . . . .	57
3.17	Tuneable distributed Bragg resonator. . . . .	58
3.18	Tuneable distributed Bragg resonator with the lid removed. Micrometers were used to tune the length of the central section. . .	58
3.19	The finite difference mesh for BOR computations . . . . .	61
3.20	Frequency domain (Top) and time domain (Bottom) plots of a Gaussian modulated sine signal as described by equations (3.5.13) and (3.5.14) . . . . .	64
3.21	Frequency response of the air filled cylindrical cavity after 262,144 iterations. . . . .	68
3.22	Plot of the magnitude of the $E_\phi$ field inside the air filled cylindrical cavity resonator at 10 GHz. . . . .	69
3.23	Plot of the magnitude of the $H_r$ field inside the air filled cylindrical cavity resonator at 10 GHz. . . . .	69

3.24	Plot of the magnitude of the $H_z$ field inside the air filled cylindrical cavity resonator at 10 GHz. . . . .	70
3.25	Simulated quality factor of the air filled cylindrical cavity resonator. The Q factor was calculated using the perturbation method at each iteration of the BOR solver. . . . .	70
3.26	Frequency response of the periodic Bragg resonator after 100,000 iterations. . . . .	72
3.27	Simulated quality factor of the periodic Bragg resonator. The Q factor was calculated using the perturbation method at each iteration of the BOR solver. . . . .	73
3.28	Plot of the magnitude of the $E_\phi$ field inside the periodic Bragg resonator at 10 GHz. . . . .	74
3.29	Plot of the magnitude of the $H_r$ field inside the periodic Bragg resonator at 10 GHz. . . . .	74
3.30	Plot of the magnitude of the $H_z$ field inside the periodic Bragg resonator at 10 GHz. . . . .	75
3.31	Line plot of the magnitude of the $E_\phi$ field along the axis of the periodic Bragg resonator . . . . .	75
3.32	Frequency response of the aperiodic Bragg resonator after 100,000 iterations. . . . .	76
3.33	Simulated quality factor of the aperiodic Bragg resonator. The Q factor was calculated using the perturbation method at each iteration of the BOR solver. . . . .	77
3.34	Plot of the magnitude of the $E_\phi$ field inside the aperiodic Bragg resonator at 10 GHz. . . . .	78
3.35	Plot of the magnitude of the $H_r$ field inside the aperiodic Bragg resonator at 10 GHz. . . . .	78
3.36	Plot of the magnitude of the $H_z$ field inside the aperiodic Bragg resonator at 10 GHz. . . . .	79
3.37	Line plot of the magnitude of the $E_\phi$ field along the axis of the aperiodic Bragg resonator . . . . .	79
3.38	Normalised plots of the voltage standing wave distribution predicted by the ABCD model (green trace) and the magnitude of the $E_\phi$ field along the axis of the aperiodic Bragg resonator (blue trace) . . . . .	80

3.39	Normalised plots of the voltage standing wave distribution predicted by the ABCD model (green trace) and the magnitude of the $E_\phi$ field along the axis of the periodic Bragg resonator (blue trace) . . . . .	81
4.1	A Simplified single channel residual phase noise measurement system. . . . .	84
4.2	Simplified cross correlation residual phase noise measurement system. . . . .	86
4.3	Time domain (top) and Frequency domain (bottom) plots for a 64 point flat-top window as defined in (4.3.6) . . . . .	89
4.4	Time domain (top) and Frequency domain (bottom) plots for a 64 point rectangular window as defined in (4.3.7) . . . . .	90
4.5	Time domain (top) and Frequency domain (bottom) plots for a 64 point Hann window as defined in (4.3.8) . . . . .	91
4.6	Cross correlation residual phase noise measurement system including calibration components. . . . .	92
4.7	A photograph of cross correlation residual phase noise measurement system. . . . .	93
4.8	Cross correlation phase noise measurement system showing the additional components required to artificially increase the system noise floor. This arrangement was used to check the validity of the calibration technique. . . . .	94
4.9	Equipment configuration used to measure the noise floor of measurement system . . . . .	95
4.10	Residual phase noise floor of the cross correlation measurement system after 1000 cross correlations. This measurement was made with a resolution bandwidth of 7.63Hz . . . . .	97
4.11	Residual phase noise floor of the cross correlation measurement system after 10000 cross correlations. This measurement was made with a resolution bandwidth of 7.63Hz . . . . .	98
4.12	Residual phase noise floor of the cross correlation measurement system after 100,000 cross correlations. This measurement was made with an increased resolution bandwidth of 122.07 Hz in order to reduce the measurement time. . . . .	99

4.13	Residual phase noise floor of the 1.25 GHz medium power silicon amplifier after 100 cross correlations. The blue and red (upper) traces are the noise floors for each independent channel and the green (lower) trace is the dual channel cross correlated noise floor	101
4.14	Residual phase noise floor of the 1.25 GHz medium power silicon amplifier after 1000 cross correlations. The blue and red (upper) traces are the noise floors for each independent channel and the green (lower) trace is the dual channel cross correlated noise floor	102
4.15	Residual phase noise floor of the 1.25 GHz medium power silicon amplifier after 5000 cross correlations. The blue and red (upper) traces are the noise floors for each independent channel and the green (lower) trace is the dual channel cross correlated noise floor	103
5.1	Bias circuit used to measure the S-Parameters of the CGH40010 GaN transistor. The bias conditions were $V_{DS} = 28 V$ , $I_D = 200 mA$ and $V_{GS} = -2.1 V$	106
5.2	Single stub matching network for the CGH40010 GaN transistor.	108
5.3	CGH40010 power amplifier circuit including biasing components.	108
5.4	Photograph of the CGH40010 power amplifier.	109
5.5	Simulated S-Parameters for the CGH40010 power amplifier circuit.	109
5.6	Frequency Response of GaN Power Amplifier - A 1 GHz span is shown.	110
5.7	Frequency Response of GaN Power Amplifier - A 2.5 GHz span is shown.	110
5.8	Noise figure measurement system.	111
5.9	Residual phase noise measurements of the CGH40010 GaN power amplifier. The purple trace shows the estimated thermal noise floor and the blue trace shows the extrapolated $1/f$ residual phase noise characteristic.	113
5.10	Simplified static frequency divider	114
5.11	Simplified emitter coupled logic (ECL) inverter	115
5.12	Simplified ECL D-Latch	116
5.13	Simplified ECL frequency divider schematic	117
5.14	Discrete ECL frequency divider schematic	118
5.15	Digital divider residual phase noise measurement system	119

5.16 Discrete ECL digital divider residual phase noise measurements.  
The blue trace shows the noise floor of the measurement system.  
The green trace shows the divider phase noise with an input  
frequency of 192 MHz and the purple trace shows the divider  
phase noise with an input frequency of 443 MHz . . . . . 121

# List of Tables

2.1	Oscillator Noise Modelling Parameters . . . . .	28
3.1	Model parameters for a cylindrical periodic Bragg resonator. The resonator has silver plated walls and operates with the $TE_{011}$ mode at 10 GHz . . . . .	42
3.2	The simulated unloaded quality factor ( $Q_0$ ) for periodic Bragg resonators with varying numbers of dielectric plates. . . . .	43
3.3	Dielectric and air section reflector thicknesses for an optimised six plate Bragg resonator. . . . .	50
3.4	Genetic algorithm parameters used during the six plate Bragg resonator optimisation. The mutation probability was calculated using equation (3.3.2). . . . .	51
3.5	Dielectric and air section reflector thicknesses for an optimised eight plate Bragg resonator. . . . .	52
3.6	Quality factor and resonant frequency for the $TE_{011}$ mode in the 6-plate aperiodic Bragg resonator as a function of the central section length. . . . .	57
3.7	Specification for an air filled cylindrical resonator cavity with silver plated walls operating with the $TE_{011}$ mode at 10 GHz . .	68
3.8	BOR field solver simulation parameters for the periodic Bragg resonator. . . . .	72
3.9	BOR field solver simulation parameters for the periodic Bragg resonator. . . . .	76
4.1	The coefficients, $a_0$ to $a_4$ for the Flat-Top window function specified in equation (4.3.6). . . . .	88
4.2	Residual phase noise floor of the cross correlation measurement system at a 20kHz offset from a carrier frequency of 1.25 GHz. .	96

List of Tables

---

5.1	S-Parameters for the CGH40010 GaN transistor at 10 GHz with $V_{DS} = 28 V$ and $I_D = 200 mA$ . . . . .	107
5.2	Noise figure measurements for the CGH40010 GaN power amplifier with a drain source voltage of $V_{DS} = 28 V$ . . . . .	111
5.3	Truth Table for the circuit in figure 5.12 . . . . .	117

# Acknowledgements

There are many people whom I wish to thank for their knowledge, support and encouragement:

My Supervisor, Professor Jeremy Everard, for the valuable support, constructive feedback and experience he has offered throughout this work.

My friend and fellow PhD student, Konstantinos Theodoropoulos, for his support and encouragement as well as the lengthy discussions we had about various research topics.

I thank my parents and my brother Alex as without your support and constant reminders to persevere and keep writing, I would never have managed to write this thesis.

Finally, a very special thank you to Leanne as without your continued support, patience, understanding and keeping me sane, I would not have completed this work.

# Declaration

This thesis is the work of the Author except where indicated. References and acknowledgements to other authors have been given where appropriate. The following publications have resulted as part of this work:

## Journal Publications

S. Bale and J. Everard, "High-Q X-band distributed Bragg resonator utilizing an aperiodic alumina plate arrangement," *IEEE Trans. Ultrason. Ferroelectr. Freq. Control*, vol.57, no.1, pp.66-73, Jan. 2010.

## Conference Publications

Simon. Bale, D. Adamson, B. Wakley, J. Everard, "Cross Correlation Residual Phase Noise Measurements using Two HP3048A Systems and a PC Based Dual Channel FFT Spectrum Analyser," presented at the *European Frequency and Time Forum Conference.*, Noordwijk, Netherland, 2010.

S. Bale and J. Everard, "High Q X-band distributed Bragg resonator utilising an aperiodic alumina plate arrangement," in *Frequency Control Symposium, 2009 Joint with the 22nd European Frequency and Time forum. IEEE International.*, Besancon, France, 2009, pp.232-236.

# Chapter 1

## Introduction

### 1.1 Background

An oscillator forms an integral part of many analogue and digital electronic systems. They are used in RADARS and communication systems as a reference for the modulation and demodulation of signals, in test and measurement equipment and in many consumer products. In many systems the oscillator characteristics set the performance and accuracy limits of the system. For example, in a digital communication system any deviation in the oscillator frequency will result in an increased bit error rate (BER) [1]. In a Doppler RADAR close to carrier noise can reduce the ability of the system to detect slow moving targets [2] [3]. In a digital PLL frequency synthesiser, the frequency multiplication process results in the multiplication of the reference oscillator phase noise by a factor of  $20 \log_{10}(N) \text{ dB}$  [4], where  $N$  is the multiplication factor. This can limit the maximum usable frequency of the synthesiser.

The most important characteristic of an oscillator is its frequency stability. Frequency stability can be split into two categories, long-term stability and short-term stability. Long term stability manifests as a gradual drift in the frequency of the oscillator. It is commonly caused by temperature variations that modify the operating points of the various components or by ageing of the devices in a system [5]. Short-term stability is a function of the noise signals within the oscillator which result in phase and amplitude modulation of the output signal. This modulation is a result of the additive noise from the passive components in the oscillator as well as the transposition of low frequency ( $1/f$ ) noise from the amplification devices to the carrier signal [6].

A simple model for the feedback oscillator noise spectrum was initially

described by Leeson [7]. His model states that within the 3 dB bandwidth of the resonator the oscillator phase noise spectrum can be considered to be a multiplication of the amplifier phase noise by a factor of  $1/\Delta f^2$ . He shows that the phase noise level is inversely proportional to the unloaded quality factor of the frequency selective element. In a later model Everard [8] also describes the noise performance of an oscillator but he incorporates additional circuit parameters such as the oscillator loop power, resonator loaded quality factor and amplifier input and output impedances. These parameters were not included in the original theory as described by Leeson. Everard goes on to show that there is an optimal resonator insertion loss for minimum phase noise. These theories demonstrate that in order to produce a low phase noise oscillator it is desirable to have a high Q resonator and a low residual noise amplifier capable of delivering a high power level into the frequency selective element.

The main objectives of this thesis are the development of high Q resonators and low phase noise measurement systems for use in low noise oscillators.

## 1.2 Thesis Structure

The thesis is organised as follows. Chapter 2 provides a general introduction to oscillator theory and phase noise. In this section the background and underlying principles for the design of low phase noise oscillators are discussed. Everard's [8] linear theory describing the generation of phase noise in an oscillator is presented. The equations derived in this theory show which parameters explicitly affect the noise performance of an oscillator.

Chapter 3 is concerned with the modelling, design and implementation of an extremely high quality factor Bragg resonator. An ABCD parameter waveguide model is developed that allows the performance of both periodic and aperiodic Bragg resonators to be rapidly evaluated. A genetic algorithm is then used to optimise the quality factor of the resonator and the measurement results for a 10 GHz aperiodic design are presented. In the final part of the chapter a finite difference time domain, body of revolution (FDTD-BOR) field solver is presented. This solver uses perturbation theory to allow the rapid simulation of the cavity field structure and quality factor.

In chapter 4 the design, implementation and measurement results for an ultra-low noise floor cross correlation residual phase noise measurement system are shown. A measurement noise floor of -200 dBc/Hz is achieved for 100,000

correlations. Residual phase noise measurements are also performed on low noise L-Band microwave amplifiers. The key features of the cross correlation technique and the different window functions required during measurement are discussed.

In chapter 5 the residual phase noise performance of several microwave components is evaluated in order to establish their potential utility in a low phase noise oscillator. In the first part of the chapter the designs for a Gallium Nitride (GaN) power amplifier are presented along with the measurements of its noise figure and residual phase noise performance. In the second part of the chapter the designs and performance of an emitter coupled logic (ECL) static digital frequency divider are presented.

Finally, concluding remarks and observations are given in Chapter 6. Future areas of research are also suggested for each of the topics described in this thesis.

# Chapter 2

## Oscillators and Phase Noise

### 2.1 Feedback Oscillators

There are several techniques that can be used to construct an oscillator. These include destabilising a transistor with a negative impedance or the use of positive feedback through a frequency selective element. A block diagram illustrating a positive feedback oscillator is shown in 2.1.

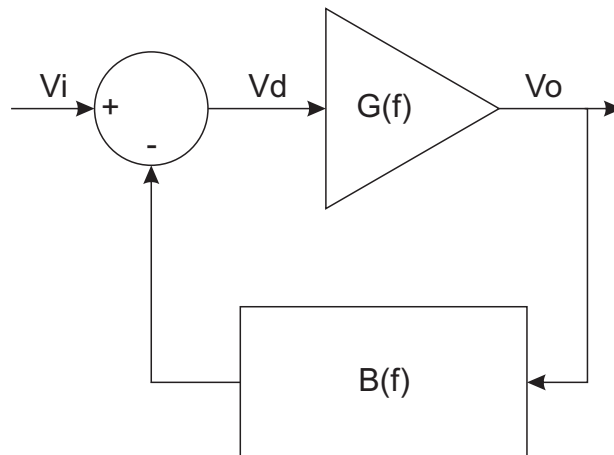


Figure 2.1: Simplified Positive Feedback Oscillator

The voltage transfer function of this circuit can be obtained by considering equations (2.1.1) and (2.1.2)

$$V_o = V_d G(f) \quad (2.1.1)$$

$$V_d = V_i - [V_o B(f)] \quad (2.1.2)$$

If we substitute (2.1.2) into (2.1.1) and re-arrange then we can write equation (2.1.3):

$$\frac{V_o}{V_i} = \frac{G(f)}{1 + [B(f)G(f)]} \quad (2.1.3)$$

This equation can also be written in the form shown in (2.1.4):

$$V_o = \left( \frac{G(f)}{1 + [B(f)G(f)]} \right) V_i \quad (2.1.4)$$

If a stable oscillation is occurring then an output voltage  $V_o$  will be present even if no input signal is applied. This can only happen if the amplifier gain becomes infinite or if the loop gain,  $1 + [B(f)G(f)]$ , becomes equal to unity at some frequency. These conditions can be stated mathematically as the Barkhausen criteria [9]:

$$|B(f)G(f)| = 1 \quad (2.1.5)$$

$$\text{Arg}[B(f)G(f)] = 2\pi n \text{ where } n = 0, 1, 2, \dots \quad (2.1.6)$$

The first condition, equation (2.1.5), states that at the frequency of operation, the gain of the amplifier,  $G(f)$ , must be sufficient to compensate for the losses in the feedback element,  $B(f)$ . The second condition, equation (2.1.6), states that the open loop phase shift must be an integer multiple of  $360^\circ$ . In order for an oscillation to start there must be an initial disturbance in the feedback loop, this is usually caused by the thermal noise present in the oscillator components. At start up the loop gain is greater than one and the thermal noise is amplified and filtered by the loop. In order for a stable and finite oscillation to occur the power circulating inside the loop must eventually saturate and the loop gain will reach unity. Typically, in electronic systems, the gain is provided by a transistor whose saturation characteristics define the operating point of the oscillator.

## 2.2 Negative Resistance Oscillators

A two port network can be said to exhibit negative impedance when an increase in current entering a port results in a decrease in the voltage across the same port. A network element that exhibits negative resistance can be said to be capable of injecting energy into an electrical circuit. This useful characteristic can be used to construct an oscillator.

A simple model of a negative resistance oscillator is shown in figure 2.2. An

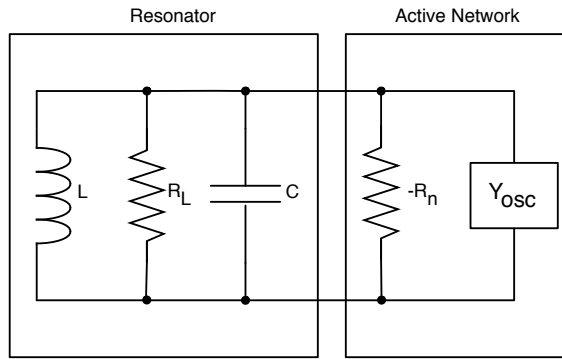


Figure 2.2: Negative resistance oscillator model

active network that exhibits a negative resistance is easily created by destabilising a transistor or by using a Gunn diode. For a stable oscillation to occur, the following conditions must be true when steady state is reached:

$$R_L = -R_n \quad (2.2.1)$$

$$-Y_{OSC} = \frac{1}{j\omega L} + j\omega C \quad (2.2.2)$$

These criteria are analogous to the Barkhausen criteria described previously. It is clear from these equations that for a stable oscillation to occur the active network must produce a negative resistance that is equal to the loss resistance,  $R_L$ , of the resonator. The operating frequency of the oscillator is defined by the frequency at which the susceptance of the resonator and active network cancel each other. At turn on the signal amplitude is small and the negative resistance of the active device is larger than the loss resistance of the resonator. As the signal amplitude increases the negative resistance decreases and when equilibrium is reached a stable oscillation occurs.

## 2.3 Ideal Oscillator Characteristics

An ideal oscillator will produce an output signal with all of its energy confined to a single frequency. The frequency spectrum of such a signal will consist of a single tone with infinitely narrow bandwidth (discrete spectral line), centred at the operating frequency of the oscillator,  $f_0$ . Figure 2.3 shows the spectrum of an ideal oscillator.

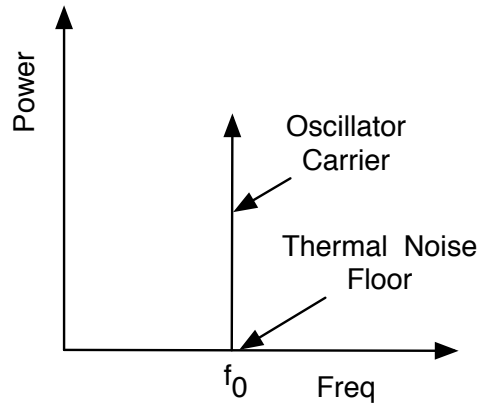


Figure 2.3: Ideal oscillator spectrum.

Unfortunately it is not possible to build an oscillator with these characteristics. Due to random phase and amplitude fluctuations inside the oscillator loop the output signal will also be phase and amplitude modulated which will result in noise sidebands. The frequency spectrum of a real oscillator will also contain a large number of harmonics which are a result of the non-linearities present in the amplification devices. The typical output spectrum of a non-ideal oscillator is shown in figure 2.4

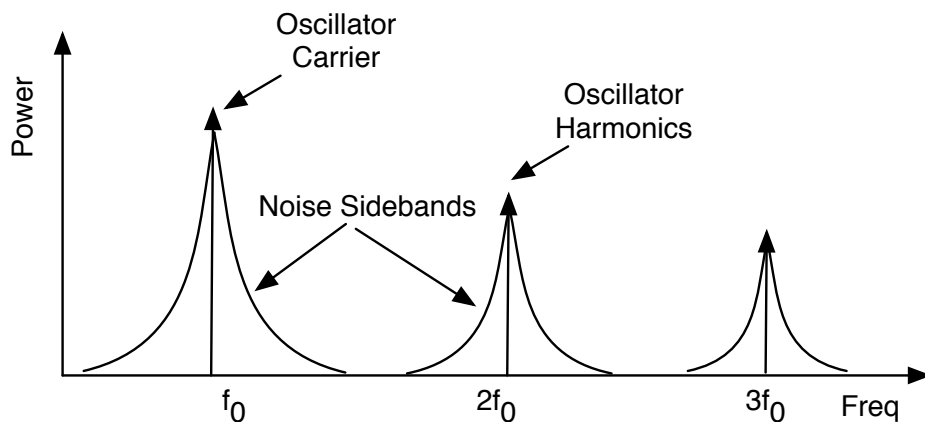


Figure 2.4: Typical oscillator spectrum.

## 2.4 Oscillator Phase Noise

Frequency stability can be split into two categories, long-term stability and short-term stability. Long term stability manifests as a gradual drift in the frequency of a waveform. It is commonly caused by temperature variations that modify the operating points of the various components or by ageing of the devices in a system, particularly the resonator [5]. Short-term stability is a function of the noise signals within the system and results in a phase and amplitude modulation of the output waveform. This modulation is a result of the additive noise from the passive components in the oscillator as well as the transposition of low frequency ( $1/f$ ) noise from the amplification devices to the carrier signal[6].

The output signal of a noisy oscillator can be modelled using equation (2.4.1):

$$V(t) = A_0(1 + \epsilon(t)) \cos(2\pi f_0 t + \phi(t)) \quad (2.4.1)$$

where,  $\epsilon(t)$  represents the random amplitude variation as a function of time (AM Noise) and  $\phi(t)$  represent the random phase variation (PM Noise). In an oscillator the amplitude instabilities are greatly suppressed by the limiting characteristics of the amplification devices and we can therefore set  $\epsilon(t) = 0$ . If we also assume that  $\phi(t) \ll 1$  then we can represent a small change in the instantaneous frequency of the oscillator by frequency modulating the phase term,  $\phi(t)$ , of the carrier using equation (2.4.2):

$$\phi(t) = \phi_p \sin(2\pi f_m t) \quad (2.4.2)$$

where  $\phi_p$  represents the modulation index. If we substitute (2.4.2) into (2.4.1) then we can write:

$$V(t) = A_0 [\cos(2\pi f_0 t) \cos(\phi_p \sin(2\pi f_m t)) - \sin(2\pi f_0 t) \sin(\phi_p \sin(2\pi f_m t))] \quad (2.4.3)$$

as we are assuming that  $\phi_p \ll 1$  then the small angle approximations  $\sin(x) \approx x$  and  $\cos(x) \approx 1$  can be used to simplify equation (2.4.3) giving:

$$V(t) = A_0 [\cos(2\pi f_0 t) - \phi_p \sin(2\pi f_m t) \sin(2\pi f_0 t)] \quad (2.4.4)$$

Using the trigonometric identity,  $\sin \alpha \sin \beta = \frac{1}{2} [\cos(\alpha - \beta) - \cos(\alpha + \beta)]$ , equa-

tion (2.4.4) can be expanded as:

$$V(t) = A_0 \left[ \cos(\omega_0 t) - \frac{\phi_p}{2} (\cos([f_0 + f_m]t) - \cos([f_0 - f_m]t)) \right] \quad (2.4.5)$$

Equation (2.4.4) shows that any small phase or frequency changes in the output of the oscillator will result in modulation side-bands at frequencies of  $(f_0 + f_m)$  and  $(f_0 - f_m)$ . It is these sidebands that are referred to as the phase noise. If the phase and frequency deviations are the result of a random process such as noise then the oscillator spectrum will take the form shown in figure 2.5.

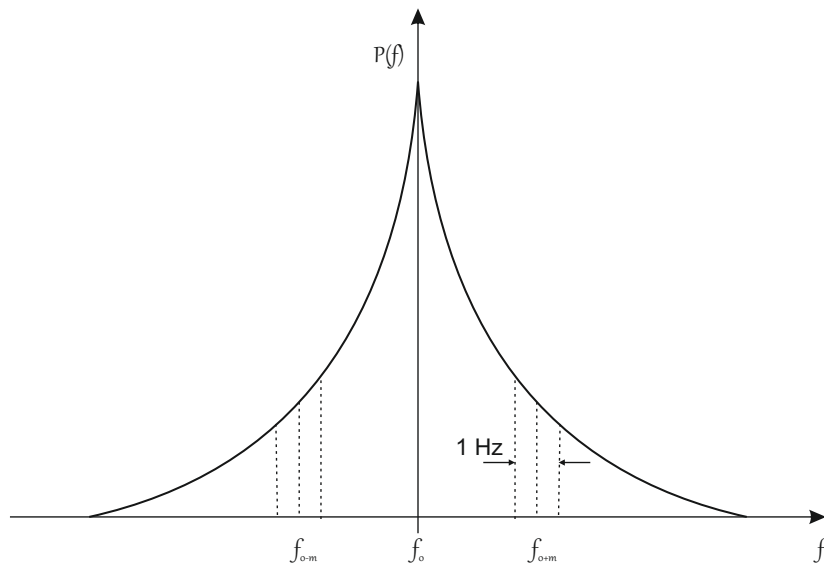


Figure 2.5: Oscillator Output - Power Spectral Density

The standard measure for characterising frequency and phase instabilities in the frequency domain is  $\mathcal{L}(f)$ , defined as one half of the double sideband spectral density of phase fluctuations[10]. Phase noise is measured as the ratio of the single side-band phase noise power in a 1Hz bandwidth, at a given offset frequency, to the total carrier power. With reference to equation (2.4.5) the ratio of the RMS noise power in a single sideband to the total RMS power in the carrier can be expressed as:

$$L(f) = \frac{P_n}{P_c} = \frac{\frac{1}{2} \left( \frac{A_0 \phi_p}{2} \right)^2}{\frac{1}{2} A_0^2} = \frac{\phi_p^2}{4} = \frac{\phi_{rms}^2}{2} \quad (2.4.6)$$

where  $\phi_{rms}$  is equal to  $\frac{\phi_p}{\sqrt{2}}$ . Since the power spectral density distribution is symmetric about the carrier frequency then the double side-band noise power,

$S_\phi(f_m)$ , is equal to:

$$S_\phi(f_m) = 2P_\phi(f_m) = \frac{\theta_p^2(f_m)}{2} \quad (2.4.7)$$

$$\mathcal{L}(f_m) = \frac{1}{2}S_\phi(f_m) \quad (2.4.8)$$

Phase noise is usually expressed in decibels and its units are dBc/Hz, dB below the carrier in 1 Hz bandwidth. There are several types of noise source that can be identified as causing the phase noise and these are described in the following subsections.

### 2.4.1 Thermal Noise

Thermal noise is the result of the random interaction of charge carriers with the lattice atoms of a conducting material. The noise has a Gaussian probability density function (PDF) [11] with a spectral density of:

$$S_t(f) = 4kTR \text{ V}^2/\text{Hz} \quad (2.4.9)$$

where  $k$  is Boltzmann's constant ( $1.38 \times 10^{-23}$  J/K),  $T$  is the ambient temperature in Kelvin and  $R$  is the resistance of the conductor. Equation (2.4.9) shows that the thermal noise is independent of frequency and we can therefore model the thermal noise in a bandwidth  $B$  as an RMS noise voltage, given by:

$$e_n = \sqrt{4kTRB} \text{ V} \quad (2.4.10)$$

It can be seen from equation (2.4.10) that as the measurement bandwidth approaches infinity so will the available thermal noise power. Obviously this can not be the case and at very high frequencies quantum effects must be considered. As described in [12] these can be incorporated into equation (2.4.10) by replacing the  $kT$  term with:

$$(kT') = hf/kT \left[ \exp\left(\frac{hf}{kT}\right) - 1 \right]^{-1} \quad (2.4.11)$$

where  $h$  is Planck's constant ( $6.626 \times 10^{-34}$  J sec). For  $f \ll kT$  equation (2.4.11) approaches  $kT' \approx kT$ . At room temperatures this approximation is valid at frequencies up to  $10^{13}$  Hz.

The thermal noise generated by a resistive impedance is typically modelled using a Thévenin or Norton equivalent circuit where the noisy resistance is

replaced with a noiseless component in combination with a noisy voltage or current source as show in figure 2.6:

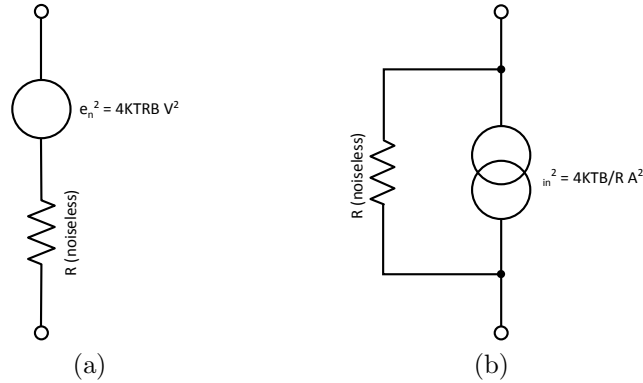


Figure 2.6: Thévenin and Norton Equivalent Circuits for a Noisy Resistor

### 2.4.2 Shot Noise

The current inside a conductor is the result of the summed motion of a large number of discrete and independent charged particles. Current does not flow uniformly as is typically imagined and if we were to count the number of particles passing a fixed point in a unit time interval then we would find that the total would vary from one interval to the next. Unlike thermal noise, shot noise is only found in the presence of a direct current flow. It is not usually possible to observe the shot noise in ordinary metallic wires as it is almost completely canceled out due to the anti-correlation between the motion of individual electrons acting on each other through the coulomb force. This cancelation does not occur when we consider the random passage of charge carriers across a potential barrier such as the pn junction in a transistor [11]. The spectral density of the shot noise current is independent of frequency and given by:

$$S_i(f) = 2eI_{DC} \quad (2.4.12)$$

where  $e$  is the electron charge ( $1.60 \times 10^{-19}$ ) C and  $I_{DC}$  is the the average DC current. Figure 2.7 shows a simplified noise model for a silicon bipolar transistor [13]. The primary noise sources are the shot noise generated by the collector and base current and the thermal noise from the base spreading resistance.

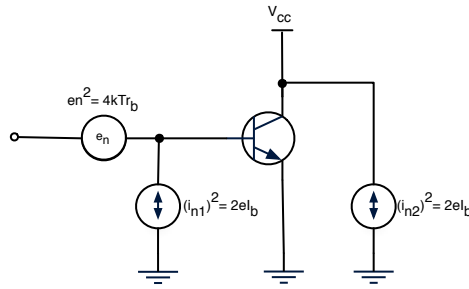


Figure 2.7: Simplified noise model of a Silicon Bipolar transistor.

### 2.4.3 Flicker Noise

It has been shown that when current passes through an electrical device there is noise present in excess of the thermal and shot noise components [11]. This additional noise is usually referred to as flicker noise. It has a spectral density characteristic of approximately  $\frac{1}{f}$  for low frequencies. At higher frequencies it has a flat spectrum and the noise power is weak, usually below the thermal noise. The point at which the spectrum moves from a  $\frac{1}{f}$  characteristic to a flat spectrum is termed the flicker noise corner. The mechanisms that give rise to this type of noise are not clearly understood. Flicker noise is present in any conducting material that is carrying a current. In resistors this noise is related to the number and quality of the contacts within the resistor [11]. In semiconductors the low frequency excess noise is generated as result of fluctuations in the number of charge carriers, resulting from the random movements in and out of the carrier traps associated with the crystal imperfections [14] [15].

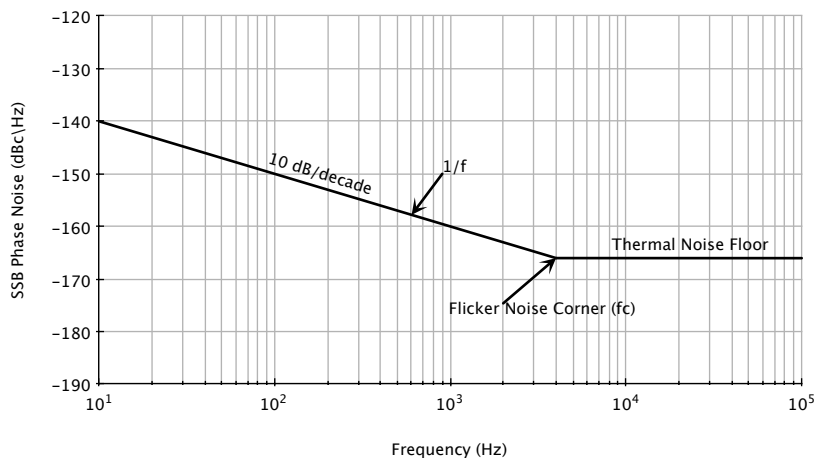


Figure 2.8: Typical residual phase noise plot for a silicon bipolar transistor amplifier with a 40 kHz flicker noise corner.

In amplifiers the flicker noise is typically up-converted onto the carrier and results in residual phase noise with a  $1/f$  characteristic as shown in figure 2.8. It has been suggested that for silicon bipolar amplifiers the  $1/f$  phase noise is largely caused by the base emitter recombination flicker noise [16]. The spectral density of an amplifier flicker noise can be modelled using equation (2.4.13).

$$S_a(f) = \frac{kTF}{P_{in}} \left( 1 + \frac{f_c}{\Delta f} \right) \quad (2.4.13)$$

where  $kTF$  is the thermal noise of an amplifier with noise figure  $F$  and input power,  $P_{in}$ .  $\Delta f$  is the carrier offset frequency and  $f_c$  is the flicker noise corner frequency.

#### 2.4.4 Oscillator Phase Noise Spectrum

Figure 2.9 shows a phase noise spectrum for a typical oscillator. There are four distinct regions in this plot. The  $\frac{1}{f^3}$  characteristic is a result of the up-conversion of the sustaining amplifier's flicker noise. The  $\frac{1}{f^2}$  characteristic is a result of the multiplication of the amplifiers white noise as described by the Lesson effect[7]. Finally, the  $\frac{1}{f}$  characteristic is a result of the sustaining amplifier phase noise or the flicker noise of an output buffer. At larger frequency offsets, outside the oscillator loop bandwidth, a noise floor is reached. This noise floor is a result of the thermal noise of the amplifier or it can represent the limitations of the measurement system.

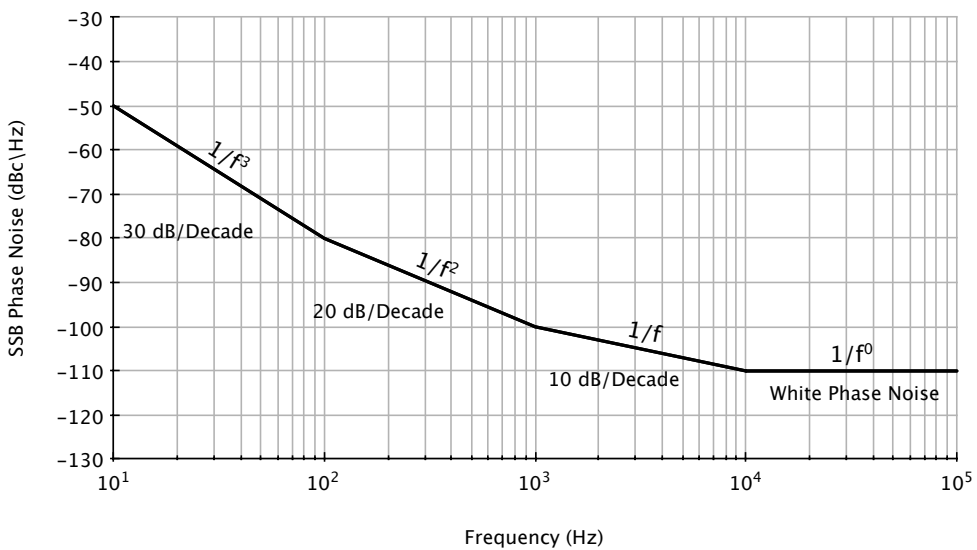


Figure 2.9: Typical oscillator phase noise spectrum.

## 2.5 Oscillator Phase Noise Model

In this section a linear theory describing the generation of phase noise in an oscillator is presented. The theory described will show which parameters explicitly affect the noise performance and a set of equations will be produced which accurately describe an oscillators noise performance. This theory has been developed by J.K.A Everard and is presented fully in [8].

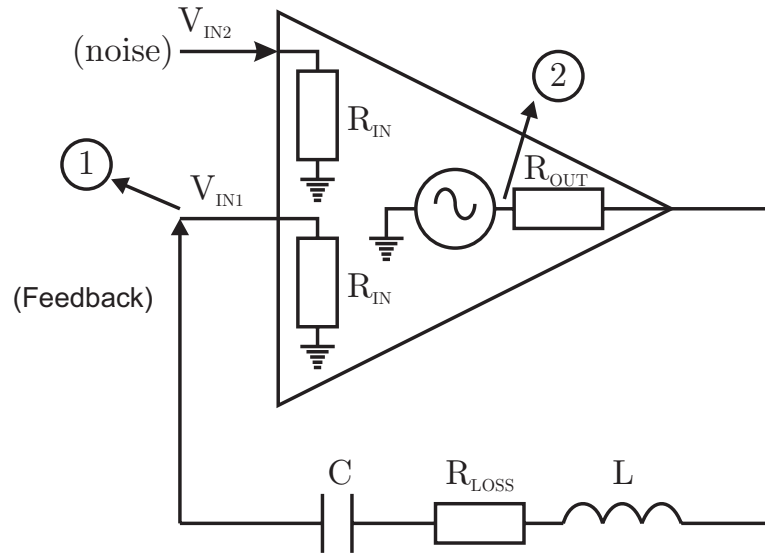


Figure 2.10: Equivalent circuit model for an oscillator.

Figure 2.10, illustrates an equivalent circuit which can be used to model a wide variety of oscillators. It consists of an amplifier and a resonator. The amplifier has two inputs with equal input impedance,  $R_{in}$ , and a single output with an impedance of  $R_{out}$ . The first input,  $V_{in2}$ , is used to model the noise and the second input,  $V_{in1}$ , as part of the feedback resonator. Two separate inputs allow the feedback path and noise input to be modelled separately, these inputs are summed and amplified to produce the output signal,  $V_{out}$ . It is assumed that any impedance transforms are incorporated into the feedback resonator model by modifying the LCR ratios. The circuit configuration above, is similar to that of a feedback operational amplifier. In order to analyse this circuit we will inject white noise into input  $V_{in2}$  and then calculate the voltage transfer function. The noise presented for amplification is dependent on the input impedance of the amplifier, the source resistance presented to the amplifier and the noise figure of the amplifier. It is assumed that the conditions defined in equations (2.1.5) and (2.1.5) are valid. The parameters required for this derivation are summarised in table 2.1.

Parameter	Description
$V_{in1}$	Input for feedback element
$V_{in2}$	Input for modelling resonator noise
$R_{in}$	Amplifier input impedance
$R_{out}$	Amplifier output impedance
$V_{out}$	Output dependant voltage source
$L$	Feedback Resonator Series Inductance
$C$	Feedback Resonator Series Capacitance
$R_{Loss}$	Feedback Resonator Loss Resistance
$G$	Amplifier Voltage Gain
$\beta$	Voltage Feedback Coefficient between nodes 1 and 2
$\beta_0$	Voltage Feedback Coefficient at resonance
$\omega_0$	Oscillator Centre Frequency
$\Delta\omega$	Offset Angular Frequency
$F$	Noise factor under Oscillating Conditions

Table 2.1: Oscillator Noise Modelling Parameters

The derivation of the phase noise equations can be spit into four stages and these are:

- Derive the voltage feedback coefficient,  $\beta$ .
- Using the feedback coefficient, derive the voltage transfer function.
- Derive the phase noise equation,  $L(f)$
- Optimise this equation and find it's minimum value.

Proceeding with step one, the voltage transfer function of our model can be written as:

$$V_{out} = G(V_{in2} + V_{in1}) \quad (2.5.1)$$

$$= G(V_{in2} + \beta V_{out}) \quad (2.5.2)$$

This can be manipulated into the form shown in equation (2.5.3)

$$\frac{V_{out}}{V_{in2}} = \frac{G}{1 - (\beta G)} \quad (2.5.3)$$

where  $\beta$  is the voltage transfer function of the resonator between nodes one and two and can be calculated as:

$$\beta = \frac{R_{in}}{R_{in} + R_{out} + R_{loss} + j\left(\omega L - \frac{1}{\omega C}\right)} \quad (2.5.4)$$

If we assume that  $\Delta\omega = \omega \pm \omega_0$  and  $\Delta\omega \ll \omega_0$ , where  $\Delta\omega$  is the angular frequency offset from the carrier then:

$$\omega L - \frac{1}{\omega C} = \pm 2\Delta\omega L \quad (2.5.5)$$

The closed loop loaded quality factor,  $Q_L$ , of the series LCR resonator, is:

$$Q_L = \frac{\omega_0 L}{R_{total}} \quad (2.5.6)$$

This can be expanded to give:

$$Q_L = \frac{\omega_0 L}{R_{in} + R_{out} + R_{loss}} \quad (2.5.7)$$

If we substitute equations (2.5.4), (2.5.5) into (2.5.7) and rearrange then the feedback coefficient  $\beta$  can be written as:

$$\beta = \frac{R_{in}}{(R_{in} + R_{out} + R_{loss}) \left(1 \pm 2jQ_L \frac{\Delta\omega}{\omega_0}\right)} \quad (2.5.8)$$

The unloaded quality factor,  $Q_0$  of the resonator can be written as:

$$Q_0 = \frac{\omega_0 L}{R_{loss}} \quad (2.5.9)$$

Using Equations (2.5.7) and (2.5.9) we can write the ratio of loaded to unloaded Q as:

$$\frac{Q_L}{Q_0} = \frac{R_{loss}}{R_{in} + R_{out} + R_{loss}} \quad (2.5.10)$$

Equation (2.5.10) can be rearranged to give:

$$\left(1 - \frac{Q_L}{Q_0}\right) = \frac{R_{in} + R_{out}}{R_{in} + R_{out} + R_{loss}} \quad (2.5.11)$$

At resonance the imaginary terms in (2.5.4) and (2.5.8) are zero. We can therefore write the feedback coefficient at resonance,  $\beta_0$ , between nodes 1 and 2 as:

$$\beta_0 = \frac{R_{in}}{R_{in} + R_{out} + R_{loss}} \quad (2.5.12)$$

$$= \left(1 - \frac{Q_L}{Q_0}\right) \left(\frac{R_{in}}{R_{in} + R_{out}}\right) \quad (2.5.13)$$

The resonator response is therefore:

$$\beta = \left( \frac{R_{in}}{R_{in} + R_{out}} \right) \left( 1 - \frac{Q_L}{Q_0} \right) \left( \frac{1}{1 \pm 2jQ_L \frac{\Delta f}{f_0}} \right) \quad (2.5.14)$$

Where  $f_0$  is the centre frequency and  $\Delta f$  is the offset frequency from the carrier.

We can now complete stage two of the derivation and define the voltage transfer function with the inclusion of the voltage feedback coefficient,  $\beta$ . Substituting (2.5.14) into (2.5.3) gives:

$$\frac{V_{out}}{V_{in2}} = \frac{G}{1 - \left( \frac{G \left( 1 - \frac{Q_L}{Q_0} \right) \left( \frac{R_{in}}{R_{out} + R_{in}} \right)}{1 \pm 2jQ_L \frac{\Delta f}{f_0}} \right)} \quad (2.5.15)$$

At resonance  $\Delta f$  is zero and  $\frac{V_{out}}{V_{in2}}$  is very large. In effect, the denominator of Equation (2.5.15) is virtually zero. We can therefore state that the operating condition specified in (2.1.5) applies. Recalling equation (2.1.5), rearranging and substituting for  $\beta_0$ , we obtain:

$$G = \frac{1}{\left( 1 - \frac{Q_L}{Q_0} \right) \left( \frac{R_{in}}{R_{in} + R_{out}} \right)} \quad (2.5.16)$$

Inserting this expression into (2.5.15) we obtain:

$$\frac{V_{out}}{V_{in2}} = \frac{G}{1 - \frac{1}{1 \pm 2jQ_L \frac{\Delta f}{f_0}}} \quad (2.5.17)$$

$$= \frac{1}{\left( 1 - \frac{Q_L}{Q_0} \right) \left( \frac{R_{in}}{R_{in} + R_{out}} \right) \left( 1 - \frac{1}{1 \pm (2jQ_L \frac{\Delta f}{f_0})} \right)} \quad (2.5.18)$$

If we are only interested in close to carrier noise then  $\frac{Q_L \Delta f}{f_0} \ll 1$  and Equation (2.5.18) simplifies to:

$$\frac{V_{out}}{V_{in2}} = \frac{G}{\pm 2jQ_L \frac{\Delta f}{f_0}} \quad (2.5.19)$$

$$= \frac{1}{\left( 1 - \frac{Q_L}{Q_0} \right) \left( \frac{R_{in}}{R_{in} + R_{out}} \right) \left( \pm 2jQ_L \frac{\Delta f}{f_0} \right)} \quad (2.5.20)$$

Oscillator phase noise is typically quoted in terms of the ratio  $\mathcal{L}(f)$  which

is defined as the ratio of the noise power in a 1 Hz bandwidth at an offset of  $\Delta f$  from the carrier, to the total power in the carrier. We can calculate the phase noise by converting the voltage transfer characteristic to a form which is proportional to power. Only the power dissipated in the oscillating system and not the power dissipated in the load is included.

The square of the input noise power in a 1Hz bandwidth is given by equation (2.5.21). It can be shown that the sideband noise power of the oscillator reaches the background level of noise by the 3 dB point of the resonator. Therefore, the noise of interest lies inside the bandwidth of the resonator, this is why the tuned circuit can be represented as a resistor for the close to carrier performance.

$$V_{in2}^2 = FkTR_{in} \quad (2.5.21)$$

It should be noted that noise figure  $F$ , is the operating noise figure under oscillating conditions and  $kT$  is the noise power that would be available to the input if the source and input impedance were equal.

Using Equation (2.5.21) and (2.5.20) an expression for  $V_{out}^2(\Delta f)$  can be obtained:

$$V_{out}^2(\Delta f) = \frac{FkTR_{in}}{4Q_L^2 \left(\frac{R_{in}}{R_{in}+R_{out}}\right)^2 \left(1 - \frac{Q_L}{Q_0}\right)^2} \left(\frac{f_0}{\Delta f}\right)^2 \quad (2.5.22)$$

This equation can be rewritten in terms of  $\frac{Q_L}{Q_0}$  to give:

$$V_{out}^2(\Delta f) = \frac{FkTR_{in}}{4Q_0^2 \left(\frac{Q_L}{Q_0}\right)^2 \left(\frac{R_{in}}{R_{in}+R_{out}}\right)^2 \left(1 - \frac{Q_L}{Q_0}\right)^2} \left(\frac{f_0}{\Delta f}\right)^2 \quad (2.5.23)$$

We can incorporate the non-linearity's introduced by the amplifier limiting into equation (2.5.23) by modifying the absolute value of the noise. If the amplifier is operating hard into saturation then any amplitude noise will be suppressed and the phase noise halved. Equation (2.5.23) therefore becomes:

$$V_{out}^2(\Delta f) = \frac{FkTR_{in}}{8Q_0^2 \left(\frac{Q_L}{Q_0}\right)^2 \left(\frac{R_{in}}{R_{in}+R_{out}}\right)^2 \left(1 - \frac{Q_L}{Q_0}\right)^2} \left(\frac{f_0}{\Delta f}\right)^2 \quad (2.5.24)$$

The phase noise,  $\mathcal{L}(f)$ , of the oscillator is defined as:

$$\mathcal{L}(f) = \frac{V_{out}^2(\Delta f)}{V_{OutMaxRMS}^2} \quad (2.5.25)$$

Substituting (2.5.24) into (2.5.25) gives:

$$\mathcal{L}(f) = \frac{FkTR_{in}}{8Q_0^2 \left(\frac{Q_L}{Q_0}\right)^2 \left(\frac{R_{in}}{R_{in}+R_{out}}\right)^2 \left(1 - \frac{Q_L}{Q_0}\right)^2 V_{OutMaxRMS}^2} \left(\frac{f_0}{\Delta f}\right)^2 \quad (2.5.26)$$

If we define  $P_{AVO}$  as the power available at the output of the amplifier into a matched load then we can write:

$$P_{AVO} = \frac{V_{OutMaxRMS}^2}{4R_{out}} \quad (2.5.27)$$

Incorporating this into Equation (2.5.26) gives:

$$\mathcal{L}(f) = \frac{FkTR_{in}}{8Q_0^2 \left(\frac{Q_L}{Q_0}\right)^2 \left(\frac{R_{in}}{R_{in}+R_{out}}\right)^2 \left(1 - \frac{Q_L}{Q_0}\right)^2 P_{AVO} 4R_{out}} \left(\frac{f_0}{\Delta f}\right)^2 \quad (2.5.28)$$

Which can be rearranged to give:

$$\mathcal{L}(f) = \frac{FkT}{32Q_0^2 \left(\frac{Q_L}{Q_0}\right)^2 \left(1 - \frac{Q_L}{Q_0}\right)^2 P_{AVO}} \left(\frac{(R_{in} + R_{out})^2}{R_{in}R_{out}}\right) \left(\frac{f_0}{\Delta f}\right)^2 \quad (2.5.29)$$

The second term in Equation (2.5.29) can be shown to be minimum when  $R_{out} = R_{in}$  it's value at this point is 4. It should be noted that this statement is only true when the power is defined as the power available at the output of the amplifier. Equation (2.5.29) now becomes:

$$\mathcal{L}(f) = \frac{FkT}{8Q_0^2 \left(\frac{Q_L}{Q_0}\right)^2 \left(1 - \frac{Q_L}{Q_0}\right)^2 P_{AVO}} \left(\frac{f_0}{\Delta f}\right)^2 \quad (2.5.30)$$

This can be modified to include the residual phase noise of the amplifier under operating conditions buy multiplying by  $1 + \frac{f_c}{\Delta f}$  to give:

$$\mathcal{L}(f) = \frac{FkT}{8Q_0^2 \left(\frac{Q_L}{Q_0}\right)^2 \left(1 - \frac{Q_L}{Q_0}\right)^2 P_{AVO}} \left(\frac{f_0}{\Delta f}\right)^2 \left(1 + \frac{f_c}{\Delta f}\right) \quad (2.5.31)$$

Equation (2.5.30) describes the noise performance within the 3 dB bandwidth of the resonator. It is apparent that, for minimum phase noise, the resonator unloaded quality factor,  $Q_0$ , should be made as large as possible while the amplifier noise factor,  $F$ , should be minimised.

This equation can now be optimised for minimum noise: The minimum value of Equation (2.5.30) can be calculated by differentiating with respect to  $\frac{Q_L}{Q_0}$  and equating the result to zero:

$$\frac{d\mathcal{L}(f)}{d\left(\frac{Q_L}{Q_0}\right)} = 0 \quad (2.5.32)$$

It can be shown [8] that the minimum phase noise occurs when  $\frac{Q_L}{Q_0} = 0.5$ . Substituting this value into equation (2.5.30) gives:

$$L_{fm} = \frac{2FkT}{Q_0^2 P_{AVO}} \left(\frac{F_0}{\Delta f}\right)^2 \quad (2.5.33)$$

This equation describes the sideband phase noise when the oscillator is operating under optimum conditions (minimum phase noise). Equation 2.5.33 shows that the oscillator phase noise is proportional to the noise factor of the sustaining amplifier and inversely proportional to the amplifier output power and the square of the resonator unloaded quality factor,  $Q_0$ . Therefore, in order to minimise the oscillator sideband phase noise we should maximise the amplifier output power and the resonator quality factor while minimising the amplifier noise figure. Doubling the resonator unloaded quality factor will result in a 6 dB reduction in side-band phase while halving the amplifier noise factor will result in a 3 dB reduction.

# Chapter 3

## High Q Distributed Bragg Resonator

### 3.1 Microwave Resonators

The purpose of this chapter is to describe the design, simulation and measurement results for a high Q X-Band cylindrical distributed Bragg resonator which utilises an aperiodic arrangement of non  $\lambda/4$  low loss alumina plates.

High-quality factor microwave resonators are an important component in many communications, RADAR systems and in their associated test equipment. They are essential elements in, for example, low phase-noise oscillators, low-insertion-loss narrow band filters and frequency discriminators. There are several types of resonator structure that are typically used at microwave frequencies: these include the empty metal cavity resonator, the dielectric resonator and the whispering gallery mode (WGM) resonator. The unloaded quality factor ( $Q_0$ ) of an empty metal cavity resonator is limited by the conduction losses in the side and end walls of the shield. The maximum unloaded quality factor attainable from a dielectric resonator is defined by the loss tangent ( $\tan \delta$ ) of the dielectric material in addition to the losses introduced by the shield used to enclose the resonator. The effect of the wall losses on the Q-factor of a dielectric resonator is highly dependent on the distance between the resonator and the walls as well as the resonant mode used. Dielectric resonators are typically operated using the  $TE_{01\delta}$  mode and providing the walls are sufficiently far from the resonator, the effect of the wall losses on the Q-factor is minimal. Modern dielectric resonators are capable of providing Q-factors of between 10,000 and 30,000 at 10 GHz [17][18]. The performance of the dielec-

tric loaded cavity can be further improved by using a whispering gallery mode (WGM) resonator. This type of structure confines the field energy to the outer edge of a ring of dielectric material and the quality factor is almost entirely defined by the loss tangent of the dielectric material. At microwave frequencies room temperature quality factors in the region of 200,000 are achievable using sapphire [19] and 100,000 using mono-crystalline rutile [20].

### 3.1.1 The Distributed Bragg Structure

The distributed Bragg resonator can offer a substantial increase in quality factor when compared with traditional microwave resonators. It is a structure formed by replacing the end and/or sidewalls of an empty metal cavity with alternating layers of air and dielectric material. The sudden change in dielectric constant at each air-dielectric interface causes a partial reflection of the incident electromagnetic wave. If several air-dielectric layers are combined, then more of the energy is reflected back into the central air region of the cavity and kept away from the lossy metal end walls. Figure 3.1 illustrates the structure of a typical cylindrical Bragg reflector resonator.

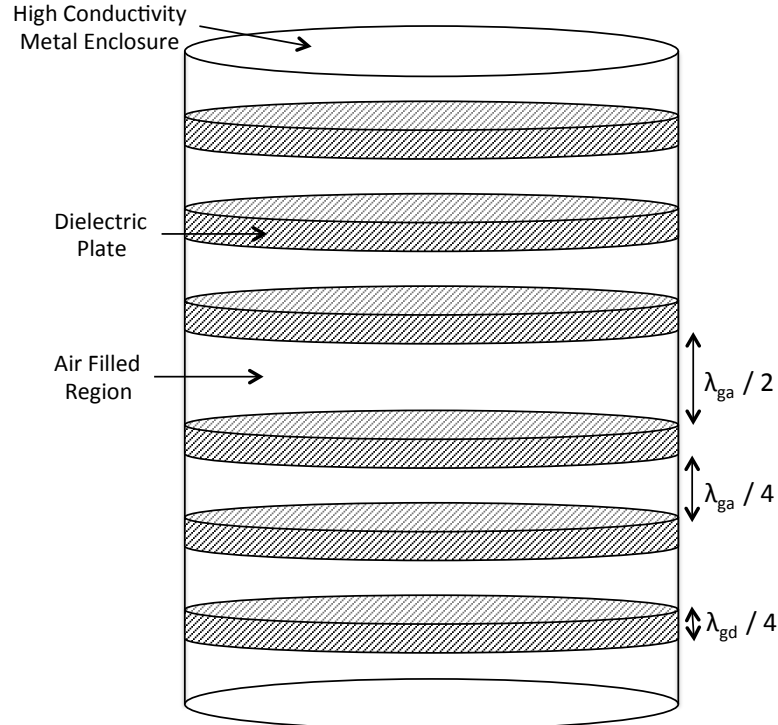


Figure 3.1: The structure of a periodic Bragg reflector resonator. The dielectric plates and air sections are one quarter of the guide wavelength in thickness, where  $\lambda_{ga}$  and  $\lambda_{gd}$  are the guide wavelength in air and dielectric respectively.

Two distinct classes of distributed Bragg resonator can be identified in the literature and these are the periodic reflector and the aperiodic reflector. In a periodic reflector, each of the dielectric plates and air sections are one quarter of the guide wavelength  $\lambda_g/4$  in thickness to maximise their reflectivity [21]. Flory and Taber [21] and Flory and Ko [22] demonstrate experimental results for 9.0 GHz and 13.2 GHz sapphire resonators consisting of interpenetrating concentric rings and plates with quality factors of 65,000 and 45,000, respectively. Maggiore et al. [23] demonstrated a distributed Bragg sapphire resonator with stated Qs of  $5.31 \times 10^5$  at 18.99GHz. Krupka et al. [24] demonstrated a Fabry-Perot resonator operating at 39 GHz consisting of 2 pairs of quarter-wavelength single crystal quartz Bragg reflectors. It achieved a Q-factor of 560000. Tobar et al. [25] demonstrated a Teflon spherical Bragg resonator with a stated Q of 22,000 at 13.86 GHz. Later Krupka et al. [26] demonstrated spherical Bragg resonators that were constructed from single-crystal YAG and quartz. The quartz resonator produced a Q-factor of  $1.04 \times 10^5$  at 26.26 GHz and the YAG resonator produced a Q of  $6.4 \times 10^4$  at 27.63 GHz.

In a recent paper, Breeze et al. [27] state that the majority of the losses in a periodic Bragg reflector occur in the first quarter wave layer and that, by redistributing the energy into the lower loss air regions, an increase in quality factor can be achieved. They demonstrate, through simulation, that by utilising an aperiodic arrangement of dielectric plates with thicknesses which asymptotically approach quarter wave reflectors as the cavity end walls are reached, a spherical Bragg resonator can be designed with a quality factor in excess  $10^7$  at 10 GHz. Floch, Tobar, Cros and Krupka [28] also demonstrate the development of a simple non-Maxwellian model that allows the design of Bragg resonators with dielectric reflectors of an arbitrary thickness.

## 3.2 ABCD Parameter Model

In this section a simple ABCD parameter waveguide model is developed which can be used to characterise the performance of a Bragg resonator. This model represents a cylindrical structure, although the equations could easily be modified to represent a rectangular resonator. A cylindrical structure was chosen because it offers a simple mechanical construction.

In this model each air and dielectric section of the Bragg structure is considered to be a separate waveguide which we represent using a two-port network. These two port networks are then cascaded to form the complete Bragg res-

onator. The ABCD parameter set is used to describe these two port networks because the series cascade connection of these networks reduces to a simple matrix multiplication. Figure 3.2 show a simple two port network. The directions of the port voltages and currents are shown and it should be noted that convention that  $I_2$  flows out of port 2 is used. This is so that when several networks are connected in cascade the current  $I_2$  will be the same current that flows into port one of the adjacent network.

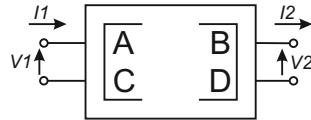


Figure 3.2: A 2-Port network represented using ABCD parameters.

This two port ABCD network can be defined mathematically using the following equations:

$$\begin{bmatrix} V_1 \\ I_1 \end{bmatrix} = \begin{bmatrix} A & B \\ C & D \end{bmatrix} \begin{bmatrix} V_2 \\ I_2 \end{bmatrix} \quad (3.2.1)$$

$$V_1 = AV_2 + BI_2 \quad (3.2.2)$$

$$I_1 = CV_2 + DI_2 \quad (3.2.3)$$

Figure 3.3 illustrates the cascade connection of a pair of two port networks represented using ABCD parameters and the corresponding matrix equation is shown in (3.2.4) (3.2.4):

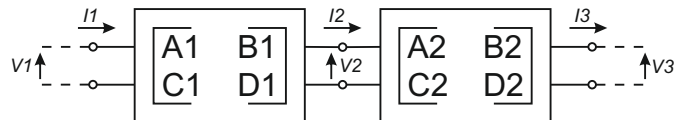


Figure 3.3: A cascade connection of two 2-Port network represented using ABCD parameters.

$$\begin{bmatrix} V_1 \\ I_1 \end{bmatrix} = \begin{bmatrix} A_1 & B_1 \\ C_1 & D_1 \end{bmatrix} \begin{bmatrix} A_2 & B_2 \\ C_2 & D_2 \end{bmatrix} \begin{bmatrix} V_3 \\ I_3 \end{bmatrix} \quad (3.2.4)$$

The ABCD matrix must now be defined for each section of the resonator. The ABCD matrix for a lossy transmission line of length  $l$  meters with complex propagation constant  $\gamma$  and characteristic impedance  $Z_0$  is shown in equation (3.2.5).

$$\begin{bmatrix} V_1 \\ I_1 \end{bmatrix} = \begin{bmatrix} \cosh(\gamma l) & Z_0 \sinh(\gamma l) \\ \frac{1}{Z_0} \sinh(\gamma l) & \cosh(\gamma l) \end{bmatrix} \begin{bmatrix} V_2 \\ I_2 \end{bmatrix} \quad (3.2.5)$$

In order to correctly represent each section of the resonator using this equation it is necessary to calculate the complex propagation constant and wave impedance for each reflector section. These calculations are performed assuming the wave is traveling in a cylindrical wave guide. The complex propagation constant,  $\gamma$ , is defined by (3.2.6):

$$\gamma = \alpha + j\beta \quad (3.2.6)$$

where  $\alpha$  is the attenuation coefficient measured in units of  $Npm^{-1}$  and  $\beta$  is the phase constant.

As we are considering a cylindrical structure the phase constant for the dielectric and air sections can be calculated using equation (3.2.7):

$$\beta = \sqrt{\omega^2 \mu \epsilon - \left(\frac{\chi'_{mn}}{a}\right)^2} \quad (3.2.7)$$

where  $\epsilon$  is the permittivity of the dielectric or air,  $\omega$  is the angular frequency and  $a$  is the cavity radius.  $\chi'_{mn}$  represents the  $n$ th zero of the derivative of the Bessel function of this first kind of order  $m$ . In the case of the  $TE_{01}$  mode the value of  $\chi'_{mn} \approx 3.8318$ .

### 3.2.1 Air Section Attenuation

The only loss in the air filled sections of the resonator is a result of the conductive side walls. This can be calculated using the perturbation method [29] and the resulting equation is show in (3.2.8). This equation represents the attenuation coefficient, in units of  $Npm^{-1}$ , for a transverse electric (TE) mode with circumferential mode number  $m$  and radial mode number  $n$  in a cylindrical waveguide of radius  $a$  operating at frequency,  $f$ .

$$(\alpha_{mn}^{TEz}) = \frac{R_S}{a\eta\sqrt{1 - \left(\frac{f_c}{f}\right)^2}} \left[ \left(\frac{f_c}{f}\right)^2 + \frac{m^2}{(\chi'_{mn})^2 - m^2} \right] \quad (3.2.8)$$

where  $\eta$ , given by (3.2.9), represents the wave impedance for a plane wave inside an unbounded infinite medium with permittivity,  $\epsilon$  and permeability  $\mu$

$$\eta = \sqrt{\frac{\mu}{\epsilon}} \quad (3.2.9)$$

The surface loss resistance of the guide walls is represented by  $R_s$  and this is a function of the wall conductivity,  $\sigma$ . The value of  $R_s$  is calculated using (3.2.10).

$$\eta = \sqrt{\frac{\omega\mu}{2\sigma}} \quad (3.2.10)$$

The lower cut off frequency of the guide is given by  $f_c$  and its value can be calculated using (3.2.11)

$$f_c = \frac{\chi'_{mn}}{2\pi a\sqrt{\mu\epsilon}} \quad (3.2.11)$$

The only remaining term required to describe ABCD matrix for the air filled sections is the guide wave impedance  $Z_0$ . This can be calculated for a transverse electric mode using (3.2.12).

$$Z_{TE} = \frac{\eta}{\sqrt{1 - \left(\frac{f_c}{f}\right)^2}} \quad (3.2.12)$$

### 3.2.2 Dielectric Sections

The total loss in the dielectric sections,  $\alpha_t$ , can be considered as the sum of the sidewall conducting loss,  $\alpha_c$ , and the dielectric losses,  $\alpha_d$ .

$$\alpha_t = \alpha_c + \alpha_d \quad (3.2.13)$$

The conductive side wall losses can be calculated using 3.2.8 but the loss in the dielectric must be treated differently. The attenuation due to the lossy dielectric,  $\alpha_d$ , can be calculated from the complex propagation constant [30]. If the loss is small then the phase constant in the dielectric section can be assumed constant. The attenuation due to dielectric loss is given by equation (3.2.14):

$$\alpha_d = \frac{\omega^2\mu\epsilon \tan \delta}{2\sqrt{\omega^2\mu\epsilon - \left(\frac{\chi'_{mn}}{a}\right)^2}} \quad (3.2.14)$$

where  $\tan \delta$  is the loss tangent of the dielectric and  $\epsilon$  is the relative permittivity of the dielectric.

### 3.2.3 Metal End Walls

The loss in the metal end walls of the cavity can be approximated by considering the complex propagation constant,  $\gamma$ , and intrinsic wave impedance,  $\eta$ , for

a plane wave in a good conductor. As is described in [30], the complex propagation constant inside a good conductor can be approximated using equation (3.2.15):

$$\gamma = j\omega\sqrt{\mu\epsilon}\sqrt{\frac{\sigma}{j\omega\epsilon}} \quad (3.2.15)$$

This can be manipulated into the form show in equation (3.2.16):

$$\gamma = (1 + j)\sqrt{\frac{\omega\mu\sigma}{2}} \quad (3.2.16)$$

The intrinsic wave impedance,  $\eta$ , for a plane wave in a general lossy medium is given by:

$$\eta = \frac{j\omega\mu}{\gamma} \quad (3.2.17)$$

If we substitute (3.2.16) into (3.2.17) then, after several manipulations, we can write:

$$\eta = Z_S = (1 + j)\sqrt{\frac{\omega\mu}{2\sigma}} \quad (3.2.18)$$

Equation (3.2.18) describes the wave impedance inside a good conductor. It can be seen that the real and imaginary parts of this equation can be modelled as an impedance consisting of a series connected resistance and inductance. In terms of ABCD parameters this can be written as:

$$\begin{bmatrix} V_1 \\ I_1 \end{bmatrix} = \begin{bmatrix} 1 & 0 \\ \frac{1}{Z_S} & 1 \end{bmatrix} \begin{bmatrix} V_2 \\ I_2 \end{bmatrix} \quad (3.2.19)$$

Using equations (3.2.5) to (3.2.18) it is now possible to characterise a dielectric, air and metal end wall section of the Bragg resonator in terms of its ABCD parameters. This model offers several advantages when compared to a full field simulation. It is possible to model a Bragg resonator with any number of dielectric and air sections of arbitrary lengths. The computation requirements are minimal and the resonant frequency and quality factor for a given mode can be extracted very rapidly using standard circuit simulation techniques. One disadvantage of the model is that it considers each mode in isolation, and therefore, to calculate the resonant frequencies of other modes, additional simulations are required.

### 3.2.4 Periodic Resonator Simulation

Using the ABCD waveguide model it is now possible to evaluate the performance of a cylindrical Bragg resonator. The cavity will be designed to operate using the  $TE_{011}$  mode at 10 GHz. This is the mode typically chosen for high Q cavities as it exhibits a low inherent loss [30]. It is possible to obtain an increase in Q by designing the cavity to operate using a higher order mode, such as  $TE_{012}$ , but this has the disadvantage of increasing the cavity volume. A block diagram of the model for a two plate resonator is shown in figure 3.4:

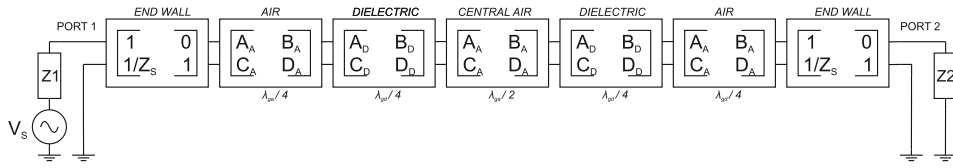


Figure 3.4: A waveguide ABCD parameter model for a two plate periodic Bragg resonator.

Each block represents a single  $ABCD$  matrix where the  $(A, B, C, D)_A$  terms represent the air section parameters, the  $(A, B, C, D)_D$  terms represent the dielectric section parameters and the  $(A, B, C, D)_C$  terms represent the central air section parameters. The cavity radius was assumed to be 60 mm, and the lengths of the air and dielectric reflector sections were set to one-quarter of the guide wavelength ( $\lambda_g/4$ ) for a  $TE_{01}$  mode at 10 GHz. The value of the guide wavelength was calculated using equation (3.2.20):

$$\lambda_g = \frac{2\pi}{\beta} \quad (3.2.20)$$

where  $\beta$  is the phase constant for the  $TE_{mn}$  mode of interest, which can be calculated using (3.2.7). Energy is driven into the structure through the port source impedances,  $Z1$ , by the source  $V_s$ . In order to simplify the calculation of the forward transmission scattering parameter the port impedances were set equal ( $Z1 = Z2$ ) and  $S_{21}$  was calculated using equation (3.2.21), a more detailed explanation of this method is described in [8].

$$S_{21} = \frac{2V_o}{V_s} \quad (3.2.21)$$

A summary of the parameters used to define the periodic Bragg resonator model are shown in table 3.1.

Parameter	Symbol	Value
Operating frequency	$(f_r)_{011}^{TE^Z}$	10 GHz
Cavity radius	$a$	60 mm
Air section length	$l_a$	7.87 mm
Dielectric section length	$l_d$	2.41 mm
Central air section length	$d$	15.73 mm
Dielectric permittivity	$\epsilon_d$	9.75
Dielectric loss tangent	$\tan \delta$	$1 \times 10^{-5}$
Wall conductivity	$\sigma$	$6.173 \times 10^7 \text{ Sm}^{-1}$
Air - Attenuation coefficient	$\alpha_a$	$0.0001090 \text{ Npm}^{-1}$
Air - Phase constant	$\beta_a$	$199.683 \text{ radm}^{-1}$
Dielectric - Attenuation coefficient	$\alpha_d$	$0.003321 \text{ Npm}^{-1}$
Dielectric - Phase constant	$\beta_d$	$651.304 \text{ radm}^{-1}$
End wall impedance	$Z_S$	$0.0252\Omega + 0.4025pH$
Port source impedance	$Z_{1,2}$	$50 \Omega$

Table 3.1: Model parameters for a cylindrical periodic Bragg resonator. The resonator has silver plated walls and operates with the  $TE_{011}$  mode at 10 GHz

In order to maximise the quality factor of the resonator it is essential that side wall and dielectric losses are minimised. The side wall loss can be reduced by using a high conductivity metal such as Silver or Aluminium. The dielectric losses are directly proportional to the loss tangent of the material used. There are many low loss dielectrics available on the market but their manufacturing process and structural properties limit the maximum diameter that can reliably manufactured while maintaining flatness and loss tangent. A brief survey of manufacturers located the CoorsTek PlasmaPure-UC SA999 low sodium, high purity Alumina. This material has a purity of 99.9%, a loss tangent of  $1 \times 10^{-5}$  at 5 GHz and a relative permittivity of 9.75. After consultation with the manufacturer a maximum diameter of 120 mm was selected. This allowed them to maintain a tolerance of 0.0508 mm for the thickness of the dielectric with a surface roughness of 0.8  $\mu\text{m}$ .

In a periodic Bragg resonator the Q-factor will begin to saturate as the number of dielectric plates is increased. This saturation is a result of the exponential decay of the electric field as the cavity end walls are approached [21]. In order to ascertain the maximum quality factor obtainable from a periodic Bragg resonator utilising our dielectric several S-parameter simulations were performed using the model shown in 3.4. Increasing numbers of dielectric plates were added and the quality factor calculated.

Number of Dielectric Plates	Unloaded Quality Factor ( $Q_0$ )
1	27,548
2	125,785
4	289,854
6	322,579
8	327,867
10	327,867

Table 3.2: The simulated unloaded quality factor ( $Q_0$ ) for periodic Bragg resonators with varying numbers of dielectric plates.

It can be seen from the results in table 3.2 that the unloaded quality factor begins to saturate when more than six plates are used. The quality factor of the periodic Bragg design could be further improved by increasing the cavity radius in order to reduce the wall loss. However, this has the undesirable affect of increasing the number of spurious modes.

### 3.3 Resonator Optimisation

Breeze, Krupka and Alford [27] have demonstrated that a significant improvement in the quality factor of a Bragg resonator can be achieved by utilising an aperiodic plate arrangement to re-distribute the energy inside the cavity into the lower loss air sections. We can consider the Bragg resonator as a structure consisting of two identical distributed reflectors designed to confine energy into a central air region. We can therefore optimise the quality factor of this type of structure by attempting to maximise the magnitude of the input reflection coefficient ( $\Gamma_{in}$ ) of both reflectors as illustrated in figure 3.5.

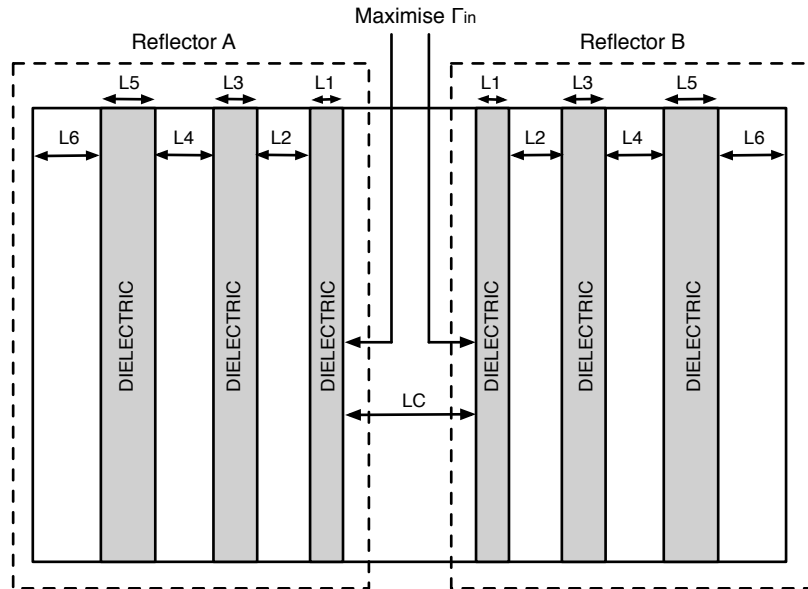


Figure 3.5: An aperiodic Bragg resonator consisting of two identical distributed Bragg reflectors. The widths of the dielectric and air sections can be optimised in order to maximise the magnitude of the input reflection coefficient ( $\Gamma_{in}$ )

In order to ascertain the reflector thicknesses required for maximum quality factor in our resonator a numerical optimisation procedure was adopted. For a six plate Bragg resonator there are three dielectric sections and three air sections in each reflector we therefore have a total of six variables in our optimisation problem and must select an algorithm suitable for this type of problem.

### 3.3.1 Genetic Algorithm

Genetic Algorithms are type of stochastic and adaptive search algorithm based on ideas taken from natural selection and genetics. Instead of starting from a single solution a genetic algorithm creates a random population of initial solutions spread throughout the search space. The algorithm then uses there operators selection, crossover and mutation to evolve the fitness of the individuals within the population until the global optimum is reached. These operators are analogous to the process of evolution that occurs in the natural world. Genetic algorithms were established by John Holland [31] in 1975 although there are earlier examples of evolutionary programming techniques such as those described by Fogel [32]. Genetic algorithms are well suited to solving problems with a high dimensionality search space [33] and therefore represent a good choice for the resonator optimisation problem. It is necessary to specify four different functions in order to fully define a genetic algorithm and these include:

- The genotype - This is the data structure that contains the parameters required to fully specify a candidate solution. It is this structure that is subject to the actual optimisation. Genetic algorithms traditionally use arrays of binary strings to represent an individual genotype.
- Genetic operators - These operators are named crossover and mutation. Crossover defines how the genes from parent individuals are combined in order to produce offspring. A mutation operator describes the method that is used to introduce random perturbations into the genome.
- Fitness function - The fitness function evaluates the performance of each individual and assigns it a value. The fitness function therefore contains a description of the problem to be solved as well as a definition of the test environment.
- Selection scheme - The selection scheme chooses which individuals should be allowed to produce offspring for the next generation as well as the individuals that will survive between generations.

The implementation of these functions is discussed in the following three sub-sections.

### 3.3.1.1 Genotype Encoding

The first stage in designing a genetic algorithm to optimise the Bragg resonator structure is to choose a genetic representation that will encode the lengths of dielectric and air sections. In this work binary strings of 1s and 0s are used to encode the length of each resonator section. These sub-string are then concatenated to form a longer string (chromosome) that fully defines the dimensions of the resonator. Figure 3.6 illustrates this data structure:

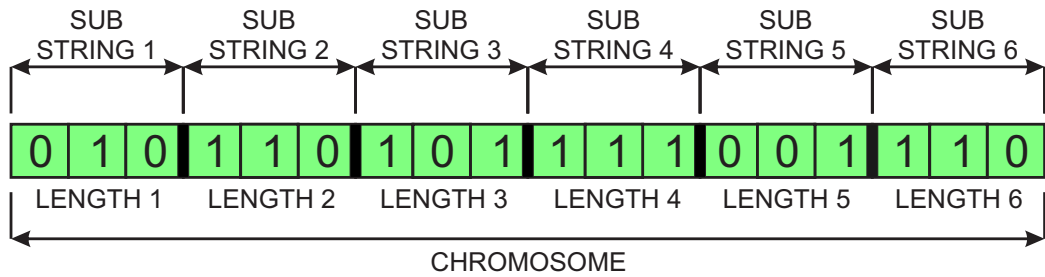


Figure 3.6: Bragg resonator genotype encoding, three bit sub-strings are shown in this figure. The actual optimisation algorithm used 26 bit sub-strings for increased accuracy.

Each binary sub-string represents the length of a single resonator section. A linear mapping exists between the fixed length binary strings and the real value which represents the resonator section length. The integer represented by the binary string can be mapped to a real number using equation (3.3.1):

$$r = \frac{r_{max} - r_{min}}{2^l - 1} z + r_{min} \quad (3.3.1)$$

where  $r_{min}$  and  $r_{max}$  represent the minimum and maximum possible values in the real number space,  $l$  is the binary string length and  $z$  is the integer represented by the binary string. If we assume that  $r_{min} = 0$  and  $r_{max} = 100mm$  then for a 26 bit binary string length we can achieve a precision of approximately 1.5 nm. This is much greater the manufacturing tolerance of any of the resonator components.

### 3.3.1.2 Selection Operator

There are many selection approaches that can be used in genetic algorithms. A simple approach would be to choose the best 50% for reproduction and inclusion in the next generation. The problem with this approach is that that it makes no distinction between an excellent individual or one who's fitness is merely satisfactory. In this algorithm we use fitness-proportional selection,

in this approach the probability of selection is proportional the fitness of an individual. The technique is summarised below:

- Calculate the sum of the fitness of all population members and store in a variable  $f_{sum}$ .
- Select a random number,  $R_s$ , between 0 and  $f_{sum}$ .
- Iterate over the whole population and calculate a running sum of the fitness. When this fitness sum is greater than  $R_s$  stop; the last individual added is the selected individual.

The selection operator is applied twice to select a pair of individuals that are the passed to the crossover operator. Selection is continued until the whole population has been processed. Unfortunately, due to the probabilistic nature of fitness proportional selection the fittest individual can be frequently thrown away. A small modification is therefore made to the previous algorithm which ensures that the fittest individual is always propagated into the next generation without undergoing crossover or mutation.

### 3.3.1.3 Crossover and Mutation

Crossover or as it is also know, recombination describes the way by which offspring genotypes are assembled from two or more parents. In this algorithm we use single point crossover where the binary strings are cut at a random location along their length and the tails swapped to create the new individuals. The process is outlined in figure 3.7.

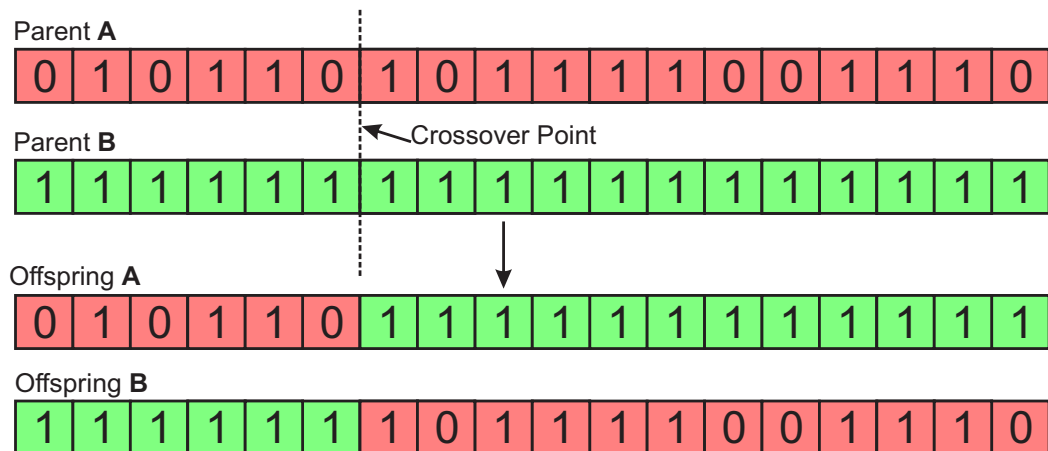


Figure 3.7: A single point crossover operation applied to a pair of binary strings. All data beyond the crossover point is swapped.

The proportion of parents strings which undergo the crossover operation is determined by the crossover probability,  $P_c$ . A random number is generated between zero and one and only if this number is greater than  $P_c$  is the crossover operation performed, in all other cases the individuals proceed unchanged.

The final genetic operator applied to the population is termed mutation. The mutation operator is required to maintain the genetic diversity of the population between generations. With each new generation the population is swept and one bit of the gene values inside an individual is altered from its initial state. The proportion of individuals that undergo mutation is determined by the mutation probability,  $P_m$ . The actual setting for,  $P_m$ , is likely to be highly problem dependant. If its value is set too high then the performance of the algorithm will be degraded to that of a crude random search. Schaffer et al [34] recommend the starting point defined by equation (3.3.2):

$$P_m = \frac{1}{N\sqrt{L}} \quad (3.3.2)$$

where  $N$  is the population size and  $L$  is the total length of the binary string used to represent each individual.

#### 3.3.1.4 Fitness Function

The fitness function evaluates the performance of each individual and assigns it a value. In the case of the Bragg reflector we are trying to maximise the magnitude of the input reflection coefficient. This was achieved by first performing the matrix multiplications required to produce a single  $ABCD$  matrix for the reflector and then using equations (3.3.3) to translate to S-Parameters:

$$S_{11} = \frac{A + B/Z_0 - CZ_0 - D}{A + B/Z_0 + CZ_0 + D} \quad (3.3.3)$$

The A,B,C,D terms represent the ABCD parameters of the compound reflector matrix and  $Z_0$  is the characteristic impedance of the measurement. The real valued magnitude,  $|S_{11}|$ , was then used as the measure of fitness.

The genetic algorithm was implemented in C++. A flow chart outlining the operation of the program is shown on in figure 3.8 on the following page.

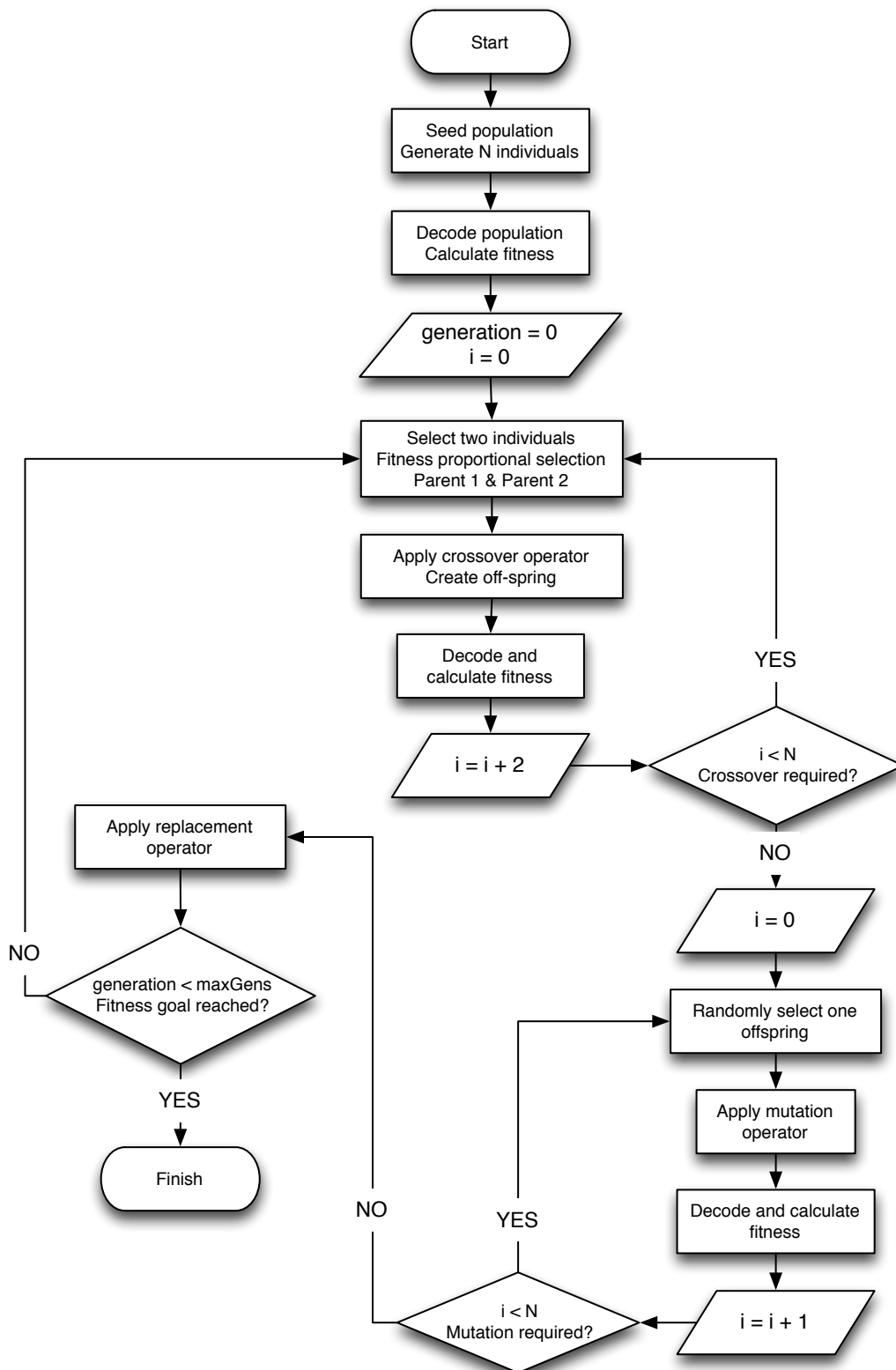


Figure 3.8: Flowchart for the genetic algorithm used to optimise the input reflection coefficient of the Bragg reflectors.

### 3.3.2 Optimised Aperiodic Resonator

With the optimisation algorithm implementation now specified, it is possible to optimise the quality factor of the Bragg resonator structure. An ABCD parameter model was constructed for one of the distributed reflectors. A block diagram of the model is shown in figure 3.9.

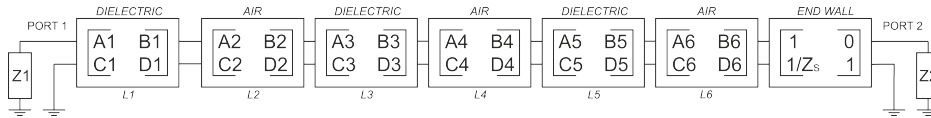


Figure 3.9: A waveguide ABCD parameter model for one half of a six plate Bragg resonator. The length of the air and dielectric sections of this structure are optimised to maximise the magnitude of the input reflection coefficient ( $S_{11}$ ).

The value of the port impedance,  $Z_1$ , was set equal to the wave impedance inside an air section. This is to ensure that we are representing a wave travelling from the central air region towards a dielectric plate. The value of terminating impedance,  $Z_2$ , is less critical due to the small impedance to ground presented by the end wall. However, its value must be large enough to avoid reducing the end wall impedance. The reflector section lengths were then optimised until the magnitude of the input reflection coefficient at port one ( $S_{11}$ ) reached a maximum. Several optimisation runs were performed and the crossover probability, mutation probability and population size were varied to see if different optima could be located. Convergence to the same solution was observed in the majority of cases. Table 3.3, specifies the optimal air and dielectric section thicknesses for a six plate aperiodic resonator. The algorithm parameters used to locate this solution are shown in table 3.4.

Section Identifier	Material Type	Length (mm)
L1	Dielectric	1.512
L2	Air	11.023
L3	Dielectric	1.887
L4	Air	9.300
L5	Dielectric	2.253
L6	Air	8.060
LC	Air	17.033

Table 3.3: Dielectric and air section reflector thicknesses for an optimised six plate Bragg resonator.

Parameter	Value
Population Size	100
Sub-String Length	26 bits
Total Sub-Strings	6
Crossover Probability	0.8
Mutation Probability	0.0026455
Number of Generations	5000
Total optimisation time	22 Sec
Parameter Range	0 mm to 100 mm

Table 3.4: Genetic algorithm parameters used during the six plate Bragg resonator optimisation. The mutation probability was calculated using equation (3.3.2).

With an optimal set of plate thicknesses found two of the reflectors can be combined and then the central air section re-introduced. The length of the central resonant region must be adjusted in order to restore the desired  $TE_{011}$  resonance to the correct frequency. This was achieved by calculating the additional phase shift required to restore the phase of the input reflection coefficient of each reflector to  $180^\circ$ . Equation (3.3.4) is used to perform this calculation:

$$\delta_d = 180^\circ - \angle S_{11} \quad (3.3.4)$$

The additional length that needs to be added to the central section,  $\delta L$ , can then be calculated using (3.3.5).

$$\delta_L = \frac{\lambda_g \delta_d}{360} \quad (3.3.5)$$

An S-Parameter simulation of the complete Bragg resonator was then performed. Using this optimised 6 plate structure it has been possible to design a cavity with a simulated unloaded quality factor of 400,000 at 10 GHz. This is 24% improvement when compared to the equivalent periodic Bragg resonator.

A second optimisation was performed on an eight plate structure and the resulting dielectric and air section thicknesses are shown in table 3.5. This structure achieved a quality factor of 421,963.

Section Identifier	Material Type	Length (mm)
L1	Dielectric	1.434
L2	Air	11.485
L3	Dielectric	1.642
L4	Air	10.930
L5	Dielectric	1.995
L6	Air	8.916
L7	Dielectric	2.299
L8	Air	7.386
LC	Air	17.097

Table 3.5: Dielectric and air section reflector thicknesses for an optimised eight plate Bragg resonator.

In order to ascertain how the optimisation procedure had redistributed the energy inside the cavity the voltage standing wave patterns were plotted for the six plate periodic and aperiodic resonators. Each wave guide section was subdivided into,  $n$ , smaller sections with the same constituent parameters but a reduced length. An ABCD matrix was generated for each of these sub-sections using equation (3.3.6).

$$\begin{bmatrix} V_1 \\ I_1 \end{bmatrix} = \begin{bmatrix} \cosh(\frac{\gamma l}{n}) & Z_0 \sinh(\frac{\gamma l}{n}) \\ \frac{1}{Z_0} \sinh(\frac{\gamma l}{n}) & \cosh(\frac{\gamma l}{n}) \end{bmatrix} \begin{bmatrix} V_2 \\ I_2 \end{bmatrix} \quad (3.3.6)$$

The reduce length sections were then combined to form the original resonator. This enabled the voltage distribution to be extracted by calculating the voltages at the nodes connecting the smaller sub-sections.

The voltage standing wave distributions inside the 10 GHz periodic and aperiodic Bragg resonators are shown in figures 3.10 and 3.11. The vertical lines indicate the locations of the edges of the dielectric plates. It is clearly visible that inside the periodic resonator, the voltage peaks occur inside the dielectric plates. However, in the aperiodic design these peaks are shifted into the the lower loss air sections. It is this re-distribution of the field pattern that results in the enhanced quality factor.

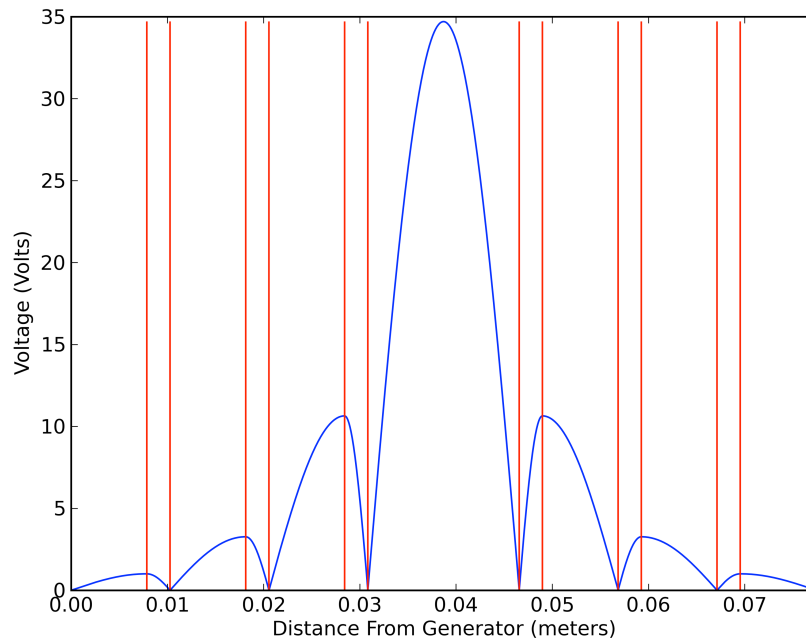


Figure 3.10: Voltage standing wave distribution inside the 6 plate periodic Bragg resonator.

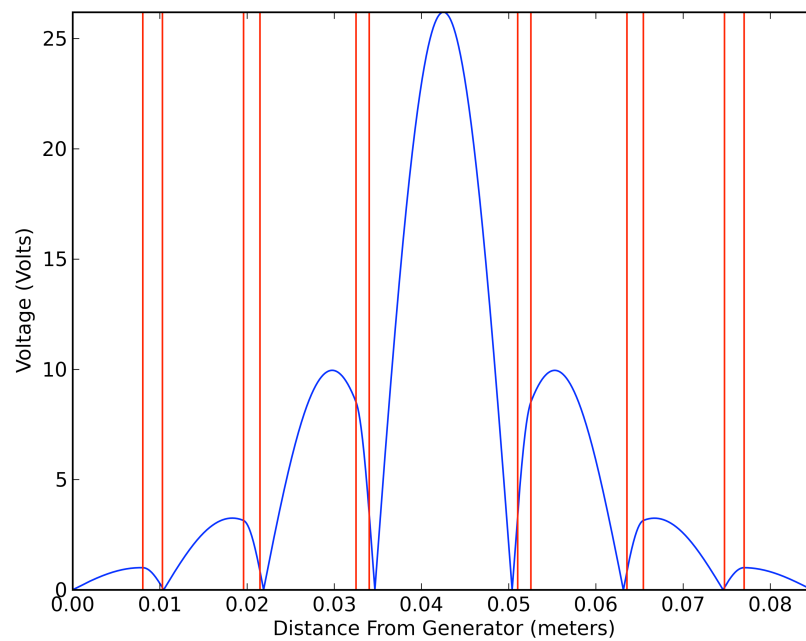


Figure 3.11: Voltage standing wave distribution inside the 6 plate aperiodic Bragg resonator.

### 3.4 Measurement Results

Using the model and simulation results described in the previous sections a cylindrical Bragg resonator was constructed using the aperiodic plate arrangement specified in table 3.3. A cross sectional view of the cavity is shown in figure 3.12.

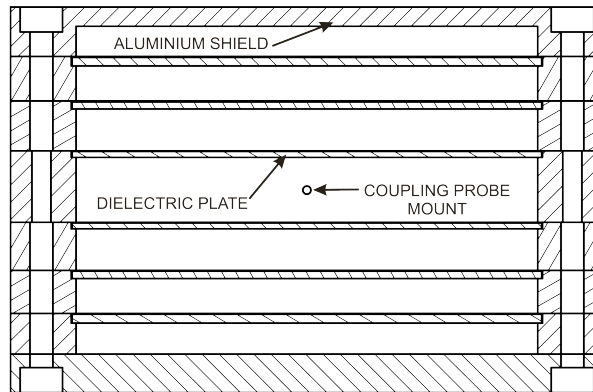


Figure 3.12: A cross section view of the six plate aperiodic Bragg resonator

This design consists of six dielectric plates mounted in an Aluminium shield. Aluminium was chosen because Silver plating was not available when the cavity was initially constructed. The reduced conductivity resulted in a theoretical optimum quality factor of 392,000, a reduction of 2% when compared to Silver design. Figure 3.13 shows a photo of the cavity with the lid removed, where one of the dielectric plates and the fixing holes are visible.

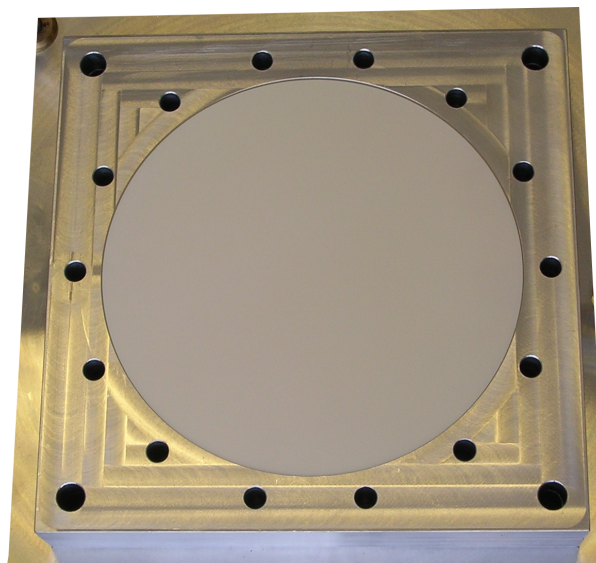


Figure 3.13: A-periodic Bragg resonator with the lid removed.

Wire loop probes were used to couple energy into the cavity. The orientation and position of the probes was adjusted in order to maximise the quality factor. This was achieved by connecting the resonator to a network analyser and continuously monitoring the S-Parameters while rotating and shifting the probes. The probes were clamped into place when the optimal quality factor had been achieved. A plot of the forward transmission coefficient scattering parameter ( $S_{21}$ ) is shown in figure 3.14. The wanted resonance can be seen at the centre of this plot. Several spurious modes are also clearly visible.

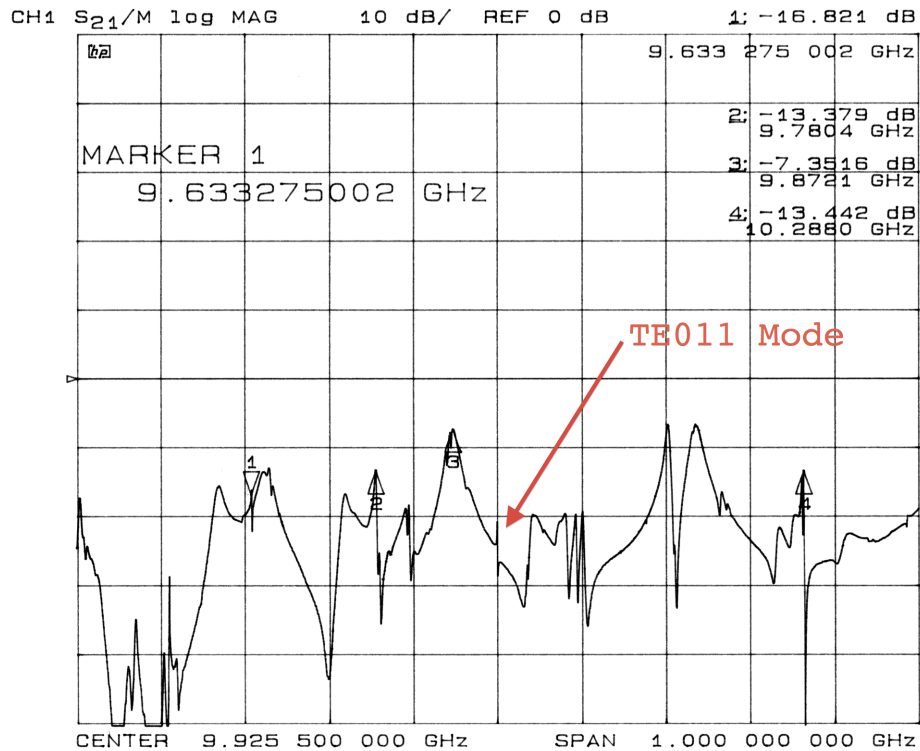


Figure 3.14: A plot of the forward transmission coefficient ( $S_{21}$ ) for the 6 plate aperiodic Bragg resonator. A frequency span of 1 GHz is shown.

A narrow band plot of the wanted  $TE_{011}$  resonant mode is shown in figure 3.15. It can be seen that the resonator has a centre frequency of 9.94 GHz with a loaded quality factor,  $Q_L$ , of 126,810 and an insertion loss,  $S_{21}$  of -8.98dB. If we assume equal input and output coupling then the unloaded quality factor,  $Q_0$ , can be calculated using equation (3.4.1)

$$Q_0 = \frac{Q_L}{(1 - S_{21})} \quad (3.4.1)$$

where  $Q_L$  is the loaded quality factor and  $S_{21}$  is the insertion loss as a voltage ratio. Substituting the values above gives an unloaded quality factor,  $Q_0$ , of

196,797.

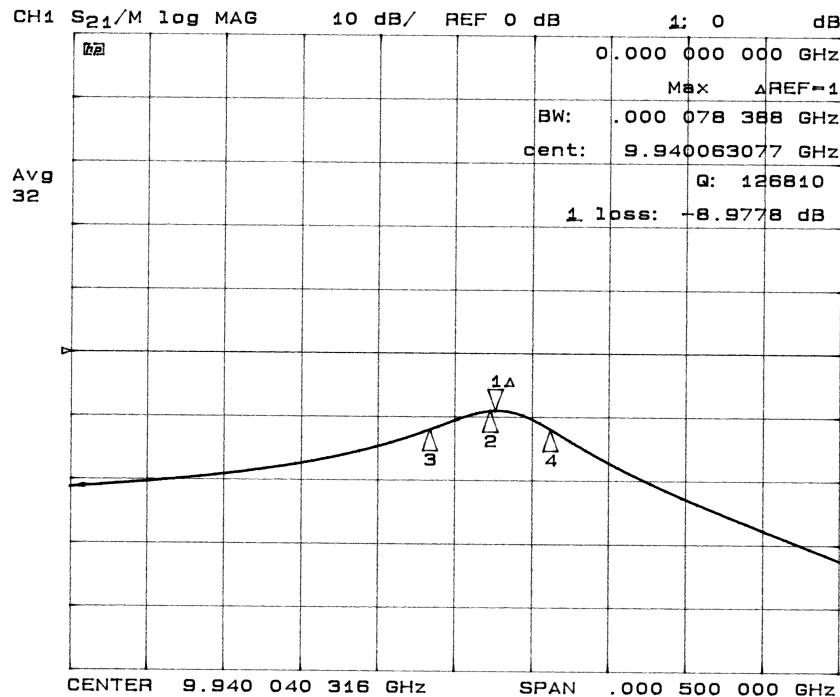


Figure 3.15: A narrow band plot of the forward transmission coefficient ( $S_{21}$ ) for the 6 plate aperiodic Bragg resonator. A frequency span of 500 kHz is shown.

The resonant frequency of 9.94 GHz is in good agreement with the simulated result of 10 GHz. It can be seen in from figure 3.15, that there are no spurious resonances within  $\pm 50$  MHz of the wanted resonance. The closest low loss unwanted mode is approximately 50 MHz lower than the wanted resonance; other low loss modes can also be seen 200 MHz higher in frequency. It is still possible to use this resonator in an oscillator, possibly with the inclusion of a lower Q broad band filter if required. This resonator may also find application as a discriminator for noise detection and reduction and in high Q filters. The unloaded quality factor of 196,797 is considerably lower than the simulated value of 400,000. There are several factors that could account for the reduced quality factor. The loss tangent of the Alumina plates may have been larger than the manufacturers specification resulting in increased dielectric losses. The Aluminium used to construct the shield may not have been 100% pure resulting in decreased electrical conductivity and increased end and side wall losses. Finally, the metal plates used to support the Alumina discs will have introduce discontinuities into the structure as well as providing small openings at their interfaces that could potentially radiate.

### 3.4.1 Tuneable Bragg Resonator

Theoretical simulations have predicted that this resonator could offer broad electro-mechanical tuning if the length of the centre section can be varied. This is because the Bragg mirrors produce fairly low loss reflectivity over a broad frequency range. Table 3.6 show the quality factor and resonant frequency for the  $TE_{011}$  mode in the 6-plate aperiodic Bragg resonator as a function of the central section length. These results are also graphed in figure 3.16.

Centre Section Length (mm)	Centre Frequency (GHz)	$Q_0$
13.027	11.6779	402688
14.027	11.2414	417899
15.027	10.8052	418806
16.027	10.3886	412247
17.027	9.9999	399998
18.027	9.6413	385654
19.027	9.3122	369532
20.027	9.0106	354750

Table 3.6: Quality factor and resonant frequency for the  $TE_{011}$  mode in the 6-plate aperiodic Bragg resonator as a function of the central section length.

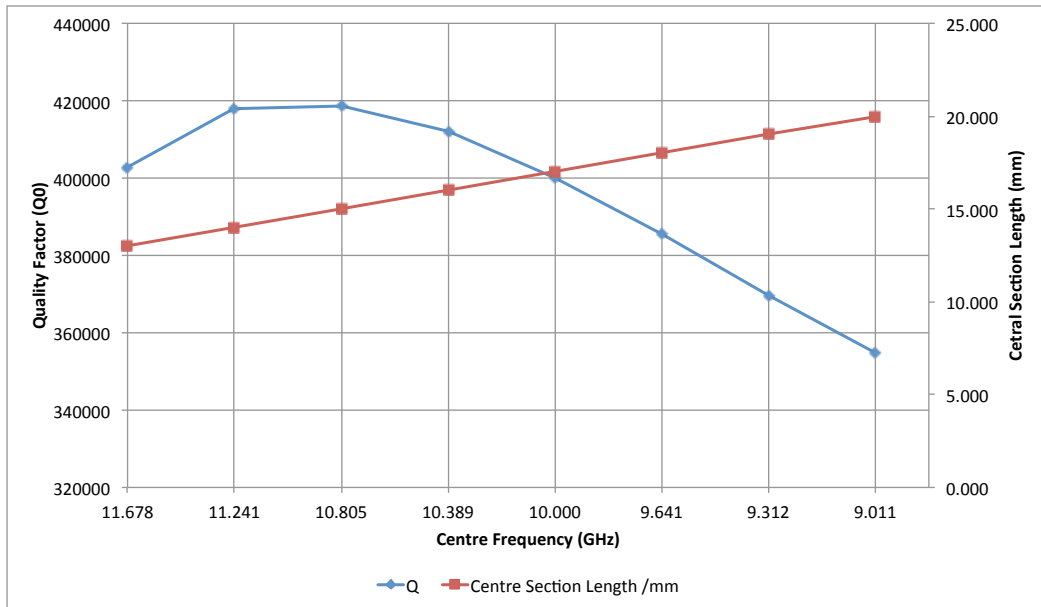


Figure 3.16: Quality factor and resonant frequency for the  $TE_{011}$  mode in the 6-plate aperiodic Bragg resonator as a function of the central section length.

A design for the tuneable structure is shown in figure 3.17. Here the two Bragg reflectors (top and bottom) are moved closer and further away from the

centre section (brown) while maintaining no line of sight exit for the wanted mode.

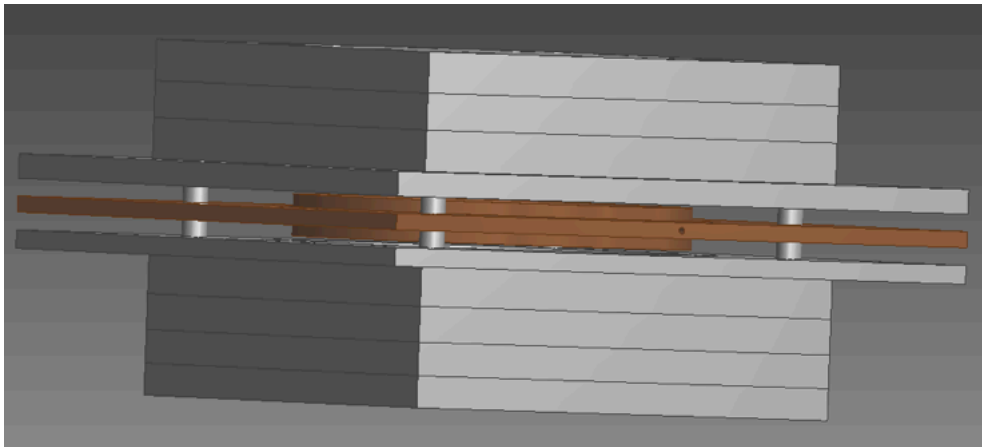


Figure 3.17: Tuneable distributed Bragg resonator.

Figure 3.18 shows the constructed tuneable Bragg resonator. Micrometers were used to tune the length of the central section and the S-Parameters were measured on a network analyser. Unfortunately the Q was degraded enormously, this was thought to be a result of the additional discontinuities introduced into the structure.

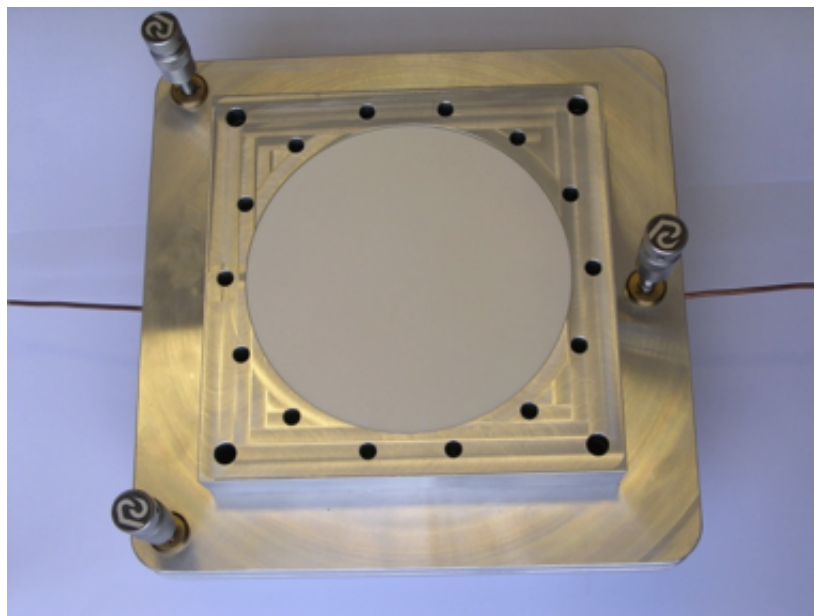


Figure 3.18: Tuneable distributed Bragg resonator with the lid removed. Micrometers were used to tune the length of the central section.

### 3.5 Numerical Field Solver

In order to determine a detailed field distribution inside the resonator cavity a custom finite difference time (FDTD) field solver was developed using the Java programming language. The FDTD method was developed by Kane S. Yee in 1966 [35]. It solves Maxwell's time dependant curl equations by replacing them with a set of finite difference equations. The method discretises the problem to be solved in both time and space by dividing the problem into a collection of two or three dimensional mesh cells. The cells size is selected such that the fields do not change significantly over a single increment, or more formally the dimensions of the cell must only be a fraction of a wavelength. The upper frequency limit of the problem must also be considered when determining a cell size as the Nyquist sampling criteria must not be violated. A general rule of thumb sets the minimum resolution, and thus the upper frequency limit, at ten cells per wavelength,  $\frac{\lambda_0}{10}$ . Once the cell size has been determined a time interval step-size can be selected to ensure computational stability. An excitation is then applied to the mesh and the difference equations are evaluated for each cell in the computational domain. The field inside the excitation cell then propagates throughout the FDTD mesh and the calculation continues until convergence has been achieved. For a finite time excitation this typically means that the residual field inside the structure has decayed to a sufficiently small level, -60 dB, from its peak value. The frequency response of the structure can then be calculated by taking the Fourier transform of the stored time domain data.

The FDTD method is a relatively simple code to implement and has a number of features that make it suitable for modelling complex structures:

- The computational domain can include lossy, lossless, and perfectly conduction materials as well as dielectrics, anisotropic and magnetic materials.
- A broadband frequency response can be calculated from a single simulation.
- It is capable of modelling arbitrarily complex structures formed from inhomogeneous materials assuming a small enough grid size and time-step can be selected.
- It has the accuracy of a second order approach without the need to solve simultaneous equations to compute the fields at the latest time-step [36].

One potential disadvantage of the FDTD method is its memory and computational requirements. For a three dimensional problem it is necessary to store seven values for each mesh point: the three electric field components,  $e_x$ ,  $e_y$ ,  $e_z$ , three magnetic field components  $h_x$ ,  $h_y$ ,  $h_z$  and an integer value used to index a matrix containing the permittivity, permeability and conductivity of the cell. If we assume double precision (8 byte) values for the field components and a 32 bit (4 byte) integer for the material index then each cell will require 52 bytes of memory. If we assume a three dimensional problem with  $N$  cells per wavelength where  $\lambda$  is the wavelength of the component with the highest frequency then the total memory requirements can be evaluated as:

$$RequiredBytes = 52 \times L_X \times L_Y \times L_Z \times \left(\frac{N}{\lambda_0}\right)^3 \quad (3.5.1)$$

For a simple FDTD implementation the computational requirements can be defined as [37]:

$$NFlops = 36 \times L_X \times L_Y \times L_Z \times \left(\frac{N}{\lambda_0}\right)^3 \quad (3.5.2)$$

It is easy to see from equations (3.5.1) and (3.5.2) that the memory and computational requirements can become prohibitively large for complex and/or large problems.

### 3.5.1 The Body of Revolution FD-TD Algorithm

The cylindrical resonator structure we are considering in this chapter is rotationally symmetric, this leads to the natural use of cylindrical coordinates. This type of problem can be solved using the FD-TD Body of Revolution (BOR) technique. This method expresses the azimuthal ( $\phi$ ) dependence of the fields as a Fourier series and as a result it is not necessary to mesh the problem in the  $\phi$  dimension. This means that the FD-TD BOR method can be considered a 2.5D technique with 2D computational resource requirements. A disadvantage of this method is that a separate solver run is required for each of the azimuthal modes that are to be investigated. In this problem we are primarily concerned with the  $TE_{01n}$  modes and as such only a single solver run is required.

As we are only considering the  $TE_{01n}$  modes the only field components required are  $e_\phi$ ,  $h_z$  and  $h_r$ . The mesh used for the finite difference time do-

main BOR computations is illustrated in figure 3.19. The field components, cell indexes, cell sizes, are all shown. The red circles and arrows represent the boundary conditions of the problem and are also set to zero in order to represent a perfect electrical conductor (PEC).

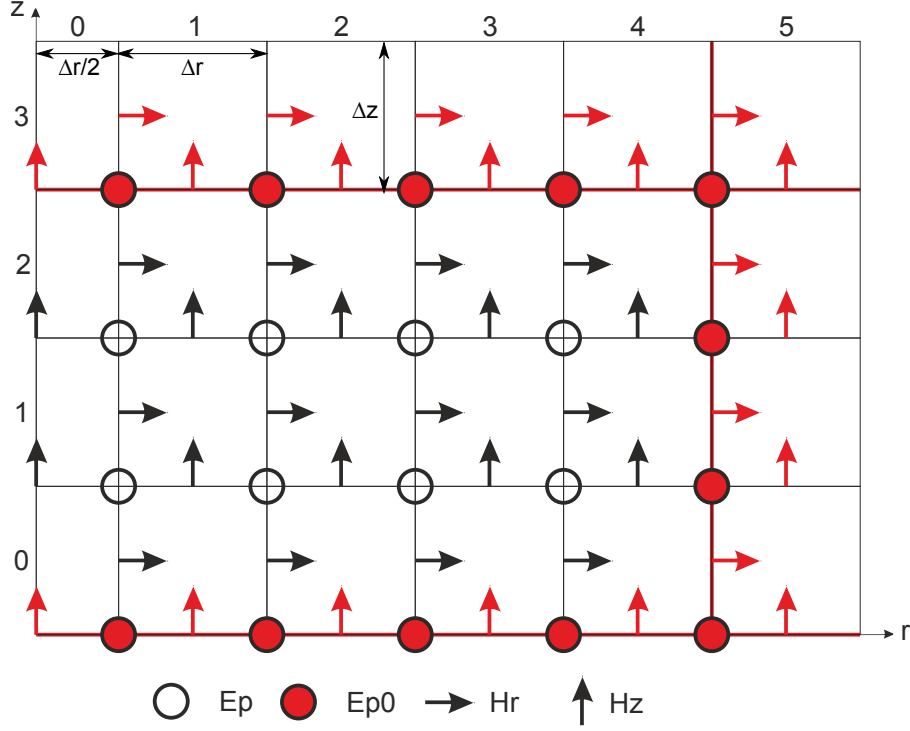


Figure 3.19: The finite difference mesh for BOR computations

The finite difference equations used are based on those derived by Chen, Mittra and Harms [38]. The required update equations are shown below in equations (3.5.3), (3.5.4) and (3.5.5):

$$E_{\phi}^{n+1}(i, j) = \frac{\left(1 - \frac{\sigma_{\phi} \Delta t}{2\epsilon_0 \epsilon_{\phi}}\right)}{\left(1 + \frac{\sigma_{\phi} \Delta t}{2\epsilon_0 \epsilon_{\phi}}\right)} E_{\phi}^n(i, j) + \frac{\left(\frac{\Delta t}{\epsilon_0 \epsilon_{\phi}}\right)}{\left(1 + \frac{\sigma_{\phi} \Delta t}{2\epsilon_0 \epsilon_{\phi}}\right)} \cdot \left[ \frac{H_r^{n+\frac{1}{2}}(i, j) - H_r^{n+\frac{1}{2}}(i, j-1)}{\Delta z} \right] \quad (3.5.3)$$

$$H_z^{n+\frac{1}{2}}(i, j) = H_z^{n-\frac{1}{2}}(i, j) + \left( \frac{m \Delta t}{\mu_0 \mu_z r_{i+\frac{1}{2}}} \right) E_r^n(i, j) - \frac{\Delta t}{\mu_0 \mu_z} \left[ \frac{r_{i+1} E_{\phi}^n(i+1, j) - r_i E_{\phi}^n(i, j)}{r_{i+\frac{1}{2}} \Delta r} \right] \quad (3.5.4)$$

$$H_r^{n+\frac{1}{2}}(i, j) = H_r^{n-\frac{1}{2}}(i, j) - \left( \frac{m\Delta t}{\mu_0\mu_r r_i} \right) E_z^n(i, j) + \frac{\Delta t}{\mu_0\mu_r} \left[ \frac{E_\phi^n(i, j+1) - E_\phi^n(i, j)}{\Delta z} \right] \quad (3.5.5)$$

With reference to figure 3.19 and the preceding three equations it can be seen that singularities occur for  $r = 0$ . These can be handled using the technique described in [39][38][40] where a half cell is used at the axis and the  $H_z$  component is calculated using Faraday's law. The required update equation is then:

$$H_z^{n+\frac{1}{2}}(0, j) = H_z^{n-\frac{1}{2}}(0, j) - \frac{4\Delta t}{\mu_0\mu_z\Delta r} E_\phi^n(1, j) \quad (3.5.6)$$

The spacial increment and time-step must be carefully selected in order to maintain numerical stability. The numerical stability boundary for the BOR algorithm described here can be empirically [36] represented using equation (3.5.7):

$$\Delta t \leq \frac{\Delta x}{sc} \quad (3.5.7)$$

where  $\Delta x$  is the spacial increment and  $s$  represent a stability factor that is dependant on the azimuthal mode number,  $m$ . For  $m > 0$ ,  $s \approx m + 1$  and for  $m = 0$ ,  $s = \sqrt{2}$ .

### 3.5.2 Quality Factor Computation

The Bragg resonator is an extremely high Q structure and in order to perform an accurate simulation we must correctly model the loss in the dielectric materials and metal walls. To correctly analyse the electromagnetic field interaction with the materials inside the cavity requires that we model the penetration of the fields into the interior of those materials. In the case of high conductivity metals the problem quickly becomes intractable. The skin effect dictates that the current density will be largest near the surface of a conductor, decreasing at greater depths. We can calculate the depth at which the current density will have fallen to  $1/e$  of its value at the surface using equation (3.5.8):

$$\delta = \sqrt{\frac{2\rho}{\omega\mu}} \quad (3.5.8)$$

where  $\rho$  is the resistivity of the conductor,  $\omega$  is the angular frequency of the current and  $\mu$  is the absolute magnetic permeability of the conductor. The

skin depth of silver at 10 GHz is 0.63  $\mu\text{m}$  which indicates that the fields must change very rapidly as they penetrate the surface of a metal. A very fine spacial grid will therefore be required in order to correctly model the loss in this material. Obviously this will lead to a lengthy computation time and significant resource usage.

There are a number of techniques that can be used in combination with FDTD method to approximate the loss in highly conducting materials. These include surface impedance boundary techniques [41][42][43] where the highly conducting material is replaced by a surface impedance boundary condition that is a function of the material parameters. This boundary condition eliminates the spacial quantisation associated with the object as well as potentially allowing smaller spacial step to be used in the remainder of the computational domain. An alternative technique is to use the perturbation method as described by Wang et al. [44]. If the material is sufficiently low loss then we can assume that fields at the surface of the lossy material are not sufficiently different from the lossless case. The quality factor for a low loss structure can be expressed as:

$$Q_c = \omega_0 \frac{W}{P_L} = \frac{2}{\delta} \left( \frac{\int_V \mu |H|^2 dV}{\oint_S \mu |H_t|^2 dS} \right) \quad (3.5.9)$$

$$Q_d = \omega_0 \frac{W}{P_d} = \omega_0 \left( \frac{\int_V \epsilon |E|^2 dV}{\int_V \sigma |E|^2 dV} \right) \quad (3.5.10)$$

where  $Q_c$  and  $Q_d$  are the quality factors associated with the conductive loss and dielectric loss respectively.  $W$  represents the maximum stored energy,  $P$  and  $P_d$  represent the average power loss associated with the conductive walls and dielectric.  $V$  represents the volume of the resonator,  $|H_t|$  is the magnetic field tangential to the resonator walls and  $\sigma$  is the skin depth of the conductor. The integrals of Equations (3.5.9) and (3.5.10) can be discretised as follows:

$$Q_c = \frac{2}{\delta} \left( \frac{\sum_{\Delta V} \mu(i, j) |F_H(i, j)|^2 \Delta V}{\sum_{\Delta S} \mu(i, j) |F_{H_t}(i, j)|^2 \Delta S} \right) \quad (3.5.11)$$

$$Q_d = \omega_0 \left( \frac{\sum_{\Delta V} \epsilon(i, j) |F_E(i, j)|^2 \Delta V}{\sum_{\Delta V} \sigma(i, j) |F_E(i, j)|^2 \Delta V} \right) \quad (3.5.12)$$

where  $F_E(i, j)$  and  $F_H(i, j)$  are the complex values of Fourier transforms of the E and H field at the mesh point  $(i, j)$ .  $F_{H_t}(i, j)$  is the Fourier transform of the tangential magnetic field on the surface of the conductor wall.

### 3.5.3 Simulation Procedure

Energy is coupled into the FDTD mesh using an internal field source. This source is implemented by specifying the value of  $e_\phi$  field at a specific node with a temporal driving function. In order to avoid the introduction a DC component into the simulation a bi-polar source is required. A Gaussian modulated sine pattern is used as this signal has no DC component, is time-limited and has a finite-bandwidth. Equations (3.5.13) and (3.5.14) describe a discrete time implementation of this source.

$$V_i = Ae^{-k(i\Delta t-d)^2} \cos [2\pi f_c(i\Delta t - d)] \quad (3.5.13)$$

where  $A$  is the peak amplitude of the signal,  $d$  is the initial delay,  $i$  is the sample index,  $\Delta t$  is the time-step and  $k$  is a constant given by:

$$k = \frac{5\pi^2 b^2 f_c^2}{q \ln(10)} \quad (3.5.14)$$

where  $b$  is the normalised bandwidth of the signal and  $q$  is the attenuation factor. Frequency domain and time domain plots for this signal are shown in Figure 3.20.

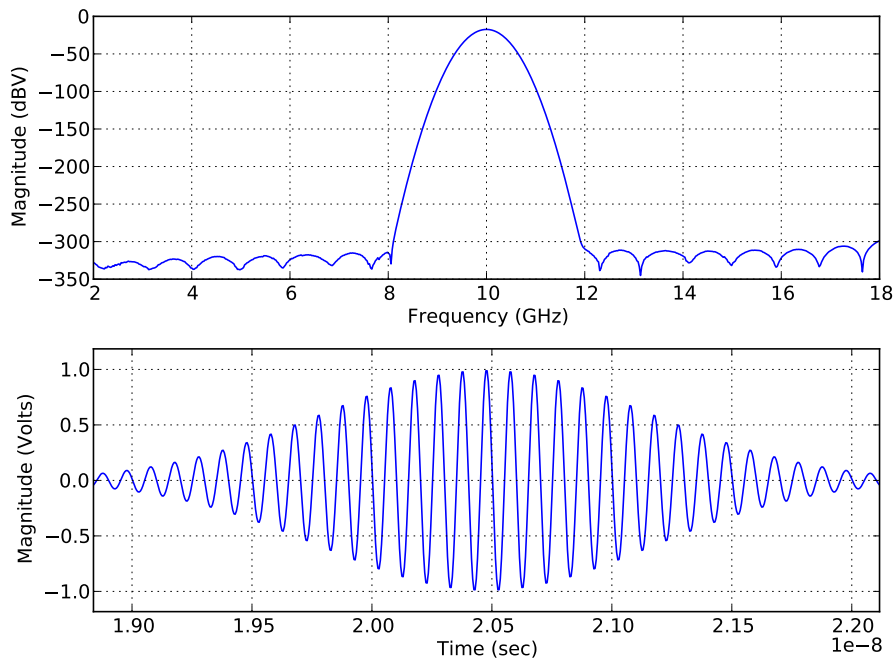


Figure 3.20: Frequency domain (Top) and time domain (Bottom) plots of a Gaussian modulated sine signal as described by equations (3.5.13) and (3.5.14)

Since the field value at the source node is specified solely by the excitation signal it will scatter any energy incident upon it. In order to reduce the effects of this problem the source is removed from the simulation after it has decayed to zero and the normal update equations are then applied. This approach relies on the fact that the reflections from the material structure have not propagated back to the source before it is switched off. In any case for a model containing a large number of cells the source cell will reflect a very small fraction of the total energy in the FDTD grid and is therefore unlikely to significantly degrade the accuracy of the simulation results.

An efficient implementation of the BOR FDTD equations is extremely important so that the simulation time is minimised. Several steps were taken to ensure that this was the case. In order to avoid the significant time penalty associated with floating-point division the conductivity terms in the update equations (3.5.3), (3.5.4), (3.5.5) and (3.5.6) were pre-calculated and stored in a look-up table. The coefficient and field data matrices are stored in one dimensional arrays allocated from a continuous chunk of memory. The data in these arrays is stored in row-major order and accessed using the style shown in equation (3.5.15):

$$x[i, j] = x[(i \times cols) + j] \quad (3.5.15)$$

where  $i$  is the row index,  $j$  is the column index and  $cols$  is the total number of columns in the matrix. It is most efficient to access this array one row at a time, that is to say that the row index,  $j$ , should be incremented over its full range before the column index is incremented. This is a consequence of the way memory is stored and accessed by the CPU. Modern CPUs access memory in chunks called pages. When the CPU requires access to a value in the field matrix it will first check if the value is available in a small fast area of memory located on the CPU die called the cache. If it cannot locate the value in the cache then a cache miss occurs and a page fault is generated. The page containing the required value will then be read from main memory and stored in the cache. Servicing this page fault can be many orders of magnitude slower than reading directly from the cache. A memory page is typically many kilobytes in size and will therefore contain many values, if we access the array elements consecutively then it is much more likely that the value will already be in the cache and any subsequent operations will be much faster.

The excitation pulse describe previously contains energy at many different

frequencies and will therefore excite many modes inside the cavity. As the field structure evolves any energy that does not belong to a resonant frequency will decay rapidly. A Fourier transform is used to isolate the frequency components belonging to the mode we are interested in. In this work a simple discrete Fourier transform is used rather than more complicated FFT algorithm. The one dimensional DFT for a real valued input signal is defined in rectangular form as:

$$X(m) = \sum_{n=0}^{N-1} x(n) \left[ \cos\left(\frac{2\pi nm}{N}\right) - j \sin\left(\frac{2\pi nm}{N}\right) \right] \quad (3.5.16)$$

where  $n$  is the index of the time domain sample  $x(n)$ ,  $m$  is the index of the DFT output  $X(m)$  in the frequency domain and  $N$  is the total number of samples. Equation 3.5.16 is easily implemented in code as a pair of "running" sums. The computational efficiency of the implementation can be improved by storing the constants  $\cos(\frac{2\pi nm}{N})$  and  $-\sin(\frac{2\pi nm}{N})$  in a look-up table before the simulation begins. In this application the primary advantage of using the DFT when compared to the more computationally efficient FFT is that there is no need to store the entire time history of the simulation. It should be noted that in many FDTD problems the DFT is more efficient both in terms of computational time and backing store than the FFT [45]. The full simulation procedure is outlined in steps one to seven below:

1. Define the problem geometry, and calculate the maximum stable time step and spacial increment.
2. Allocate and clear the required memory for the time domain field data, material parameters, solver coefficients, DFT coefficients and frequency domain field data.
3. Calculate the solver and DFT coefficients and populate the look-up tables.
4. Calculate the value of the input excitation and set the value of the appropriate mesh cell.
5. Apply the  $e_\phi$ ,  $h_r$  and  $h_z$  field update equations to the entire mesh at the current time-step.
6. Update the DFT sum of each mesh cell using the new time domain field data.

7. Calculate the Q-Factor of the structure.
8. Iterate over items 4, 5, 6 and until the quality factor has stabilised or the fields have reduced by 60dB from their peak values.

### 3.5.4 Simulator Verification

A simple air filled cylindrical resonator was used to validate the simulator. This test structure has an analytical solution that describes the resonant frequency and quality factor, a comparison of the simulated and calculated values is presented in this section.

The resonant frequency for the transverse electric,  $TE_{mnl}^Z$ , modes of a cylindrical resonator cavity with radius  $a$  and height  $d$  can be calculated [46] using equation 3.5.17:

$$(f_r)_{mnl}^{TE^Z} = \frac{c}{2\pi\sqrt{\mu\epsilon}} \sqrt{\left(\frac{p'_{nm}}{a}\right)^2 \left(\frac{l\pi}{d}\right)^2} \quad (3.5.17)$$

where  $\mu$  and  $\epsilon$  are, respectively, the permeability and permittivity of the material filling the guide and  $p'_{nm}$  represents the  $n$ th zero of the derivative of the Bessel function of the first kind of order  $m$ . In the case of the  $TE_{011}$  mode  $p'_{nm} = 3.8318$  [47]. The quality factor,  $Q_c$ , for the transverse electric modes of a cylindrical cavity with imperfectly conducting walls but lossless dielectric can be derived using perturbation theory[46] as:

$$Q_c = \frac{(ka)^3 \eta a d}{4(p'_{nm})^2 R_s} \frac{1 - \left(\frac{n}{p'_{nm}}\right)^2}{\left(\frac{ad}{2} \left[1 + \left(\frac{\beta a n}{(p'_{nm})^2}\right)^2\right] + \left(\frac{\beta a^2}{p'_{nm}}\right)^2 \left(1 - \frac{n^2}{(p'_{nm})^2}\right)\right)} \quad (3.5.18)$$

where the propagation constant is,  $\beta = \frac{l\pi}{d}$ , the wave number is  $k = \omega\sqrt{\mu\epsilon}$ , the intrinsic impedance is  $\eta = \sqrt{\frac{\mu}{\epsilon}}$  and the surface resistivity of the cavity walls is  $R_s = \frac{\omega\mu}{2\sigma}$ . The total cavity quality factor,  $Q$ , which includes the dielectric losses can be computed using equation (3.5.19):

$$Q = \left(\frac{1}{Q_c} + \frac{1}{\tan \delta}\right)^{-1} \quad (3.5.19)$$

Using these equation we can compute the dimensions and quality factor for an air filled cylindrical cavity with the  $TE_{011}$  resonant mode present at 10 GHz. The cavity and simulation parameters are defined below in table 3.7:

Parameter	Symbol	Value
Operating frequency	$(f_r)_{011}^{TEZ}$	9.997 GHz
Quality Factor - Analytical	$Q$	13223
Cavity radius	$a$	60 mm
Cavity height	$d$	15.738 mm
Wall surface resistivity	$R_s$	0.0253 $\Omega$
Radial grid cells	$R$	120
Axial grid cells	$Z$	100
Radial step size	$\Delta r$	$5.063 \times 10^{-4}$
Axial step size	$\Delta z$	$1.590 \times 10^{-4}$
Time step	$\Delta t$	$3.750 \times 10^{-13}$
Source centre frequency	$f_c$	10.0 GHz
Source bandwidth	$b$	1000 MHz

Table 3.7: Specification for an air filled cylindrical resonator cavity with silver plated walls operating with the  $TE_{011}$  mode at 10 GHz

These parameters were programmed into the BOR solver and the quality factor, resonant frequencies and field distributions were calculated. Time domain data was collected from a single  $e_\phi$  cell located at the centre of the computational domain.

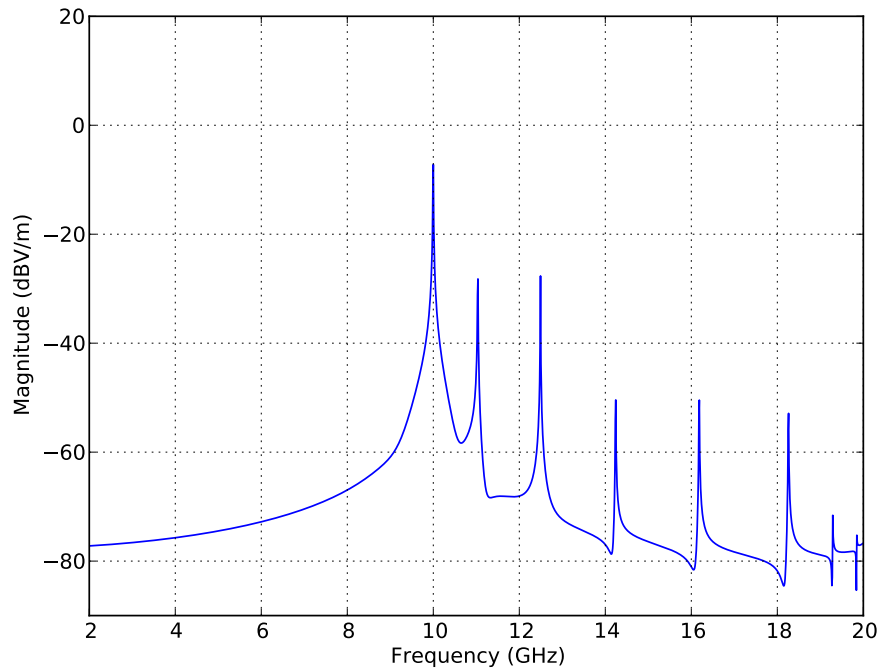


Figure 3.21: Frequency response of the air filled cylindrical cavity after 262,144 iterations.

Figure 3.21 shows a frequency domain plot of the structure after 262,144 iterations. This corresponds to an approximate DFT resolution bandwidth of  $\approx 10$  MHz. The  $TE_{011}$  resonant mode is clearly visible at 10 GHz, as are the  $TE_{021}$  and  $TE_{031}$  modes at 11.03 GHz and 12.49 GHz respectively. Figures 3.22, 3.23 and 3.24 show 2D plots of the magnitude of the  $E_\phi$ ,  $H_r$  and  $H_z$  field distributions inside the cavity at 10 GHz. These plots demonstrate the presence of the  $TE_{011}$  mode at 10 GHz:

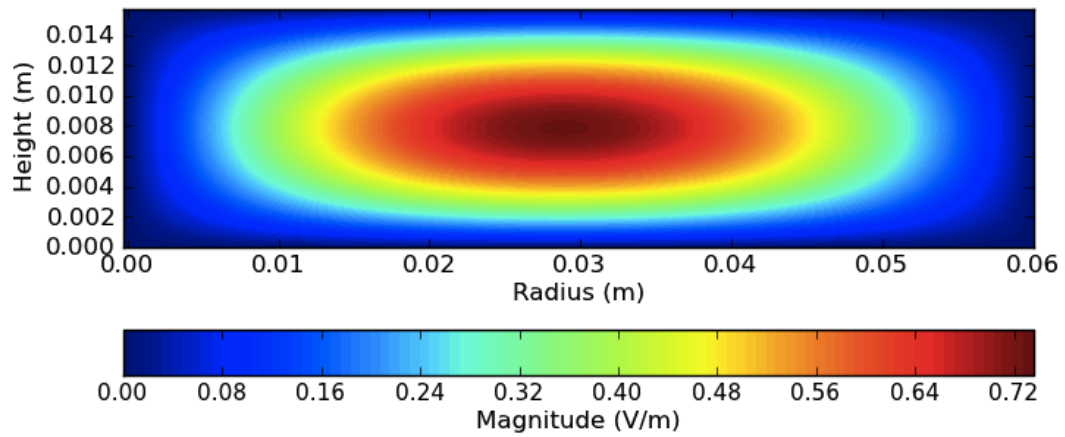


Figure 3.22: Plot of the magnitude of the  $E_\phi$  field inside the air filled cylindrical cavity resonator at 10 GHz.

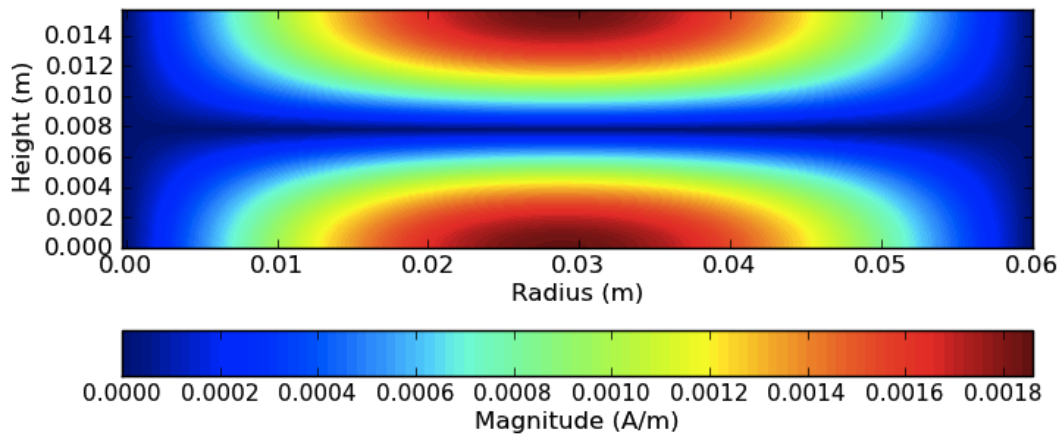


Figure 3.23: Plot of the magnitude of the  $H_r$  field inside the air filled cylindrical cavity resonator at 10 GHz.

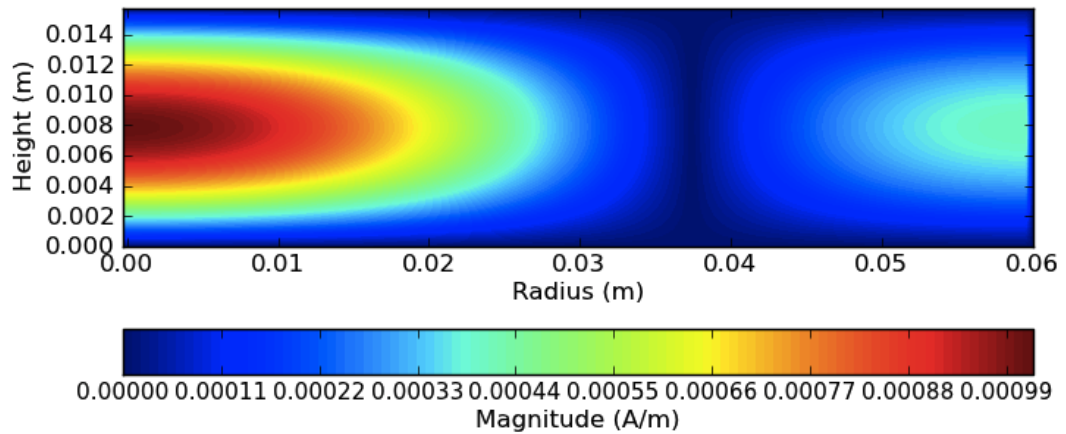


Figure 3.24: Plot of the magnitude of the  $H_z$  field inside the air filled cylindrical cavity resonator at 10 GHz.

The perturbation method described in section 3.5.2 was used to calculate the Q factor of the cavity at each time step. A plot of the data is shown in figure 3.25:

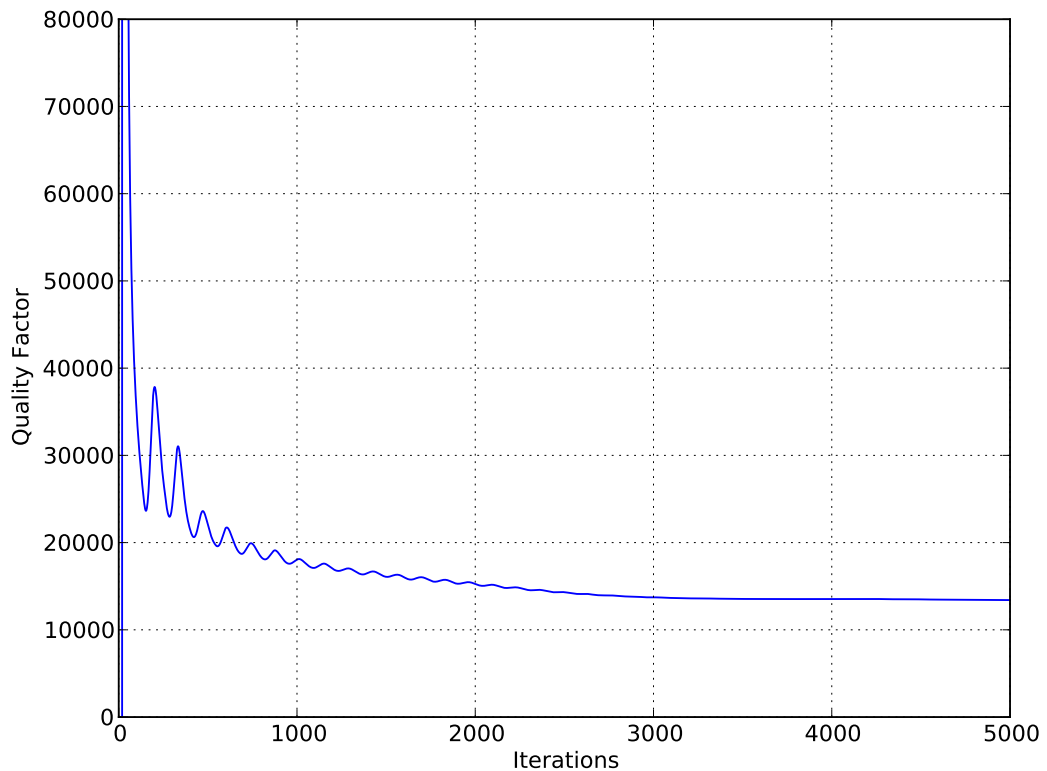


Figure 3.25: Simulated quality factor of the air filled cylindrical cavity resonator. The Q factor was calculated using the perturbation method at each iteration of the BOR solver.

It is clearly visible that by 3000 iterations the Q factor has converged to a value of 13,300. This is good agreement with the analytical value of 13,223. It should be noted that the simulation was not run for long enough to allow the fields to decay to the extent that the natural response of the cavity would have been dominant. This is un-necessary when using the perturbation method to calculate the quality factor as it is the field structure and shape that is important and not the absolute magnitude of the fields.

### 3.5.5 Periodic Bragg Resonator Field Simulation

In order to determine a detailed field distribution inside the periodic Bragg resonator a BOR field simulation was performed. The cavity specifications are those outlined in table 3.1 and the simulation parameters are shown in table 3.8. A wide-band source was used in order to excite any spurious modes.

Parameter	Symbol	Value
Radial grid cells	$R$	120
Axial grid cells	$Z$	800
Radial step size	$\Delta r$	$5.063 \times 10^{-4}$ m
Axial step size	$\Delta z$	$9.688 \times 10^{-5}$ m
Time step	$\Delta t$	$2.285 \times 10^{-13}$ s
Source centre frequency	$f_c$	10.0 GHz
Source 6 dB bandwidth	$b$	1000 MHz

Table 3.8: BOR field solver simulation parameters for the periodic Bragg resonator.

Figure 3.26 shows a frequency domain plot of the structure after 100,000 iterations. The  $TE_{011}$  resonant mode is clearly visible at 10 GHz, as are many additional spurious modes.

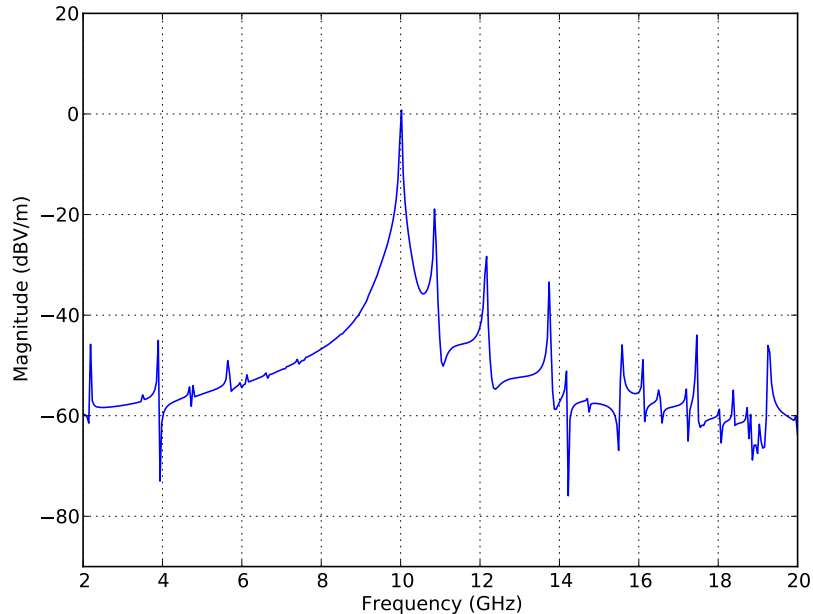


Figure 3.26: Frequency response of the periodic Bragg resonator after 100,000 iterations.

The perturbation method was again used to calculate the Q factor of the cavity at each time step. A plot of the data is shown in figure 3.27 where it is clearly visible that by 80000 iterations the Q factor has converged to a value of 310,000. This is reasonable agreement with the value of 322,579 calculated using the ABCD parameter model and represents an error of around 4 %.

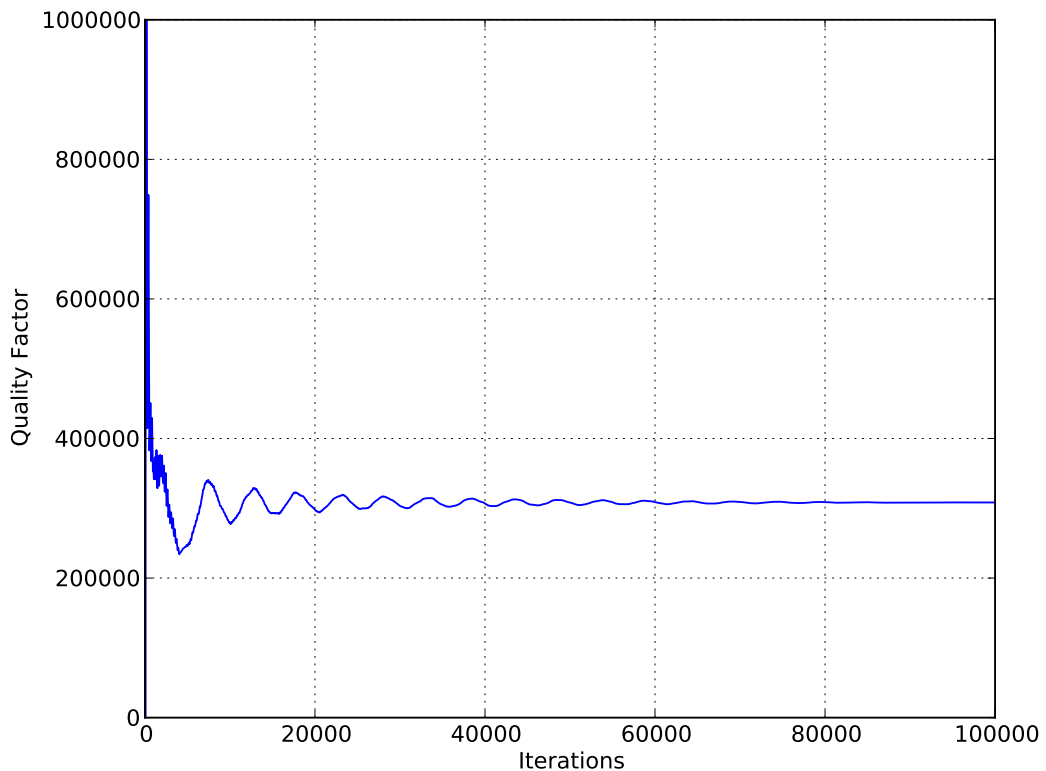


Figure 3.27: Simulated quality factor of the periodic Bragg resonator. The Q factor was calculated using the perturbation method at each iteration of the BOR solver.

Figures 3.28 to 3.30 on pages 74 and 75 and show 2D plots of the magnitude of the  $E_\phi$ ,  $H_r$  and  $H_z$  field distributions inside the cavity at 10 GHz. These plots show the presence of the  $TE_{011}$  mode as well as demonstrating the field confinement afforded by the Bragg reflectors.

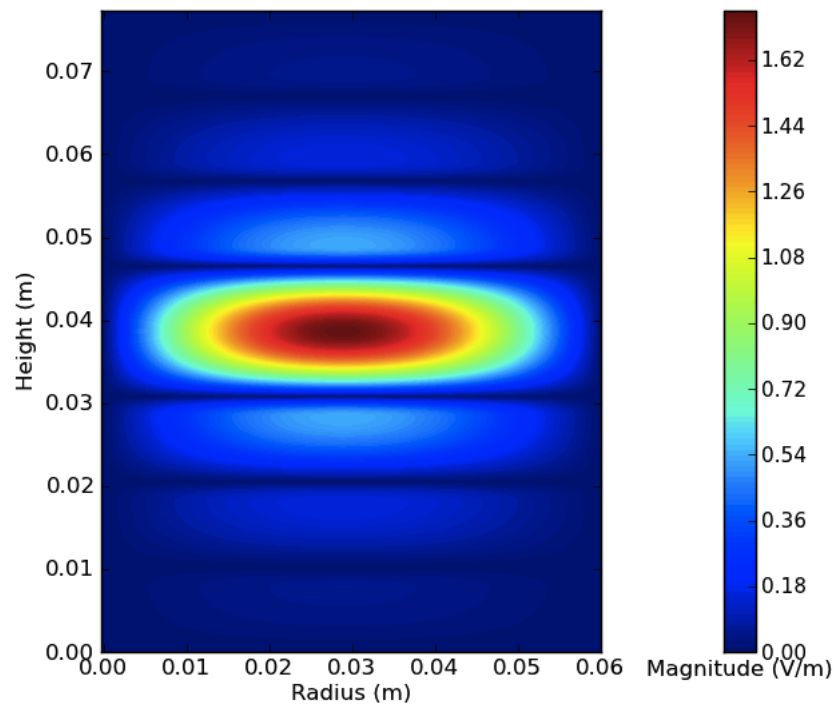


Figure 3.28: Plot of the magnitude of the  $E_\phi$  field inside the periodic Bragg resonator at 10 GHz.

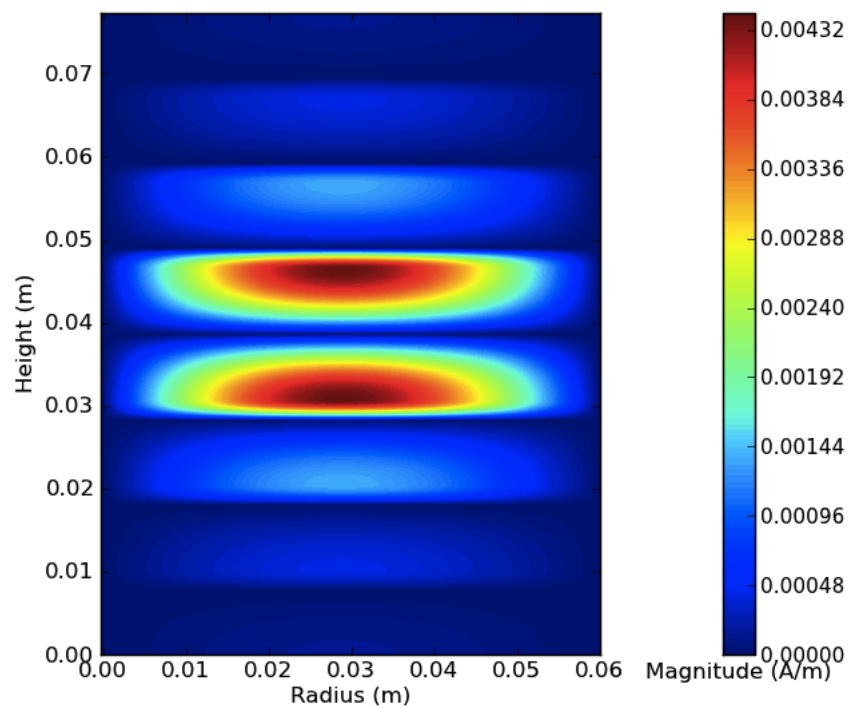


Figure 3.29: Plot of the magnitude of the  $H_r$  field inside the periodic Bragg resonator at 10 GHz.

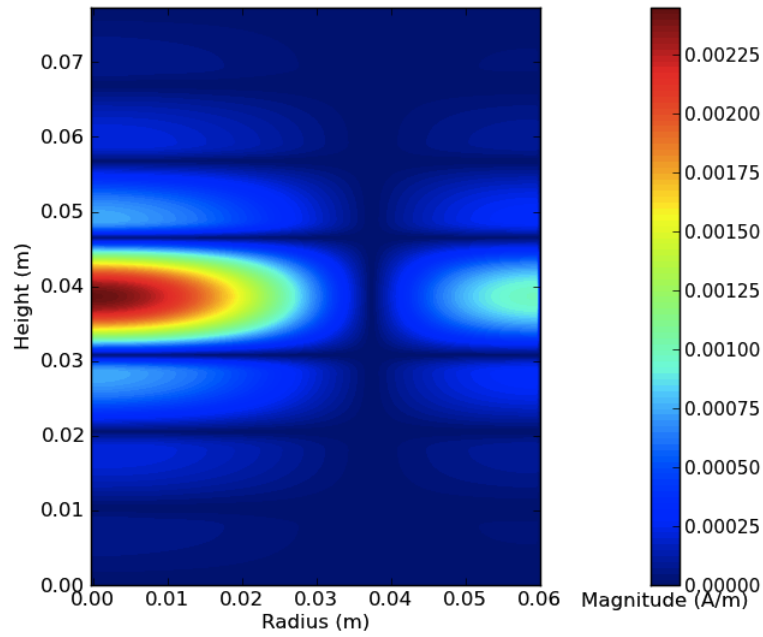


Figure 3.30: Plot of the magnitude of the  $H_z$  field inside the periodic Bragg resonator at 10 GHz.

Figure 3.31 shows a Line plot of the magnitude of the  $E_\phi$  field along the axis of the periodic Bragg resonator. If we compare this figure to the voltage standing wave distribution plotted using the ABCD waveguide model it can again be seen that the peaks of the field occur inside the lossy dielectric plates.

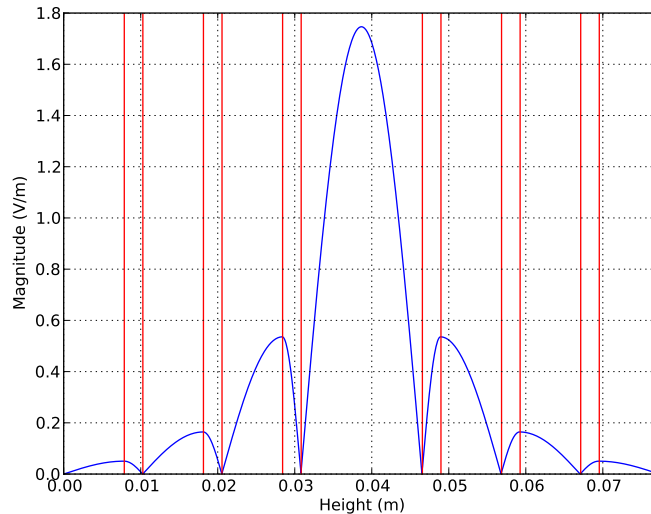


Figure 3.31: Line plot of the magnitude of the  $E_\phi$  field along the axis of the periodic Bragg resonator

### 3.5.6 aPeriodic Bragg Resonator Field Simulation

This section presents the results of a field simulation of the aperiodic Bragg resonator. The cavity specifications are those outlined in table 3.3 and the simulation parameters are shown in table 3.9.

Parameter	Symbol	Value
Radial grid cells	$R$	120
Axial grid cells	$Z$	800
Radial step size	$\Delta r$	$5.063 \times 10^{-4}$ m
Axial step size	$\Delta z$	$1.065 \times 10^{-4}$ m
Time step	$\Delta t$	$2.512 \times 10^{-13}$ s
Source centre frequency	$f_c$	10.0 GHz
Source bandwidth	$b$	1000 MHz

Table 3.9: BOR field solver simulation parameters for the periodic Bragg resonator.

Figure 3.32 shows a frequency domain plot of the structure after 200,000 iterations. The  $TE_{011}$  resonant mode is clearly visible at 10 GHz, as are many additional spurious modes.

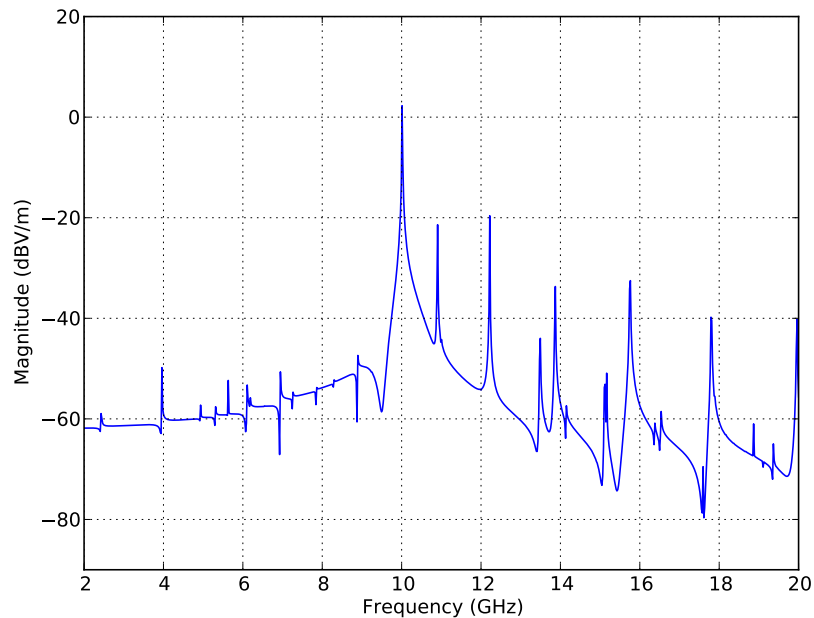


Figure 3.32: Frequency response of the aperiodic Bragg resonator after 100,000 iterations.

The perturbation method was again used to calculate the Q factor of the cavity at each time step. A plot of the data is shown in figure 3.33 where it is clearly visible that by 150,000 iterations the Q factor has converged to a value of 340,000. This is considerably lower than the predicted value of 400,000. The cause of this is thought to be the overly simplistic end wall model used in the ABCD waveguide simulations. This model seems to underestimate the end wall losses and as results the optimisation algorithm has incorrectly sized the dielectric plates. This effect was not observed in the periodic Bragg field simulation as the end wall losses form a smaller portion of the total losses. This is because the high field regions are located closer to the centre of the cavity in the periodic resonator.

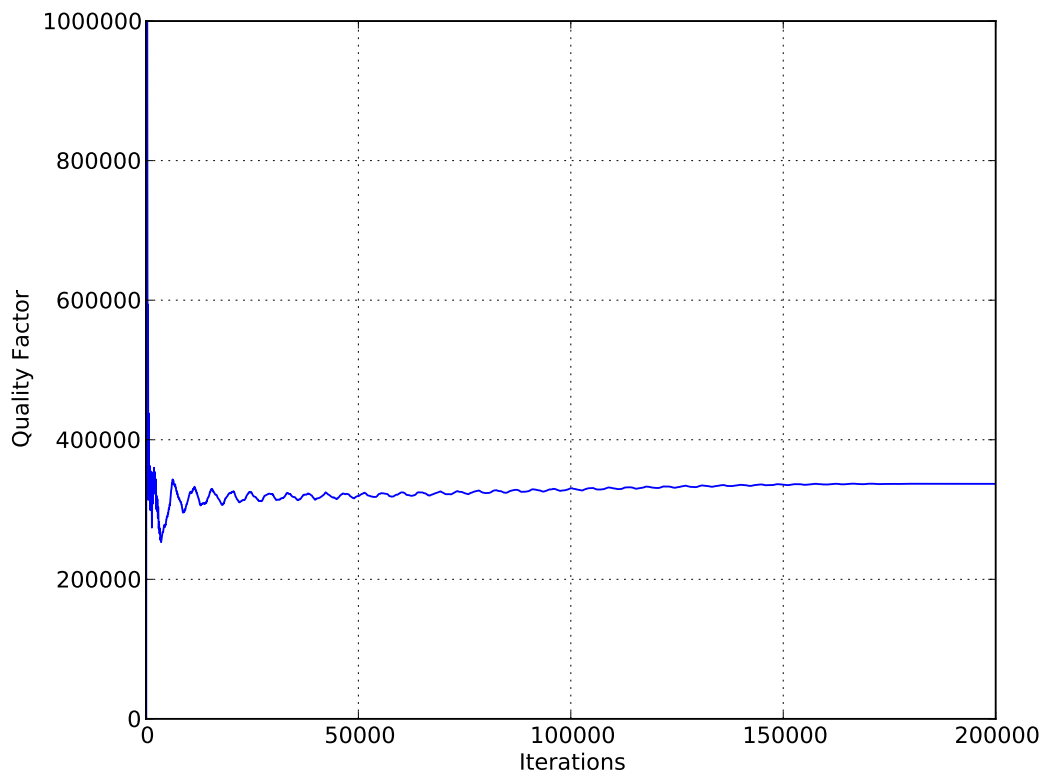


Figure 3.33: Simulated quality factor of the aperiodic Bragg resonator. The Q factor was calculated using the perturbation method at each iteration of the BOR solver.

Figures 3.34 to 3.36 on pages 78 and 79 and show 2D plots of the magnitude of the  $E_\phi$ ,  $H_r$  and  $H_z$  field distributions inside the cavity at 10 GHz. These plots show the presence of the  $TE_{011}$  mode at 10 GHz. If we compare this figure to the  $E_\phi$  field distribution inside the periodic resonator then we can see an increased field strength inside the air regions.

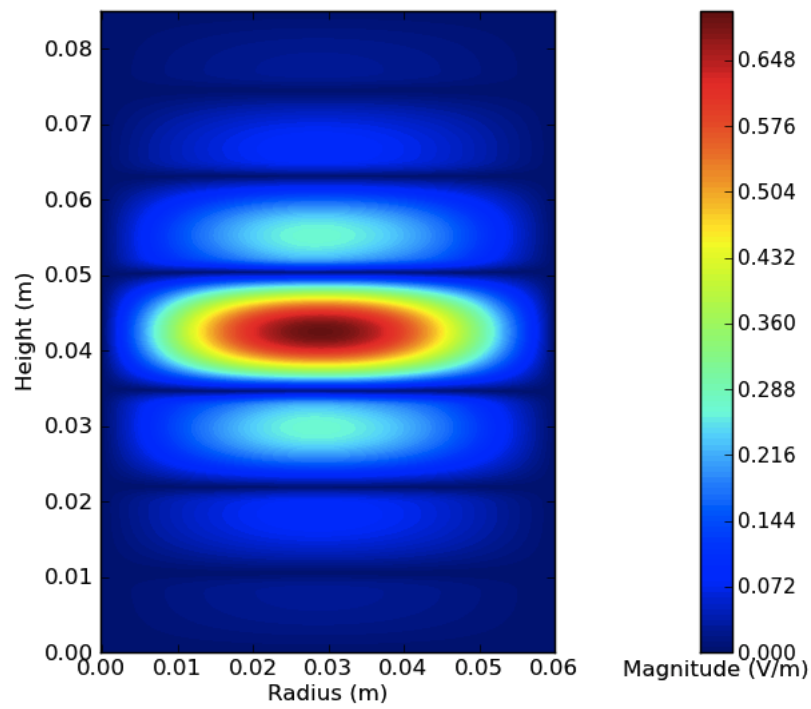


Figure 3.34: Plot of the magnitude of the  $E_\phi$  field inside the aperiodic Bragg resonator at 10 GHz.

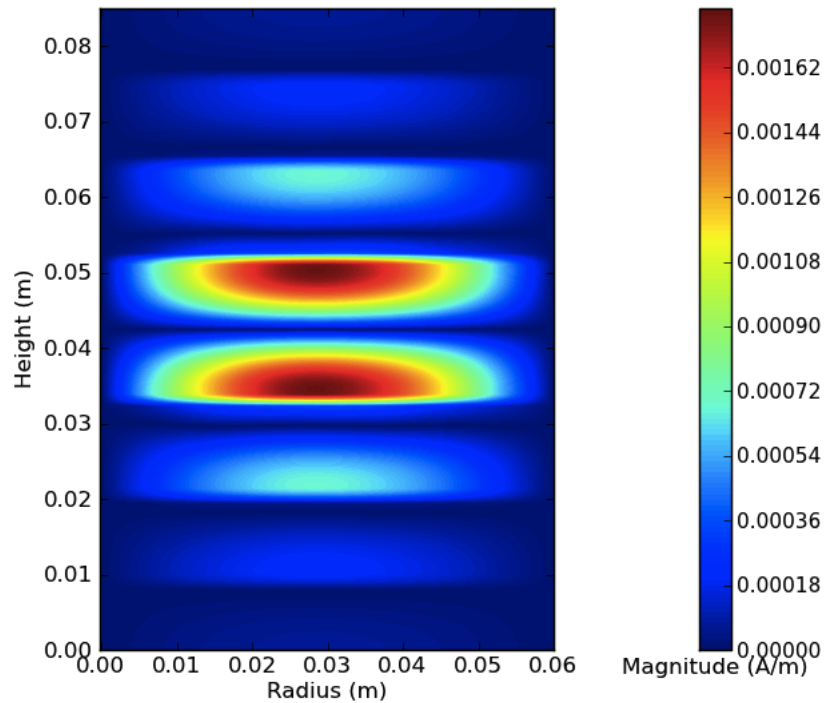


Figure 3.35: Plot of the magnitude of the  $H_r$  field inside the aperiodic Bragg resonator at 10 GHz.

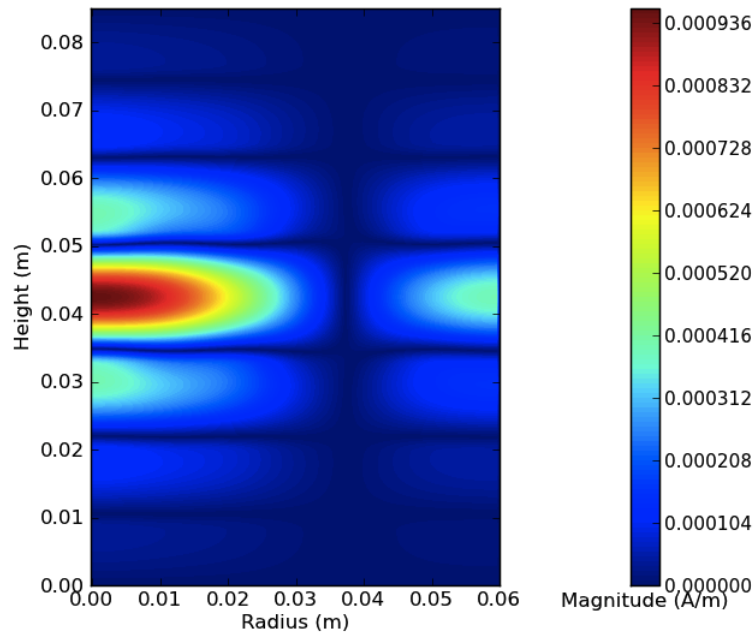


Figure 3.36: Plot of the magnitude of the  $H_z$  field inside the aperiodic Bragg resonator at 10 GHz.

Figure 3.37 shows a Line plot of the magnitude of the  $E_\phi$  field along the axis of the aperiodic Bragg resonator. It can be seen that for the first and second set of dielectric plates the field peak has been shifted into the lower loss air region. This effect is not as pronounced in third pair of plates.

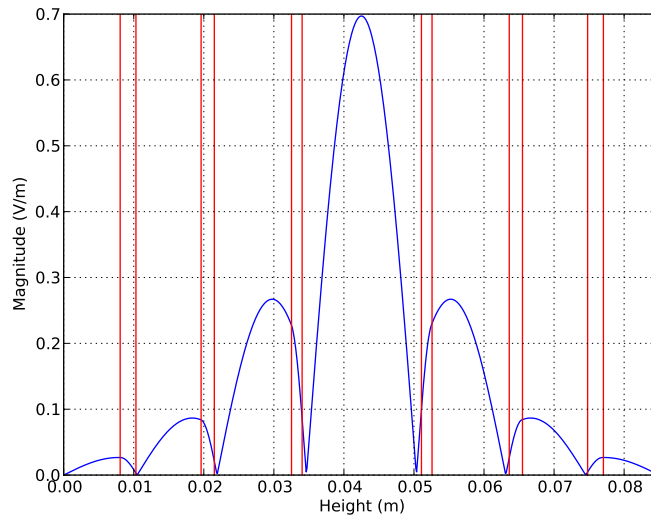


Figure 3.37: Line plot of the magnitude of the  $E_\phi$  field along the axis of the aperiodic Bragg resonator

Figures 3.38 and 3.39 show comparisons between the voltage standing wave distributions predicted by the ABCD models (green traces) and the magnitude of the  $E_\phi$  field along the axis of the resonators (blue traces). These plots were created by normalising each distribution by the peak field magnitude or voltage produced by the simulator. In the case of the aperiodic resonator it is clearly visible that the ABCD model predicts a higher peak field magnitude in the air filled regions between the first and second and second and third plates. The cause of this is thought to be simplistic end wall model used by the ABCD waveguide simulator which underestimates the end wall losses. In the case of the periodic resonator it can be seen that the both models are in good agreement. The effect of the end wall models in these simulations is less significant as the end wall losses form a smaller portion of the total losses.

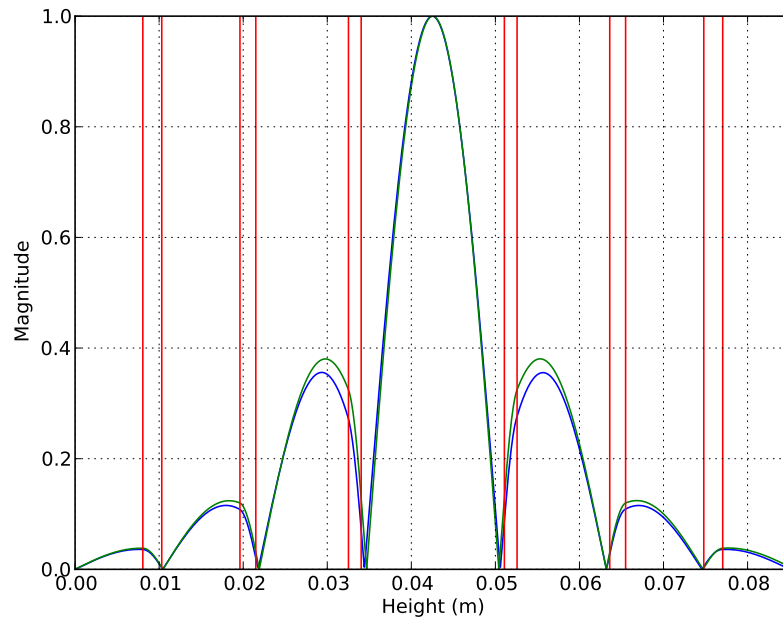


Figure 3.38: Normalised plots of the voltage standing wave distribution predicted by the ABCD model (green trace) and the magnitude of the  $E_\phi$  field along the axis of the aperiodic Bragg resonator (blue trace)

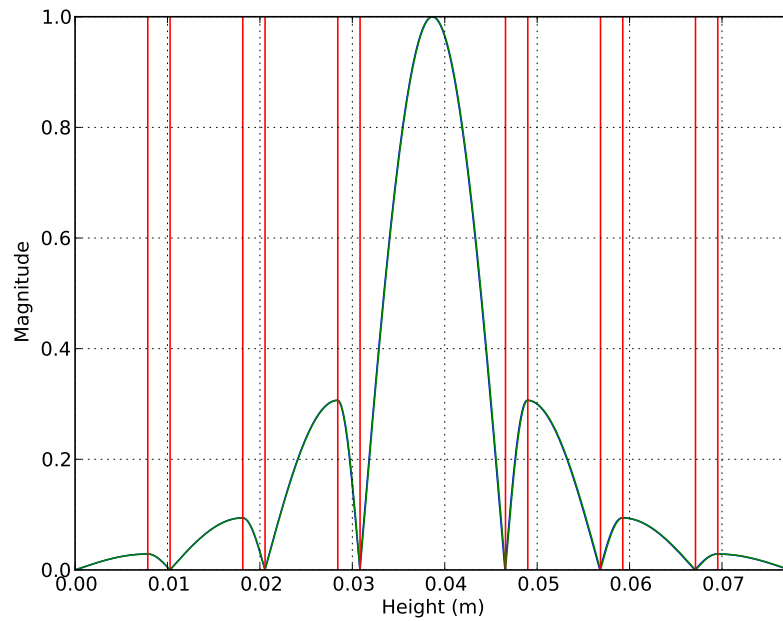


Figure 3.39: Normalised plots of the voltage standing wave distribution predicted by the ABCD model (green trace) and the magnitude of the  $E_\phi$  field along the axis of the periodic Bragg resonator (blue trace)

# Chapter 4

## Cross Correlation Residual Phase Noise Measurement System

### 4.1 Introduction

The purpose of this chapter is to describe the design, implementation and measurement results for an ultra-low noise floor cross correlation residual phase noise measurement system.

Frequency stability can be split into two categories, long-term stability and short-term stability. Long term stability manifests as a gradual drift in the frequency of a waveform. It is commonly caused by temperature variations that modify the operating points of the various components or by ageing of the devices in a system. Short-term stability is a function of the noise signals within the system and represents a phase modulation of the output waveform. In this chapter we are primarily interested in short term stability and the measurement of phase noise.

Phase noise, jitter and therefore the internal residual noise of components and amplifiers set the ultimate performance limits of oscillators and dependent systems. Phase noise can be described as the frequency domain representation of the short term, random fluctuations in the phase of a waveform. Phase noise is important for several reasons. Digital circuits are particularly sensitive to transition jitter which results from phase noise. In an oscillator the phase slope of the resonator (group delay & Q) cause any internal phase fluctuations (within the bandwidth of the resonator) to be transformed into a frequency

fluctuation. These frequency fluctuations then result in increased phase noise at the output of the oscillator [48] [8] [7]. In a communication system this frequency fluctuation can cause increased bit error rates or complete loss of the incoming information. In a frequency synthesiser, the frequency multiplication process also results in the multiplication of phase noise [4] which can limit the maximum attainable frequency. An accurate measurement of phase noise performance of amplifiers, oscillators, synthesisers and other radio frequency components is therefore exceptionally important.

There are a number of existing correlation based noise measurements systems (NMS) in the literature. Rubiola [49] has demonstrated an NMS using a double interferometric technique with a noise floor of  $-192$  dB  $rad^2/Hz$  at microwave frequencies and  $-194$  dB  $rad^2/Hz$  in the VHF band. Walls [50] has demonstrated a conventional cross correlation NMS with a noise floor below  $-190$  dBc/Hz using a 5 MHz carrier.

In this work we show that it is possible to construct a microwave cross correlation residual phase noise measurement system with a noise floor around or below  $-200$  dBc/Hz by using careful design techniques, an HP11848A single channel phase noise interface measurement system and modern signal processing components and techniques. The main reason for using the HP system was that it offers a very low single channel noise floor below  $-180$  dBc/Hz and has been designed and optimized over many years in order to offer the very best performance.

## 4.2 Residual Phase Noise Measurement

Residual noise, also known as modulation or multiplicative noise, can be described as the noise modulated onto a signal when it's processed by a two port network. It consists of both amplitude modulation (AM) and phase modulation (PM) components. In this work we will primarily be dealing with the measurement of the PM component. A full description and definition of phase noise is provided in section 2.4 of chapter 2.

A conventional single channel residual phase noise measurement system is illustrated in figure 4.1. The purpose of the apparatus is to measure and isolate the multiplication noise introduced by the two DUTs.

A low noise sinusoidal signal source is used to provide a reference signal at the input to the measurement system. This signal is then split into two separate paths that provide the drive signals to a phase detector which is

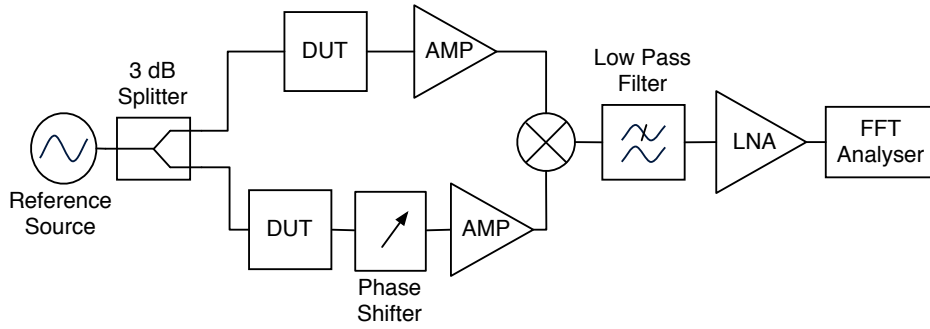


Figure 4.1: A Simplified single channel residual phase noise measurement system.

typically a double balanced mixer. It is assumed that the source phase noise is correlated at the inputs to the phase detector and therefore cancels. A phase shifter is used to adjust the delay in one of the paths such that the signals mix in phase quadrature. This is the point at which a mixer is most sensitive to any phase fluctuations between its input signals and least sensitive to AM noise [51]. Finally, the output of the mixer is low pass filtered to remove any unwanted RF components before being amplified and fed to an FFT analyser. The FFT analyser then plots the spectral density of the noise at the output of the mixer.

The operation of this system can easily be understood by considering the phase detector as an analogue multiplier. We can model a noisy signal using a simple amplitude and phase modulated sinusoid as shown in equation (4.2.1):

$$V(t) = A(1 + \epsilon(t)) \cos(\omega t + \phi(t)) \quad (4.2.1)$$

where,  $\epsilon(t)$  represents the random amplitude variation as a function of time (AM Noise) and  $\phi(t)$  represents the random phase variation (PM Noise). If we now consider two different noisy signals such as:

$$V_0(t) = A_0(1 + \epsilon_0(t)) \cos(\omega_0 t + (\theta_0 + \phi_0(t))) \quad (4.2.2)$$

$$V_1(t) = A_1(1 + \epsilon_1(t)) \cos(\omega_1 t + (\theta_1 + \phi_1(t))) \quad (4.2.3)$$

where  $\theta_0$  and  $\theta_1$  represent a constant average phase shift. The phase noise can be extracted from these signals by multiplying equations (4.2.2) and (4.2.3) to

give equation (4.2.4):

$$V_0(t) \times V_1(t) = \frac{1}{2}A_0A_1(1 + \epsilon_1(t) + \epsilon_0(t) + \epsilon_0(t)\epsilon_1(t)) \times \\ [\cos(\omega_0t + \omega_1t + \theta_0 + \theta_1 + \phi_0(t) + \phi_1(t)) + \\ \cos(\omega_0t - \omega_1t + \theta_0 - \theta_1 + \phi_0(t) - \phi_1(t))] \quad (4.2.4)$$

If we then set  $\omega_1 = \omega_2$ , such that the angular frequency of both signals is identical and then low pass filter

$$V_0(t) \times V_1(t) = \frac{1}{2}A_0A_1(1 + \epsilon_1(t) + \epsilon_0(t) + \epsilon_0(t)\epsilon_1(t)) \times \\ [\cos(\theta_0 - \theta_1 + \phi_0(t) - \phi_1(t))] \quad (4.2.5)$$

If we assume that the signals are mixed in quadrature such that  $\theta_0 = 0^\circ$  and  $\theta_1 = 90^\circ$  then from equation (4.2.5) we can write: (4.2.6):

$$V_0(t) \times V_1(t) = \frac{1}{2}A_0A_1 \times [\sin(\phi_0(t) - \phi_1(t))] \quad (4.2.6)$$

If we then assume that the phase fluctuations are very small such that the small angle approximation  $\sin(\phi) \approx \phi$  is true then from (4.2.6) we can write:

$$V_0(t) \times V_1(t) = K_d \times [(\phi_0(t) - \phi_1(t))] \quad (4.2.7)$$

where  $K_d = \frac{1}{2}A_0A_1$ . If the phase noise terms,  $\phi_0$  and  $\phi_1$ , are un-correlated then:

$$V_0(t) \times V_1(t) = K_d \times [\phi_0(t) + \phi_1(t)] \quad (4.2.8)$$

It can be seen from (4.2.8) that the output of the multiplied and filtered signals is a low frequency voltage representing the phase variation between the two input signals. It is the Fourier components of this signal that are typically used to describe the residual phase noise. The noise floor of a system utilising this single channel measurement technique is highly dependent on and limited by the noise floors of the mixer, filters and low noise amplifier (LNA) [50]. This type of system can have a residual phase noise floor in the region of -180 dBc/Hz at high offset frequencies [52].

### 4.3 The Cross Correlation Technique

The cross correlation technique can be used to suppress the mixer, filter and baseband LNA noise from the measurement results by using two channels [50]. Using this method the uncorrelated noise in each channel can be suppressed by a factor of  $\sqrt{N}$ , where  $N$  is the number of cross correlations. In this type of system two independent channels are used and their outputs are fed to a cross spectrum analyser. Figure 4.2 shows the simplified diagram of a cross correlation residual phase noise measurement system.

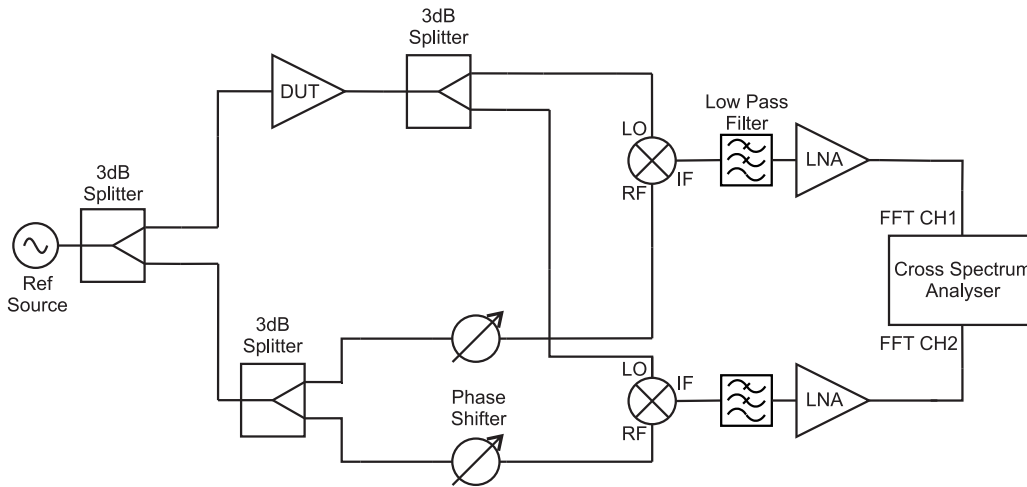


Figure 4.2: Simplified cross correlation residual phase noise measurement system.

It can be seen that the reference signal is split into two paths, the first passes through the device under test (DUT). The signal at the output of the DUT is then equally split again where it provides the LO inputs to a pair of mixers. The second path from the reference source also passes through a 3 dB splitter whose outputs are used to provide the additional quadrature signals required to drive the mixers. This arrangement ensures that the noise added by the DUT is correlated in both channels while the noise generated by the mixers, filters and LNA remains un-correlated.

As described by Rubiola[53], the noise present at the output of each mixer can be modelled using the two noisy signals shown in equations (4.3.1) and (4.3.2).

$$x(t) = a(t) + c(t) \xleftrightarrow{FFT} X(f) = A(f) + C(f) \quad (4.3.1)$$

$$y(t) = b(t) + c(t) \xleftrightarrow{FFT} Y(f) = B(f) + C(f) \quad (4.3.2)$$

where  $a(t)$  and  $b(t)$  represent the uncorrelated instrument noise present in each channel and  $c(t)$  represents the correlated DUT noise. If we take the cross spectrum of these two signals and average over  $N$  samples then we can write:

$$\overline{S_{XY}} = \frac{1}{N} \sum_{n=1}^{n=N} [X_n \times Y_n^*] \quad (4.3.3)$$

where  $n$  represents the sample index and  $*$  implies the conjugate. If we then substitute equations (4.3.1) and (4.3.2) into (4.3.3) we can write:

$$\overline{S_{XY}} = \frac{1}{N} \sum_{n=1}^{n=N} [(A_n + C_n) \times (B_n + C_n)^*] \quad (4.3.4)$$

Finally, after multiplying out the brackets, we can write (4.3.5)

$$\overline{S_{XY}} = \frac{1}{N} \sum_{n=1}^{n=N} [(A_n B_n^*) + (A_n C_n^*) + (C_n B_n^*) + (C_n C_n^*)] \quad (4.3.5)$$

If we assume that there is no correlation between the noisy signals  $a(t)$ ,  $b(t)$  or  $c(t)$  then as the number of averages increases, the uncorrelated terms in the cross spectrum -  $AB$ ,  $AC$  and  $CB$  will all approach zero. The only remaining term,  $CC$ , represents the power spectral density of the correlated DUT noise.

### 4.3.1 Data Windowing

The correlation sum described in (4.3.3) consists of  $N$  uniformly spaced frequency domain samples. These frequency domain samples are typically generated by using an implementation of the discrete Fourier transform (DFT). The mathematics of the DFT and the discrete nature of the time to frequency domain conversion dictate that the DFT will only produce an exact result when the input data contains energy at the exact centre of each frequency bin. If the input signal has a frequency component at some frequency between bins then some of it's energy will leak into adjacent bins [54]. This phenomenon causes several problems, it may degrade our ability to detect small tones adjacent to nearby strong tones and it will degrade the amplitude accuracy of our wanted signal. We can compensate for this problem by multiplying the time domain data by a 'window' function.

Three window functions are of particular interest for use during phase noise measurements and these are the Flat-Top, Hann and Rectangular window

functions. The Flat-Top window functions is shown in equation (4.3.6)

$$w(n) = a_0 - a_1 \cos\left(\frac{2\pi n}{N}\right) + a_2 \cos\left(\frac{4\pi n}{N}\right) - a_3 \cos\left(\frac{6\pi n}{N}\right) + a_4 \cos\left(\frac{8\pi n}{N}\right) \quad (4.3.6)$$

where  $N$  is the total number of samples,  $n$  is the sample index and the range of  $n$  is given by  $0 \leq n \leq N$ . The coefficients  $a_0$  to  $a_4$  are shown in table 4.1. It should be noted that these coefficients have been scaled in order to incorporate the coherent power gain of the window.

Coefficient	Value
a0	0.21557895
a1	0.41663158
a2	0.277263158
a3	0.083578947
a4	0.006947368

Table 4.1: The coefficients,  $a_0$  to  $a_4$  for the Flat-Top window function specified in equation (4.3.6).

A frequency domain plot of the flat-top window function is shown in figure 4.3. This window is characterised by a flat and broad main lobe with a side-lobe amplitude of less than -70 dB. These characteristics ensure that the window provides excellent amplitude accuracy as well as dramatically reducing any leakage. The flat-top window is therefore a good choice for measuring the amplitude of noise spurs or calibration tones. Unfortunately this window is a poor choice for noise analysis because its wide main lobe results in an equivalent noise bandwidth of  $3.43\Delta f$  as well as reduced selectivity.

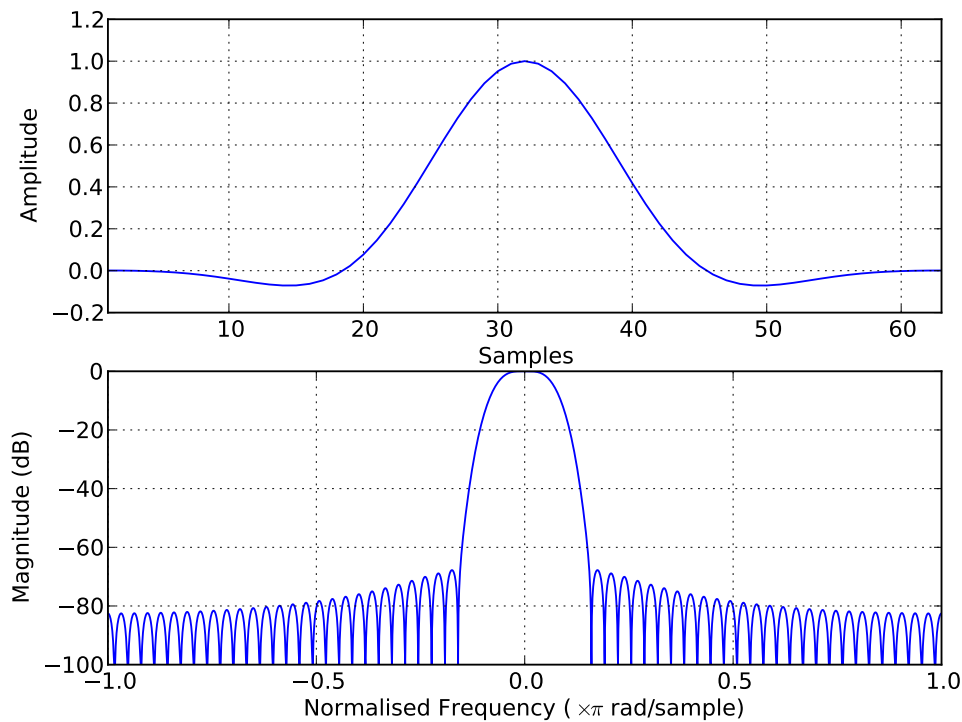


Figure 4.3: Time domain (top) and Frequency domain (bottom) plots for a 64 point flat-top window as defined in (4.3.6)

The process of measuring our input signal for a finite time is equivalent to multiplying the time domain data by a rectangular window. We can define the rectangular window function using equation (4.3.7) and a frequency domain response is shown in figure 4.4.

$$w_n = 1.0 \quad (4.3.7)$$

This window has a narrow main lobe with high side lobes (-13dB). The high side lobes result in a large level of spectral leakage and therefore make the window unsuitable for accurately measuring the amplitude of any large single frequency signals such as noise-spurs. However, the narrow main lobe provides excellent frequency resolution and a small equivalent noise bandwidth which makes this window most suitable for making broadband noise measurements.

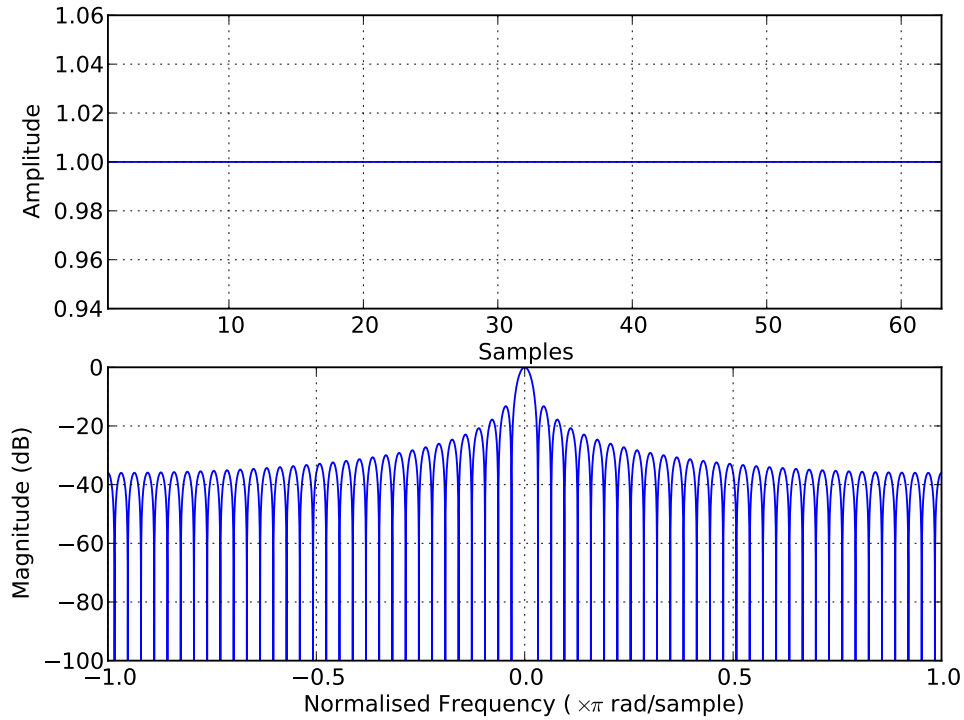


Figure 4.4: Time domain (top) and Frequency domain (bottom) plots for a 64 point rectangular window as defined in (4.3.7)

The Hann window function is defined in equation (4.3.8) and a frequency domain response is shown in figure 4.5.

$$w_n = 0.5 \left( 1 - \cos 2\pi \frac{n}{N} \right) \quad (4.3.8)$$

The Hann window provides a compromise between the characteristics of the Flat-Top and rectangular windows. It has a narrow main lobe and a maximum side lobe level of -32 dB. These side lobes fall off at a rate of -60 dB/decade. When compared with the rectangular window the Hann function provides greatly reduced leakage and improved amplitude accuracy at the expense of a slightly reduced frequency accuracy and an increased equivalent noise bandwidth of  $1.5\Delta f$ .

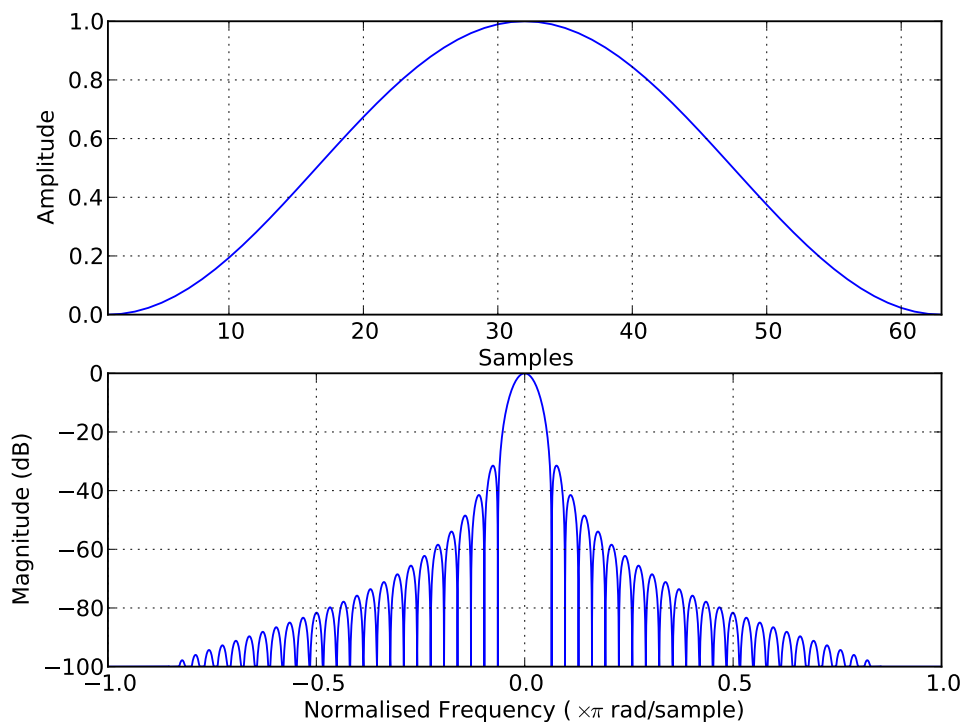


Figure 4.5: Time domain (top) and Frequency domain (bottom) plots for a 64 point Hann window as defined in (4.3.8)

## 4.4 Measurement Apparatus

A block diagram of the complete measurement system, including calibration components, is shown in 4.6. The phase detector, LNA and filtering are provided by two HP 11848A phase noise test sets, shown enclosed inside the red dashed rectangles. These units exhibit a low single channel noise floor of below  $-180$  dBc/Hz at carrier offsets greater than 10kHz [52]. They are also fully computer controllable using Visual Basic software developed at the UK National Physical Laboratory (NPL) by David Adamson. A dual channel high speed data capture card with a 16bit resolution and maximum sampling rate of 125 MSamples/sec is used to capture the noisy signal at the output of the anti-aliasing filter. A software based cross spectrum analyser has also been developed using the Java programming language. This fully multi-threaded software allows spectrum auto-correlation and cross-correlation as well as the application of multiple time domain windows to the sampled data. Additional high order LC anti-aliasing filters were placed at the input to the A to D converters.

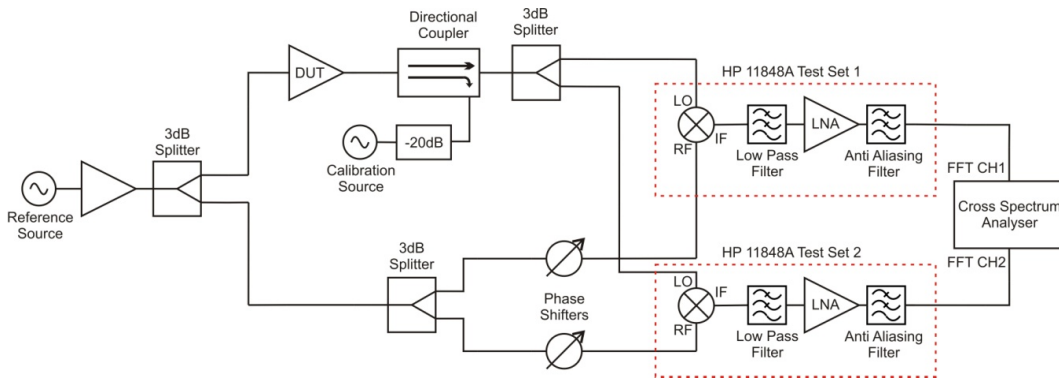


Figure 4.6: Cross correlation residual phase noise measurement system including calibration components.

The reference source is provided by a battery powered ultra low phase noise dielectric resonator oscillator (DRO) developed at York. This oscillator exhibits PM and AM noise levels of less than  $-173\text{dBc}/\text{Hz}$  at carrier offset greater than  $10\text{kHz}$  [55]. Its low level of AM noise is particularly beneficial when making sensitive phase noise measurements. This is because a typical saturated double balance microwave usually only offers around  $20\text{ dB}$  to  $30\text{ dB}$  of AM noise suppression [52]. Once this has been exhausted the source AM noise will directly add to the residual phase noise and corrupt the measurement results. A power amplifier with a gain of  $20\text{ dB}$  was connected to the output of the reference oscillator to increase the signal level to a value large enough to saturate the phase detectors. Saturation of the phase detectors is required in order to ensure that any AM noise present at the input to the phase detectors is suppressed. In order to reduce the effect of any external noise sources on the measurement results double shielded, microwave cables are used to interconnect the various components. A photograph of the measurement apparatus is shown in figure 4.7

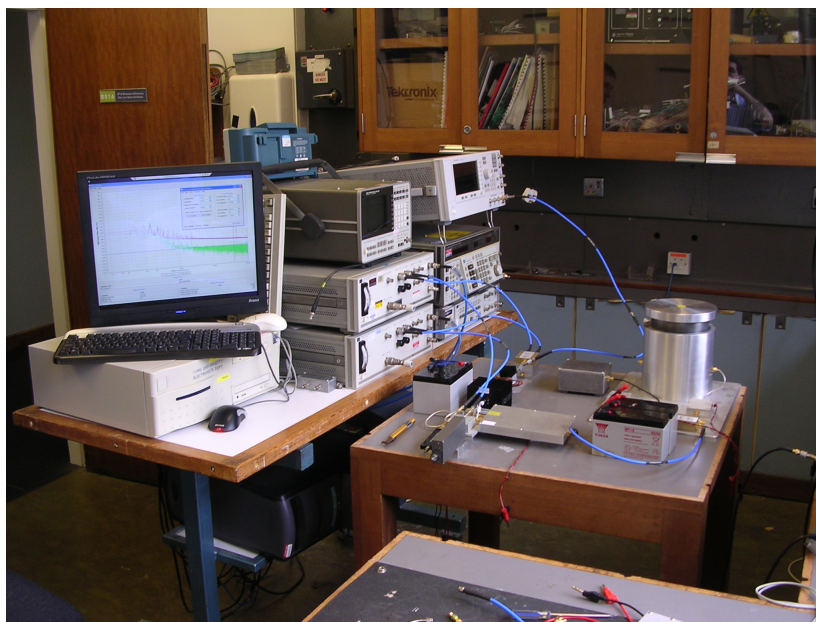


Figure 4.7: A photograph of cross correlation residual phase noise measurement system.

#### 4.4.1 System Calibration

Calibration is achieved by injecting a tone into the measurements system via the directional coupler shown in 4.6. This tone modulates the carrier signal present at the LO ports of both phase detectors and will therefore appear as a single side-band spur at the inputs to the cross spectrum analyser. Injecting a signal at this point ensures that non-linearities in both mixers are accounted for and that the calibration conditions match the measurement conditions as closely as possible. It's important to note that the accuracy of the calibration and resulting phase noise measurements is, in part, limited by the accuracy achieved during the measurement of the amplitude and frequency of the calibration spur. As described in 4.3.1 we must window the measured signal in order to reduce the spectral leakage that will occur as a result of transformation into the frequency domain. During the calibration the amplitude accuracy of the spur measurement is the most important parameter and for this reason a flat-top window was used. When the calibration spur measurement has been completed the tone is removed and the coupled port of the directional coupler is terminated with a  $50\Omega$  load. The measured noise can then be converted to single sideband phase noise,  $L(f)$ , using (4.4.1).

$$L(f) = S_{\phi} + K_1 + K_2 - 6 \quad (4.4.1)$$

where  $S_\phi$  is the double side band phase noise spectral density,  $K_1$  is the carrier to sideband spur ratio and  $K_2$  is the amplitude of the calibration spur - all parameters are in decibels. The subtraction of an additional 6dB is necessary in order to account for the fact that we are measuring double side band phase noise at the output of the mixers. The primary advantage of calibrating the instrument in this way is that the calibration is performed under the actual measurement conditions with the DUT in place. It should also be noted that ideally a calibration spur should be injected at every measurement frequency of interest; however, the frequency response of the HP11848A units is sufficiently flat that this is not necessary.

In order to check the validity of this calibration technique a second independent calibration method was used. The DUT was replaced with the series connection of a 44 dB attenuator and a 44 dB amplifier as shown in 4.8.

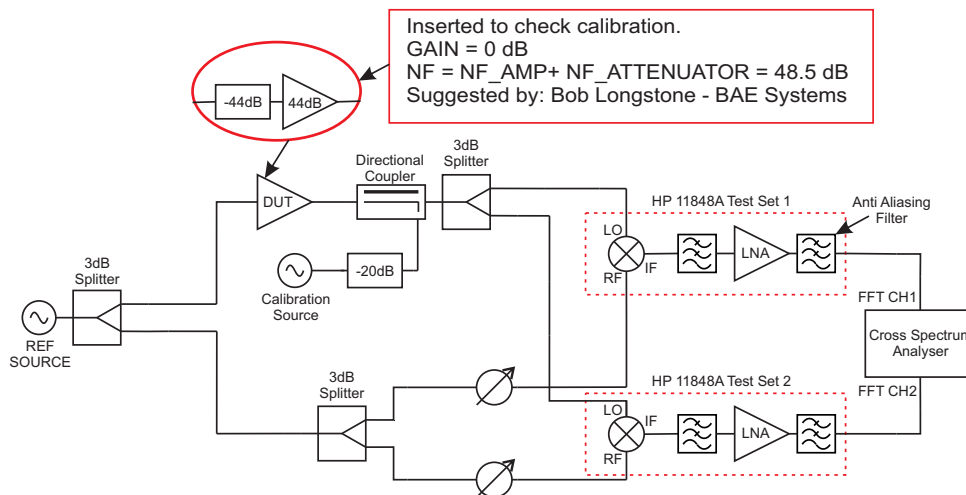


Figure 4.8: Cross correlation phase noise measurement system showing the additional components required to artificially increase the system noise floor. This arrangement was used to check the validity of the calibration technique.

This arrangement artificially increases the system noise floor to a value that can be calculated using (4.4.2):

$$L(f) = -177 + N_A - P_i \quad (4.4.2)$$

where  $N_A$  is the noise figure of the combined amplifier and attenuator and  $P_i$  is the power available at the input to the attenuator. If we substitute in the combined noise figure of 48.5 dB and an input power of 20 dBm then the theoretical phase noise floor can be calculated to be -148.5 dBc/Hz at offsets above the flicker noise corner. The measured noise floor was -148.4 dBc/Hz

which is in good agreement with the theory.

## 4.5 System Noise Floor Measurements

The system noise floor is measured by removing the DUT from the equipment setup and replacing it with a straight through connection as shown in figure 4.9:

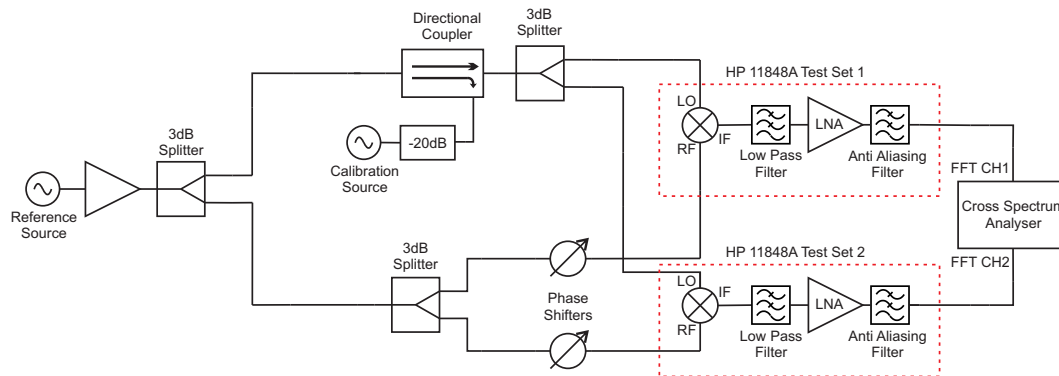


Figure 4.9: Equipment configuration used to measure the noise floor of measurement system

The phase shifters were adjusted so that DC level at the output of each mixer was at a minimum. In order that the source phase noise did not de-correlate at large offset frequencies the group delay of each channel was measured to ensure that the phase shift between the mixer input ports was only  $90^\circ$  and not a higher multiple. The measurement was performed at a frequency of 1.25 GHz with mixer LO and RF port input powers of 16.1 dBm and 16.9 dBm respectively. The use of high power levels ensures that the mixers are truly saturated and minimises the signal channel noise floor of each HP 11848A unit. The signal processing was performed at a sampling rate of 2 MSamples/Sec with a data frame length of 262,144 points. This equated to a resolution bandwidth of 7.63 Hz. In order to minimise the FFT noise bandwidth no additional data windowing was performed. That is to say, that the data was effectively multiplied by a uniform window resulting in a noise bandwidth identical to the resolution bandwidth.

After the calibration had been performed the residual noise floor was measured for increasing numbers of cross correlations. Table 4.2 details residual phase noise floor and acquisition time for each of these measurements. The final measurement of 100,000 cross correlations has an increased resolution bandwidth because the number of data points acquired in each frame was reduced in order to shorten the measurement time.

Correlations	Noise Floor @ 20kHz Offset (dBc/Hz)	Measurement Time (Seconds)	Resolution Bandwidth (Hz)
100	< -185dBc/Hz	73	7.63Hz
1000	< -190dBc/Hz	730	7.63Hz
10,000	< -195dBc/Hz	7300	7.63Hz
100,000	< -200dBc/Hz	3620	122.07Hz

Table 4.2: Residual phase noise floor of the cross correlation measurement system at a 20kHz offset from a carrier frequency of 1.25 GHz.

Figures 4.10, 4.11 and 4.12 on pages 97, 98 and 99 show plots of residual phase noise floor for 1000, 10,000 and 100,000 cross correlations respectively. The blue and red (upper) traces are the noise floors for each independent channel and the green (lower) trace is the dual channel cross correlated noise floor. It should be noted that due to the large variance of the measured noise the top of noise line was used to provide a conservative estimate for the noise floor. This demonstrates a noise floor of -200 dBc/Hz for offsets greater than 20 kHz. This ties in accurately with the overall noise floor predicted for the system which can be easily calculated from the microwave power level at the input to the system which was +23 dBm. The noise floor would then be predicted to be +23-177 i.e. -200 dBc/Hz. If we compare these three figures, the reduction in noise floor is clearly visible as the number of correlations increase. The phase noise floor is reducing by approximately 5 dB for every factor of 10 increases in the number of cross correlations and this is in good agreement with the theory. Unfortunately the close to carrier noise, at frequency offsets below 1 kHz, does not show the same level of suppression. This is thought to be a result of the high levels of spurs that are present in the 10 Hz to 1 kHz region. These spurs are most probably due to noise introduced by the ancillary equipment inside the HP3048 units as well as the other external noise sources present in the laboratory environment.

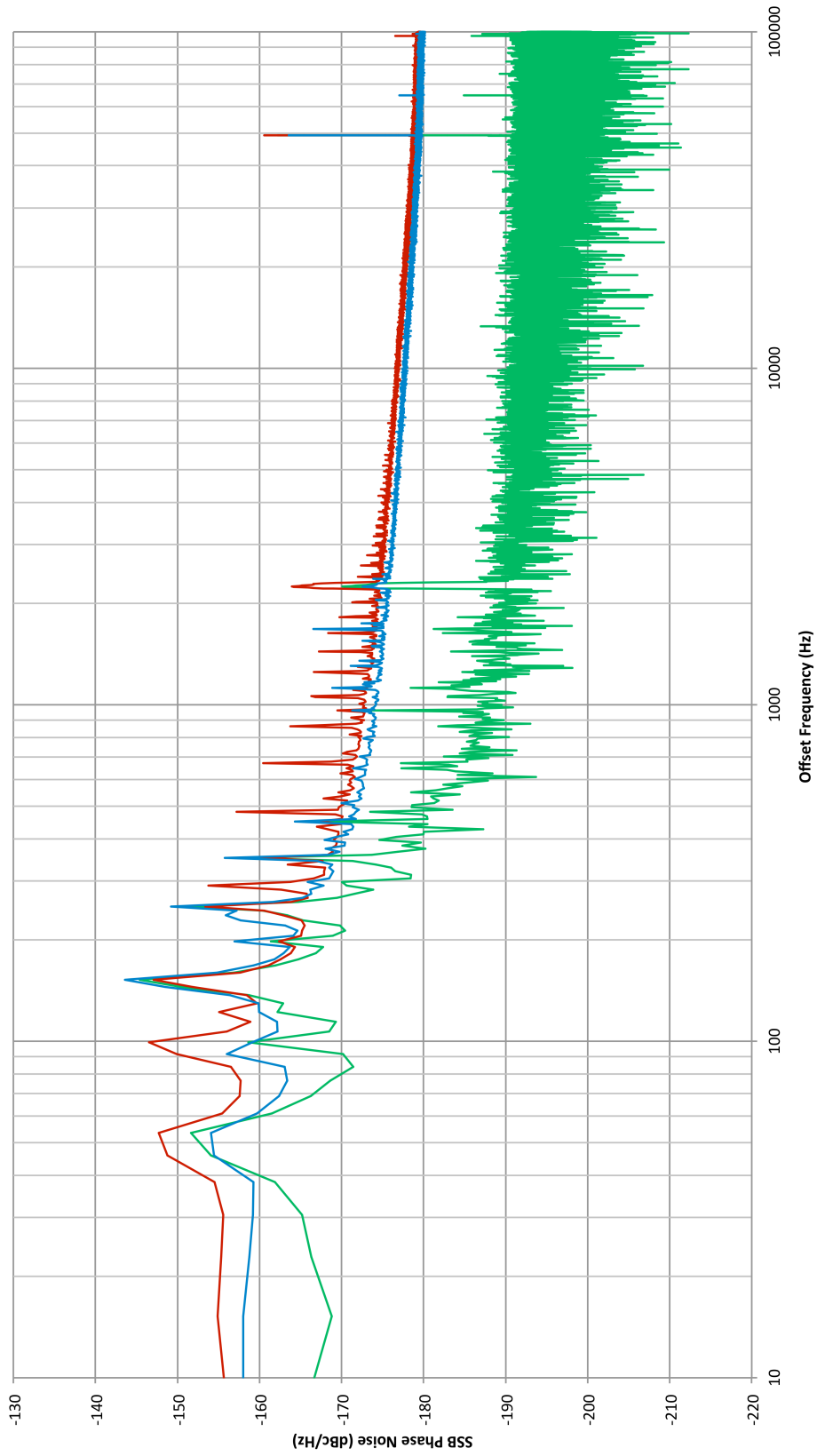


Figure 4.10: Residual phase noise floor of the cross correlation measurement system after 1000 cross correlations. This measurement was made with a resolution bandwidth of 7.63Hz

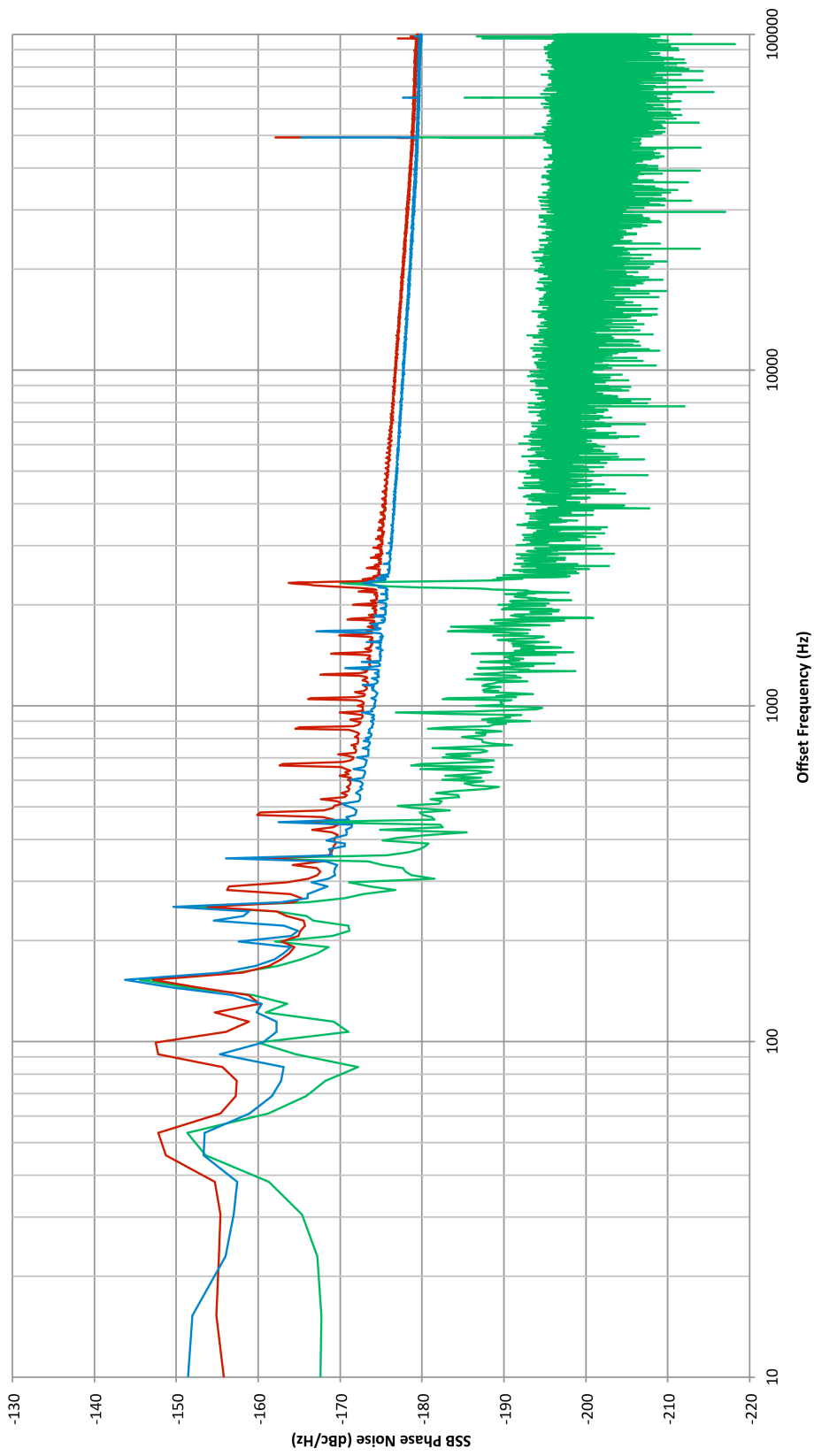


Figure 4.1.1: Residual phase noise floor of the cross correlation measurement system after 10000 cross correlations. This measurement was made with a resolution bandwidth of 7.63Hz

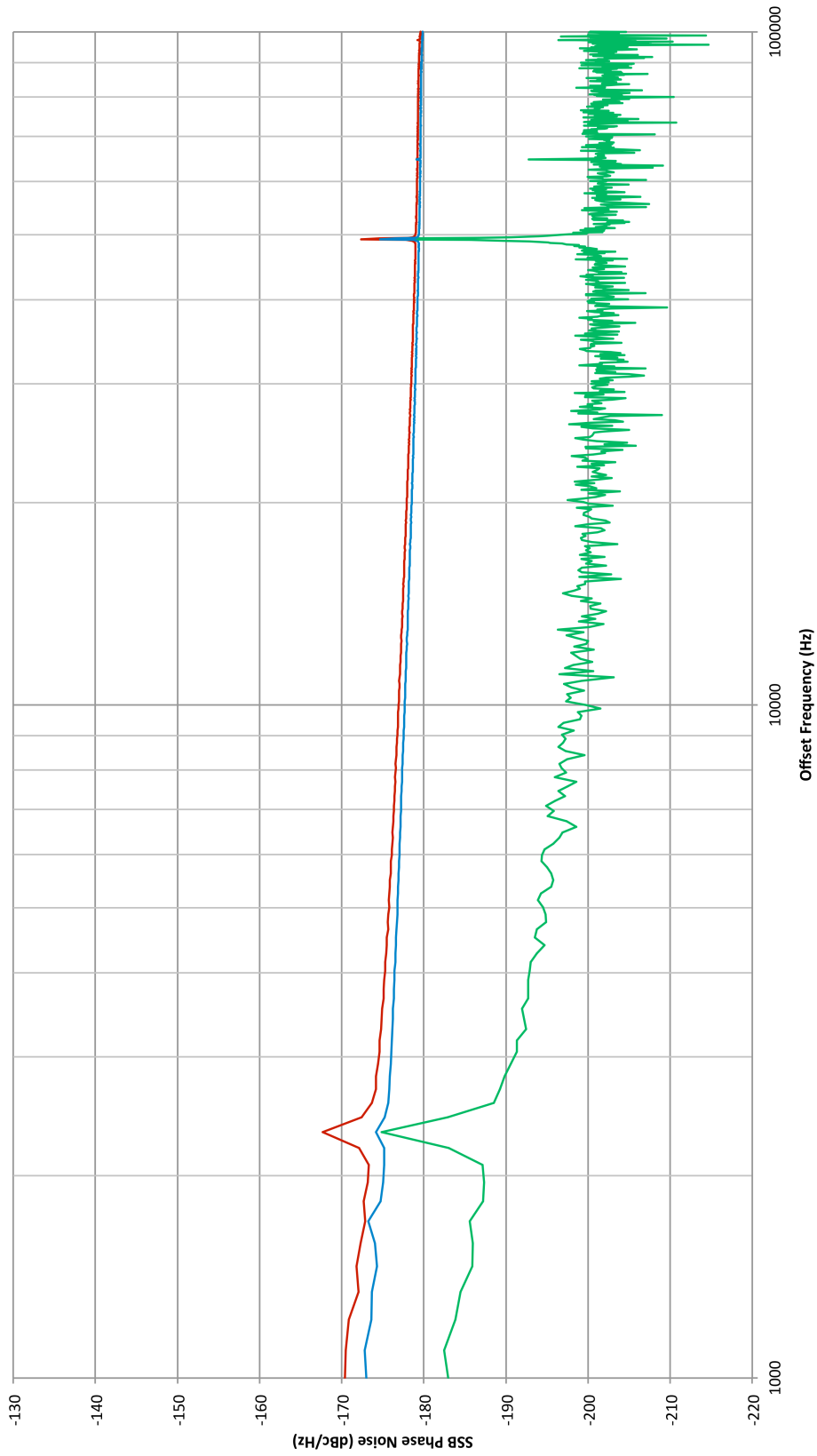


Figure 4.12: Residual phase noise floor of the cross correlation measurement system after 100,000 cross correlations. This measurement was made with an increased resolution bandwidth of 122.07 Hz in order to reduce the measurement time.

## 4.6 Low Noise Amplifier Measurements

In order to show the utility of the system for measuring the performance of devices that exhibit extremely low levels of phase noise a measurement of a 1.25 GHz medium power silicon amplifier has been performed. This amplifier was developed at York and exhibits a noise figure of 8 dB, it has previously been shown to have a far from carrier phase noise floor of at least -183 dBc/Hz. The amplifier was powered using batteries in order to reduce the potential for additional interference. A power level of 17.2 dBm was provided to its input and the theoretical far from carrier residual phase noise floor was calculated using (4.4.2) as -186.2 dBc/Hz.

Figures 4.13, 4.14 and 4.15 on pages 101, 102 and 103 show plots of the amplifiers residual phase noise for 100, 1000 and 5000 cross correlations respectively. With reference to figure 4.13 it can be seen that after 100 correlations the measured noise still has a large variance. This is because the uncorrelated instrument noise is present in the measurement data. However, as the number of correlations increases it can clearly be seen that the measured noise is converging to an absolute value. At offsets above 10 kHz the residual phase noise is approximately -185 dBc/Hz, this is good agreement with the theoretical value of -186.2 dBc/Hz.

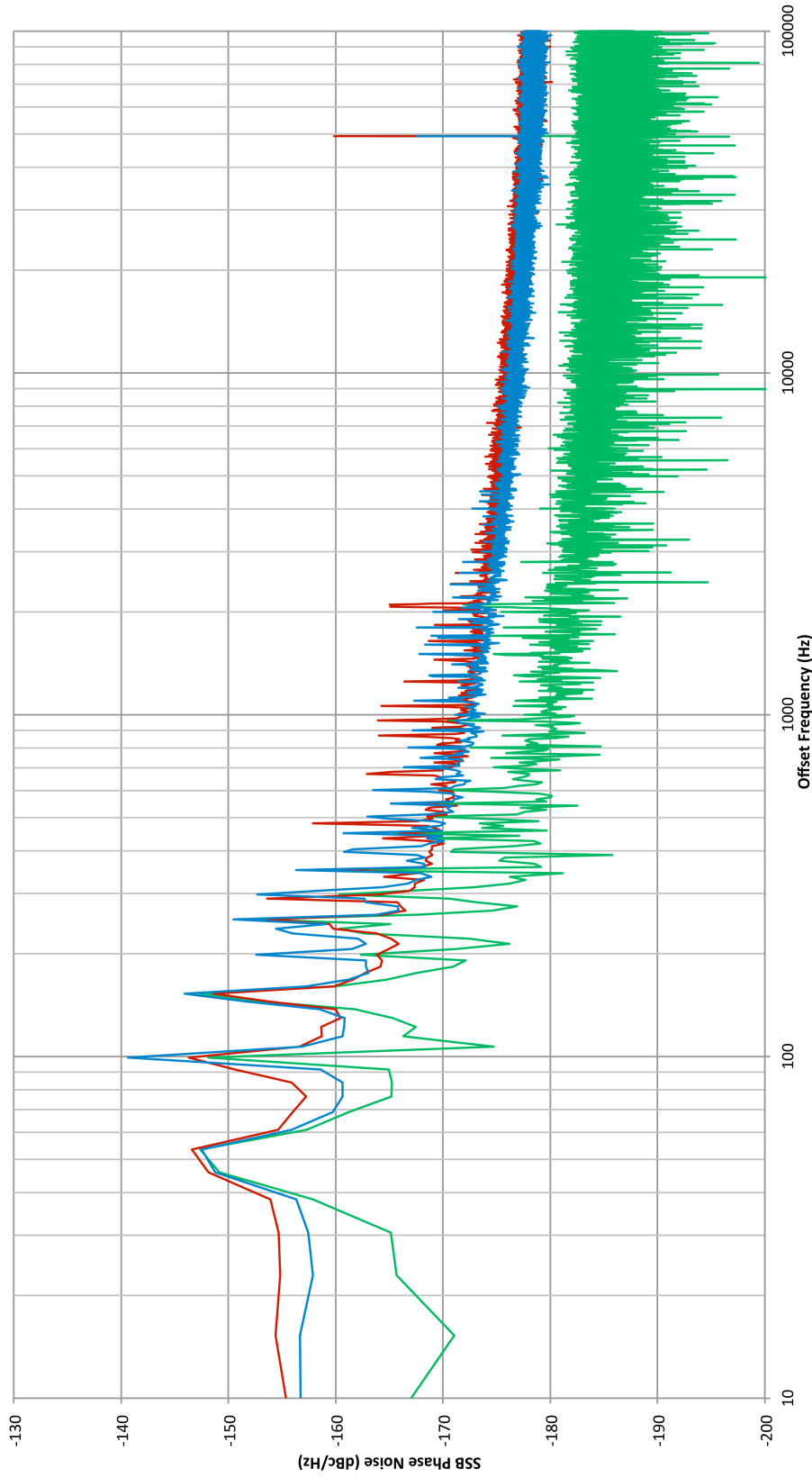


Figure 4.13: Residual phase noise floor of the 1.25 GHz medium power silicon amplifier after 100 cross correlations. The blue and red (upper) traces are the noise floors for each independent channel and the green (lower) trace is the dual channel cross correlated noise floor

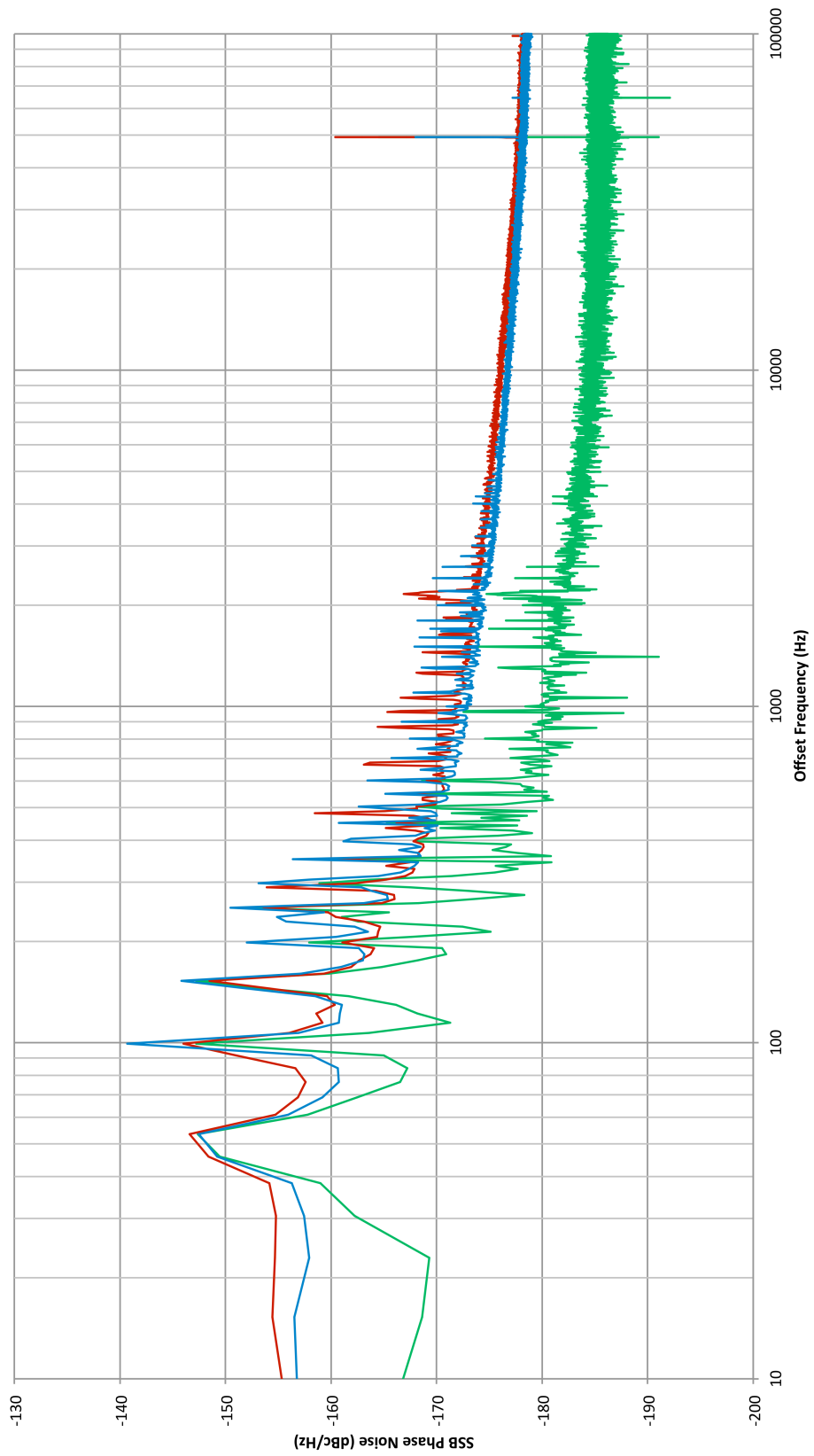


Figure 4.14: Residual phase noise floor of the 1.25 GHz medium power silicon amplifier after 1000 cross correlations. The blue and red (upper) traces are the noise floors for each independent channel and the green (lower) trace is the dual channel cross correlated noise floor

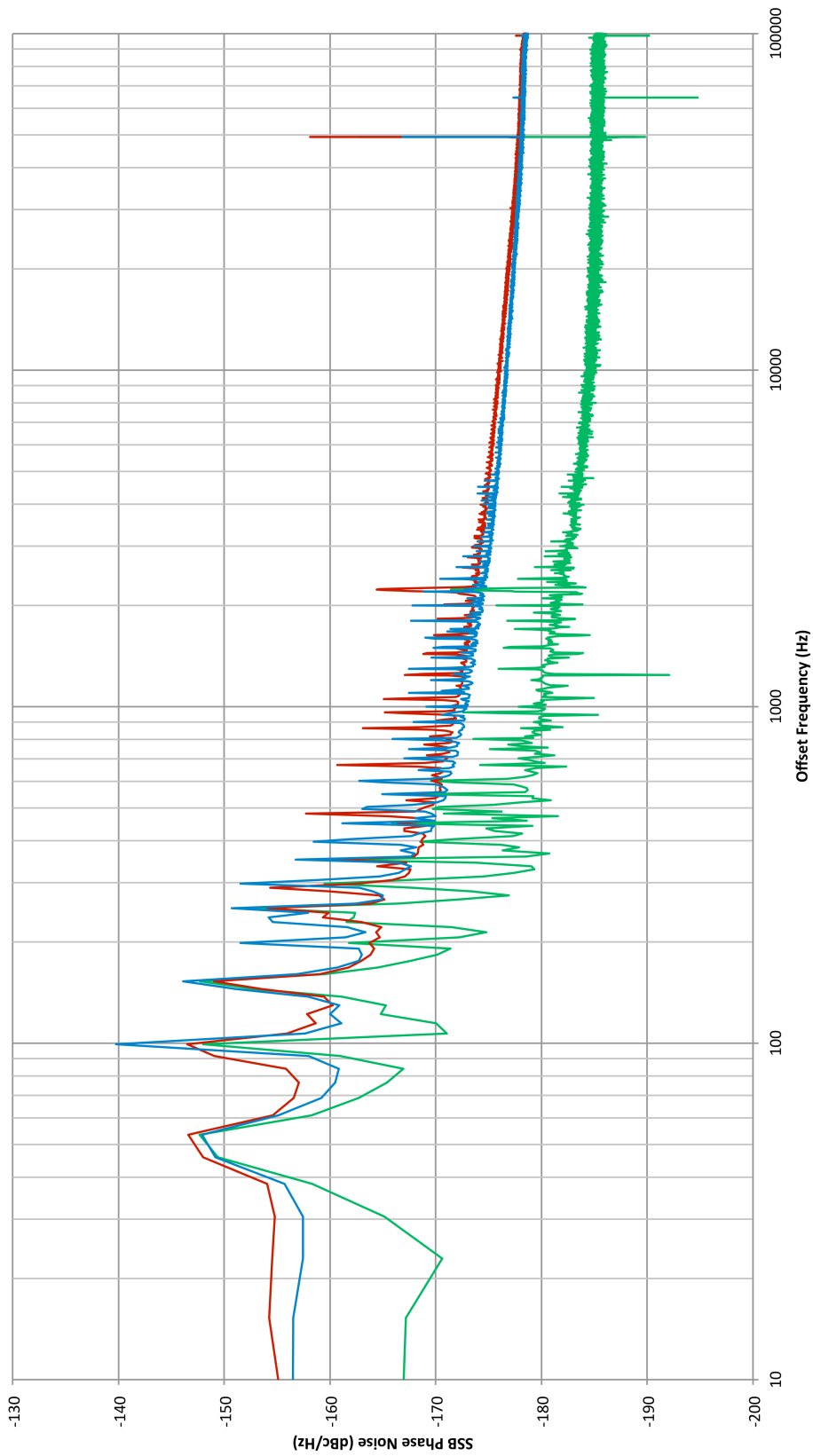


Figure 4.15: Residual phase noise floor of the 1.25 GHz medium power silicon amplifier after 5000 cross correlations. The blue and red (upper) traces are the noise floors for each independent channel and the green (lower) trace is the dual channel cross correlated noise floor

## 4.7 Conclusions

A cross correlation residual phase noise measurement system has been demonstrated with a noise floor in excess of  $-200$  dBc/Hz for 100,000 correlations. This is an improvement of 20 dB when compared with the same system operating with a single channel and is typically 10dB better than current commercial systems. This system was then used to measure a low noise medium power L-Band amplifier at 1.25GH. This demonstrated a residual noise figure of  $-186$  dBc/Hz at 10 kHz and  $-180$  dBc/Hz at 1 kHz. No additional AM suppression was required to achieve these results. It is expected that the noise floor can be further improved by increasing the power at the input to the system. Note that the power at the mixers is limited to  $+23$  dBm which would allow an increase of 7 dB for the noise floor measurement. Further increases can be incorporated with this system just by using attenuators in front of the mixers but of course this then requires a larger number of cross correlations and hence more processing time.

# Chapter 5

## Residual Phase Noise Measurements of Microwave Components

The phase noise performance of a feedback oscillator is limited by the residual noise performance of the sustaining amplifier and other loop components, as well as the feedback loop power and the resonator quality factor. It is therefore critical to minimise the residual phase noise produced by the components inside the oscillator loop. In this chapter we assess the residual phase noise performance of several microwave components in order to establish their potential utility in a low phase noise oscillator.

In the first part of the chapter the designs for a Gallium Nitride (GaN) power amplifier are presented along with the measurements of its noise figure and residual phase noise performance. In the second part of the chapter the designs and performance of an emitter coupled logic (ECL) static digital frequency divider are presented.

### 5.1 Gallium Nitride Amplifier

Amplifiers constructed using Silicon or Silicon Germanium Bipolar Junction transistors typically exhibit low noise figures and low flicker noise levels. However, at frequencies above a few Gigahertz the power available from these devices is low. GaAs Field effect transistors can provide much higher powers however they exhibit poor residual noise characteristics. Oscillators incorporating amplifiers constructed using GaAs based amplifiers usually exhibit

poor phase noise performance due to the increased transposed flicker noise [56]. They are typically 20 to 30 dB worse than their silicon equivalents at offsets of around 10 kHz [56]. After extensive discussions with Cree in the USA it was suggested that we may be able push the operating frequency of one of their commercial 10 Watt GaN devices which normally operated between 2 and 6 GHz up to 10 GHz and that their device may be able to achieve a low noise figure. The Flicker noise performance of the device was unknown.

### 5.1.1 Amplifier Design

The first stage of the design was to ascertain the S-Parameters for the device. A non-linear SPICE model containing data for both the die and package was provided by the manufacturer. The model was placed in the circuit configuration shown in figure 5.1 and a commercial Spice simulator was used to measure the S-Parameters.

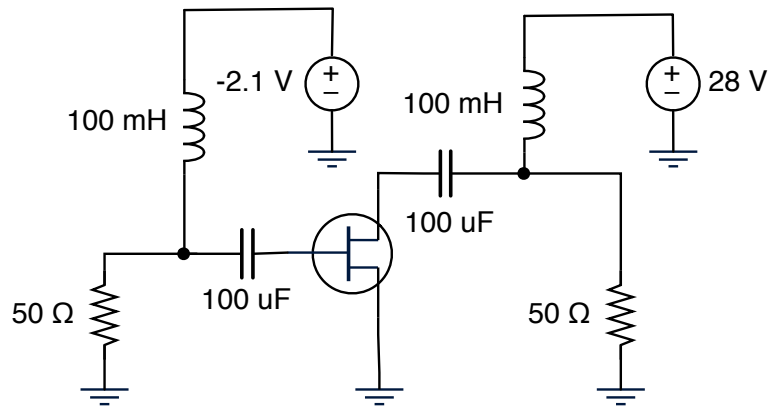


Figure 5.1: Bias circuit used to measure the S-Parameters of the CGH40010 GaN transistor. The bias conditions were  $V_{DS} = 28 V$ ,  $I_D = 200 mA$  and  $V_{GS} = -2.1 V$

The device was biased with a drain to source voltage ( $V_{DS}$ ) of 28V and a drain current ( $I_D$ ) of 200 mA, this required a gate to source voltage ( $V_{GS}$ ) of -2.1 V. Large inductors of 100 mH were used to provide the RF chokes required to inject the bias. The S-Parameters of the device at 10 GHz are shown in table 5.1:

Parameter	Magnitude	Angle (Degrees)
$S_{11}$	0.916806	3.012181
$S_{21}$	1.120886	-133.312871
$S_{12}$	0.038345	-80.574106
$S_{22}$	0.551785	44.977872

Table 5.1: S-Parameters for the CGH40010 GaN transistor at 10 GHz with  $V_{DS} = 28 V$  and  $I_D = 200 mA$

The amplifier was designed for maximum gain at an operating frequency of 10 GHz. First, the stability of the transistor was checked using the  $K - \Delta$  test. This states that a transistor is unconditionally stable if Rollet's condition,  $K$ , is greater than unity and the auxiliary condition,  $|\Delta|$ , is less than unity. As  $K > 1$  and  $|\Delta| < 1$  the transistor is unconditionally stable at 10 GHz.

$$|\Delta| = |S_{11}S_{22} - S_{12}S_{21}| = 0.514 \quad (5.1.1)$$

$$K = \frac{1 - |S_{11}|^2 - |S_{22}|^2 + |\Delta|^2}{2|S_{12}S_{21}|} = 1.383 \quad (5.1.2)$$

In order to maximise the gain of the amplifier the matching sections are designed for a conjugate match, such that the source impedance is transformed to a value equal to the conjugate of the input impedance,  $\Gamma_S = \Gamma_{IN}^*$  and the load impedance is transformed to a value equal to the conjugate of the output impedance,  $\Gamma_L = \Gamma_{OUT}^*$ . As described by Pozar [30] the values of the source and load impedances for a simultaneous conjugate match, assuming a bilateral device, can be calculated using equations (5.1.3) and (5.1.4):

$$\Gamma_S = \frac{B_1 \pm \sqrt{B_1^2 - 4|C_1|^2}}{2C_1} = 0.9374 \angle -5.132^\circ \quad (5.1.3)$$

$$\Gamma_L = \frac{B_2 \pm \sqrt{B_2^2 - 4|C_2|^2}}{2C_2} = 0.6463 \angle -70.305^\circ \quad (5.1.4)$$

where  $B_1$ ,  $B_2$ ,  $C_1$  and  $C_2$  are given by equations (5.1.5), (5.1.6), (5.1.7) and (5.1.8):

$$B_1 = 1 + |S_{11}|^2 - |S_{22}|^2 - |\Delta|^2 \quad (5.1.5)$$

$$B_2 = 1 + |S_{22}|^2 - |S_{11}|^2 - |\Delta|^2 \quad (5.1.6)$$

$$C_1 = S_{11} - \Delta S_{22}^* \quad (5.1.7)$$

$$C_2 = S_{22} - \Delta S_{11}^* \quad (5.1.8)$$

A Smith chart was used to perform the impedance transformation and the resulting single-stub matching network is shown in figure 5.2:

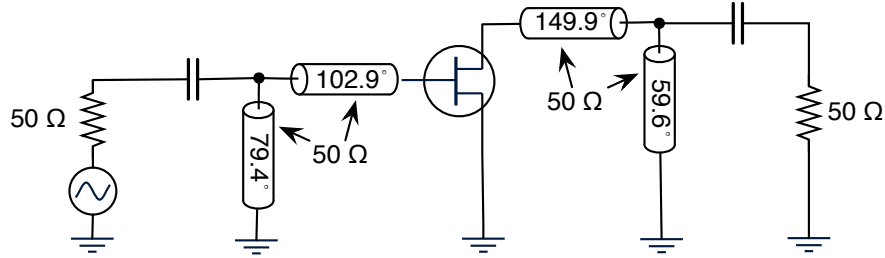


Figure 5.2: Single stub matching network for the CGH40010 GaN transistor.

The complete RF circuit for the CGH40010 power amplifier is shown in figure 5.3. A Bias-T network incorporating a radial stub was used to inject the bias voltages and currents. The transmission line lengths shown are for 50  $\Omega$  micro-strip line. The lengths of the matching sections were tuned using a SPICE simulator in order to account for the small impedance mismatches introduced by the biasing components. A 40  $\Omega$  resistor was also placed in series with the base to improve the low frequency stability, this resistor was capacitively bi-passed at high frequencies.

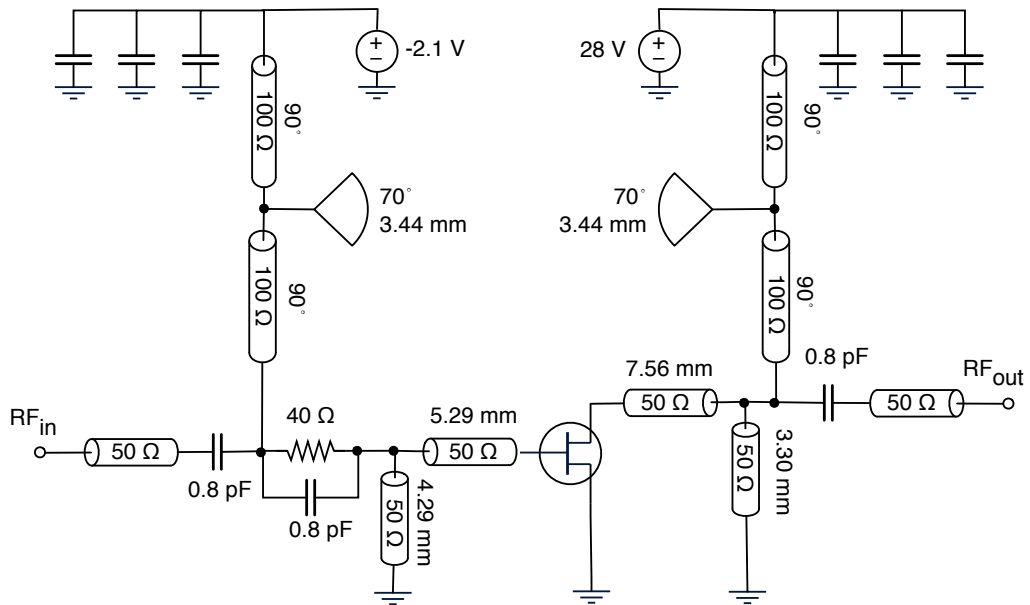


Figure 5.3: CGH40010 power amplifier circuit including biasing components.

A photograph of the amplifier is shown in figure 5.4. Note the amplifier is a 3 part jig (I/P matching, Device and O/P matching). This enables changing device as well as looking backwards into the input matching network to work out the input impedance. This also enables checking of the load network input impedance.

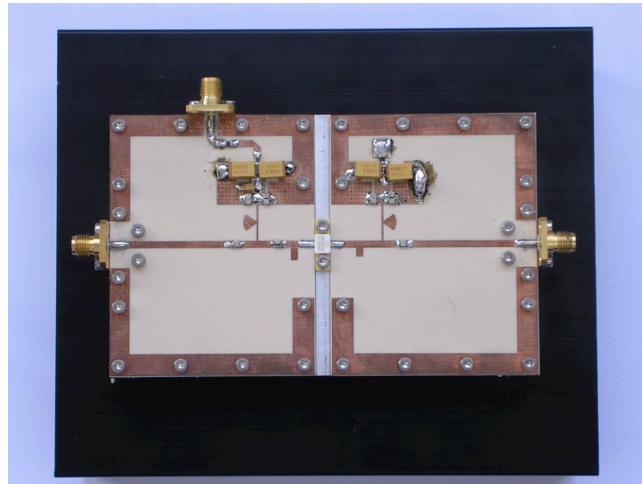


Figure 5.4: Photograph of the CGH40010 power amplifier.

A plot of this simulated S-Parameters is shown in figure 5.5 where a peak gain of 8.55 dB can be seen at a centre frequency of 10 GHz.

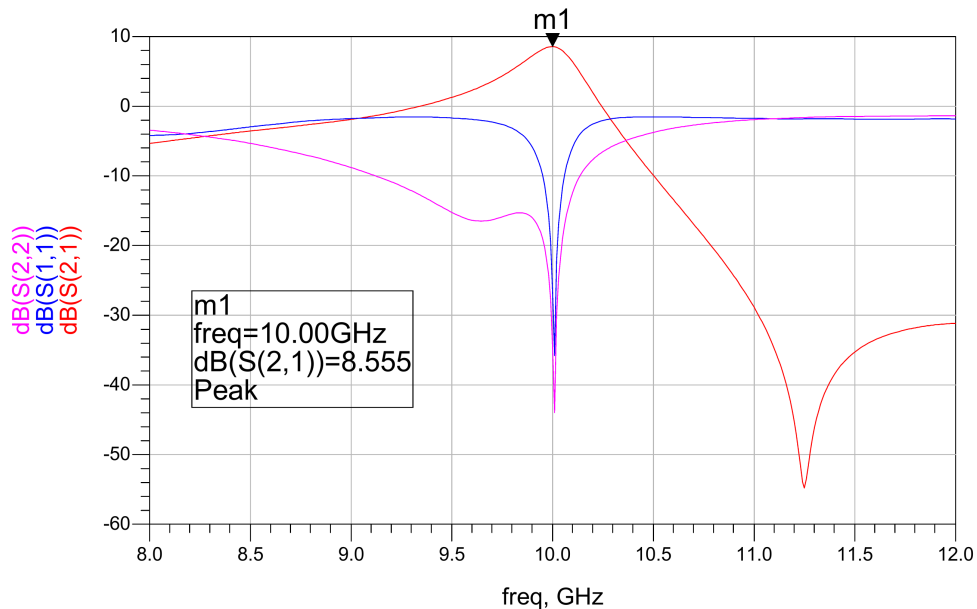


Figure 5.5: Simulated S-Parameters for the CGH40010 power amplifier circuit.

### 5.1.2 Measured Performance

The gain of the amplifier was measured using standard VNA. A 16 dB attenuator was placed on each port of the network analyser in order to protect it against any oscillations at the input or output of the amplifier. The frequency response is shown in figures 5.6 and 5.7 where a peak gain of 8.4 dB can be seen at 9.2 GHz.

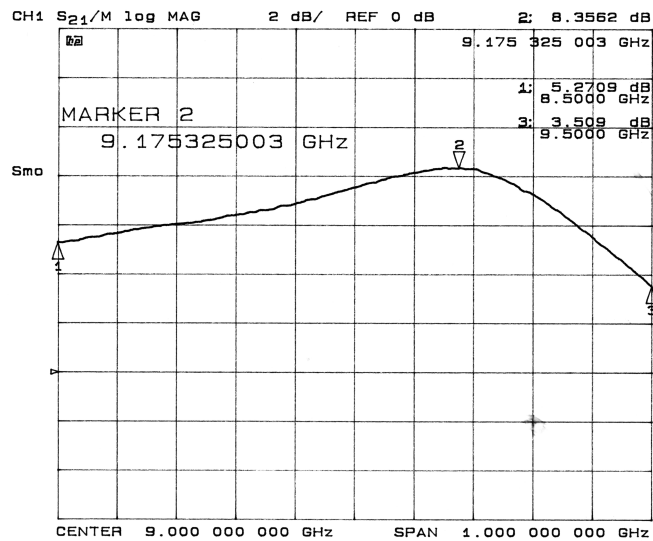


Figure 5.6: Frequency Response of GaN Power Amplifier - A 1 GHz span is shown.

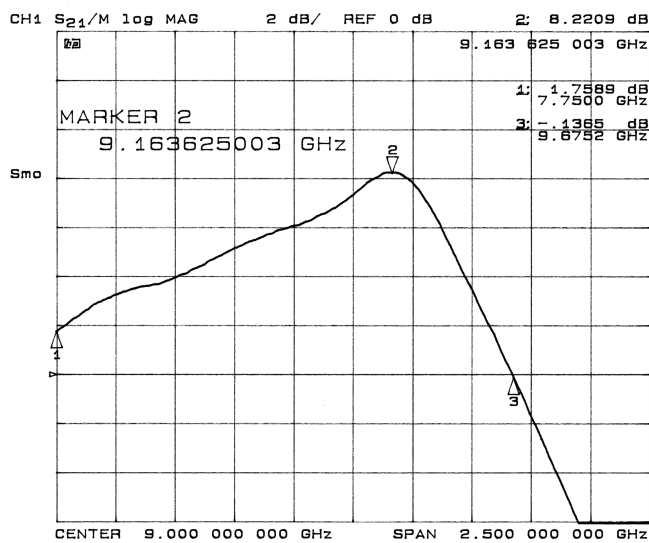


Figure 5.7: Frequency Response of GaN Power Amplifier - A 2.5 GHz span is shown.

The centre frequency is a little low, possibly due to less accurate models for the device and package as we are operating far outside the normal operating range as well as the accuracy of the matching network. It is important to note that the input capacitance is also rather high (5 pF) partly due to the package. This also places constraints on the bandwidth.

The noise figure of the amplifier was measured using a HP8970B noise figure meter. The standard double side band (DSB) technique was used [57], a diagram of the measurement apparatus is shown in figure 5.8:

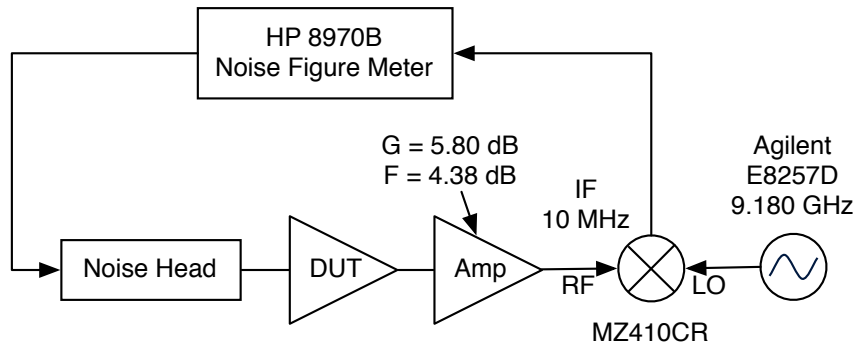


Figure 5.8: Noise figure measurement system.

The equipment was calibrated by connecting the noise head directly to the input of the preamp. The preamp is required in order to increase the signal level into the noise figure meter due to the extra insertion loss caused by the mixer conversion loss. The measurement results are shown in table 5.2 where a relatively low noise figure of 4.57 dB is observed at a drain current of 200 mA increasing to 5.16 dB for a drain current of 500 mA.

$V_{GS}$ (V)	$I_D$ (mA)	Gain (dB)	Noise Figure (dB)
-3.136	100	7.33	4.56
-2.981	200	8.11	4.57
-2.833	300	8.25	4.73
-2.689	400	8.17	4.93
-2.536	500	7.99	5.16

Table 5.2: Noise figure measurements for the CGH40010 GaN power amplifier with a drain source voltage of  $V_{DS} = 28$  V

### 5.1.3 Residual Phase Noise Measurement

A residual phase noise measurement was taken on the GaN amplifier. The measurement was performed using the single channel technique described in section 4.2 of chapter 4. The maximum bandwidth of this measurement system was limited to 100 kHz and the measurement noise floor was also limited as at this stage as the two channel cross correlation system, described in chapter 4, had not been built. The input power to the amplifier was limited to +3.3 dBm, as the input power to the mixer of the single channel residual noise measurement system is limited to +10 dBm.

It is possible to estimate the noise floor and hence the flicker noise corner level using extrapolation. If we assume that the flicker noise slope is  $1/f$  (10 dB/decade) and the noise figure is 4.2 dB then using equation (5.1.10) we can estimate the thermal noise floor to be around -176 dBc/Hz and hence the flicker noise corner (at these operating conditions) to be around 2 MHz. The measurements results and extrapolated characteristics are shown in figure 5.9 on page 113.

$$L(f) = -177 + N_A - P_i \quad (5.1.9)$$

$$= -177 + 4.2 - 3.3 \quad (5.1.10)$$

An alternative flicker noise Figure of Merit could be the flicker noise level at 10Hz (-123 dBc/Hz) or 1 Hz (-113 dBc/Hz) as these should be power independent (thereby remaining constant) assuming there are no additional non linear effects. It should be noted that if this amplifier was operated with 1 Watt output power then extrapolations would suggest a noise floor around -195 dBc/Hz and for 10 Watts around -205 dBc/Hz! This assumes (as mentioned earlier) that there are no additional non linear effects. It can be seen that very low noise floors can be achieved although at present the flicker noise corners are rather high. The flicker noise performance of this amplifier could be improved using circuit level techniques. It has been demonstrated that the feed-forward technique can be used to improve the residual noise characteristics of an amplifier [58] [59] [60]. Everard and Broomfield[59] demonstrated a 1 Watt 7.7 GHz feed-forward amplifier with a 20 dB flicker noise power reduction over a 1 to 30 kHz offset range. Sokolov [60] also demonstrated a 20 dB gain 10 GHz feed-forward amplifier with up to 20 dB of noise suppression from 1KHz through 100 kHz.

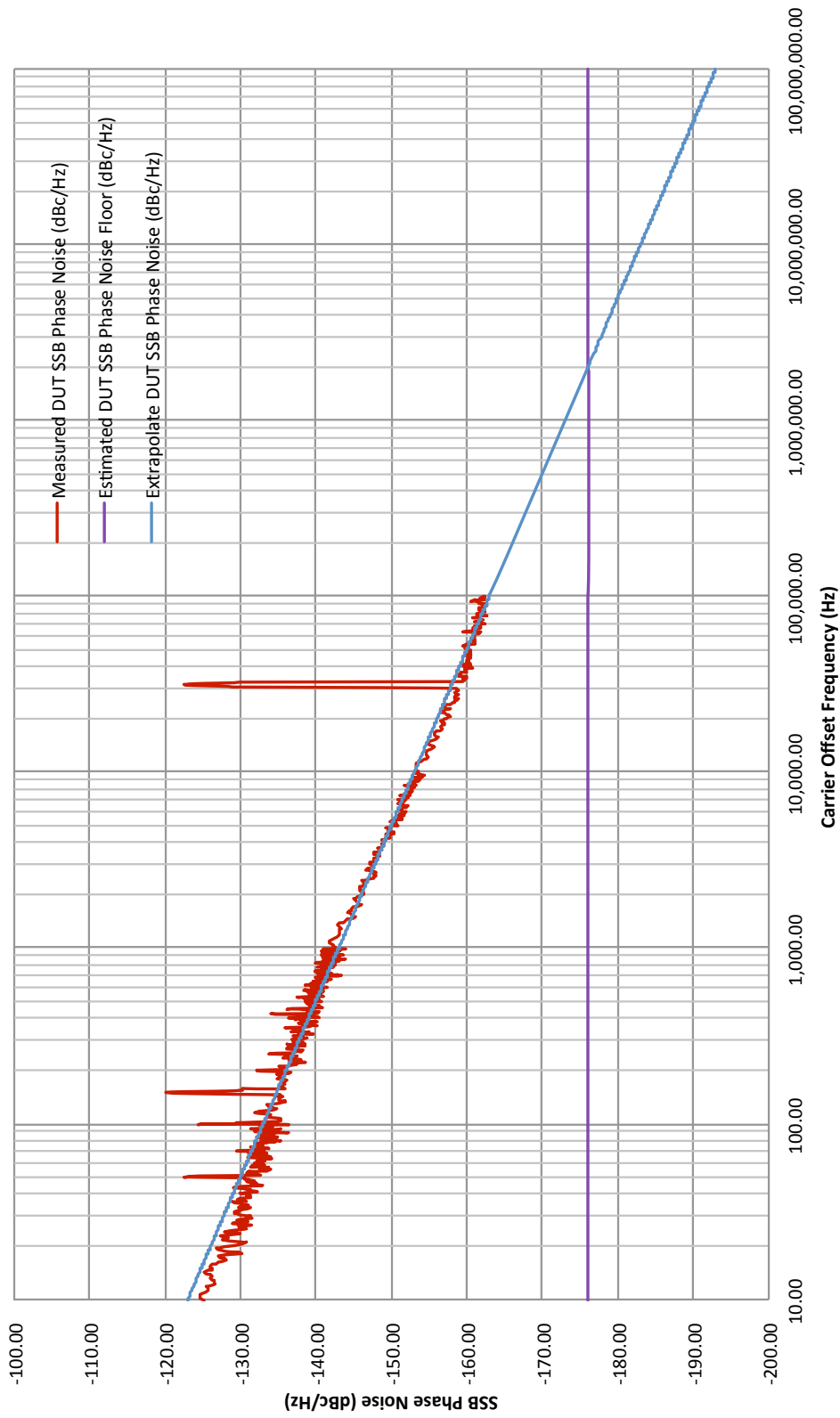


Figure 5.9: Residual phase noise measurements of the CGH40010 GaN power amplifier. The purple trace shows the estimated thermal noise floor and the blue trace shows the extrapolated  $1/f$  residual phase noise characteristic.

## 5.2 Digital Frequency Divider

Frequency dividers have many applications, they are used extensively in phase-locked loop frequency synthesisers, measurement systems and communications equipment. A low phase noise frequency divider can be used to improve the phase noise performance of a lower quality reference signal. A frequency divider will reduce the carrier frequency by the division ratio,  $n$  while also reducing the phase noise by a factor of  $20 \log_{10} n$  dB. This equates to a 6 dB reduction in phase noise for each halving of the input frequency. This improvement in phase noise will only occur until the residual noise floor of the divider is reached.

There are many different circuit configurations that can be used to build a frequency divider. One of the most popular forms, frequently seen in the literature [61][62][63], is the static digital frequency divider. This type of divider usually employs a master-slave D flip-flop arrangement with negative feedback. A simplified block diagram is shown in figure 5.10:

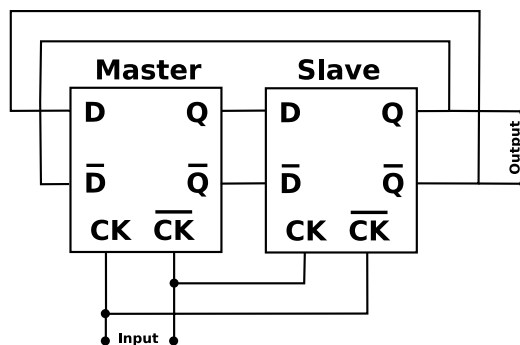


Figure 5.10: Simplified static frequency divider

The master-slave latch pair in this configuration act as an edge triggered D-Type flip-flop where the output can only change state on one of the clock edges. The specific edge used depends on the implementation of the latches. It can be seen from Figure 5.10 that the output,  $Q$ , is fed back into the inverting data input,  $\bar{D}$ , and the inverted output,  $\bar{Q}$ , is fed back to the non-inverting data input. This ensures that the output can only change state on every other clock edge which results in a halving of the frequency of any input placed on the clock lines.

In order to ensure operation with a high frequency input signal it is desirable that each of the latches operate as quickly as possible. In this work we use a circuit configuration known as emitter coupled logic (ECL), the transistors in this type of circuit never saturate and as such do not suffer from the problems

of base charge storage. This ensures that their turn on and turn off transients are as rapid as possible.

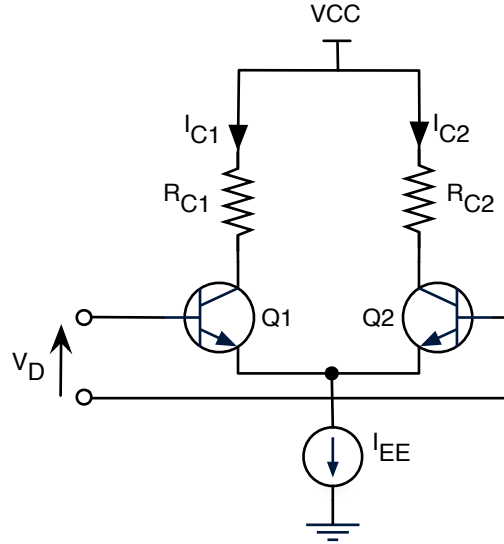


Figure 5.11: Simplified emitter coupled logic (ECL) inverter

The simplified schematic of a typical ECL inverter gate is shown in figure 5.11. The input voltages are applied to the base of transistors Q1 and Q2 and the output voltages are taken from the collectors of each transistor. The current source,  $I_{EE}$  is used to bias the transistors into their linear region. The ratio of the collector currents as a function of the differential input voltage,  $V_D$ , for the circuit in figure 5.11 can be written as:

$$\frac{I_{C1}}{I_{C2}} = e^{(V_{BE1} - V_{BE2})/V_T} \approx e^{V_D/V_T} \quad (5.2.1)$$

$$I_{C1} + I_{C2} \approx I_{EE} \quad (5.2.2)$$

With reference to Equation (5.2.1) it can be seen that if the transistors are matched then the ratio of the collector currents is a simple function of the differential input voltage,  $V_d$ . If we ignore the base current then for a small differential input voltage the collector current is almost entirely transferred into one of the transistors. This simple circuit operates as a current switch and as a result of the resistors  $R_{C1}$  and  $R_{C2}$  the input signal is inverted and amplified at the collectors.

The transistors in this circuit must not be allowed to saturate or the turn on and turn off transients will become unacceptably long as a result of the additional base current that must be supplied. Operation away from the sat-

uration region is guaranteed providing that the base voltage is not allowed to rise more than half a volt above the collector voltage, this ensures that the collector base junction does not become forward biased. The principal limitation of this style of circuit is that the output swing is limited to around 0.5 Volts or 1 Volt when taken differentially.

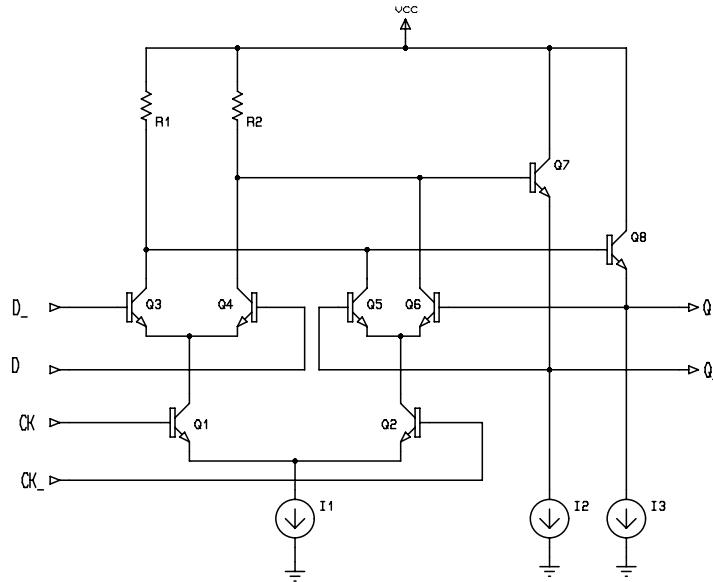


Figure 5.12: Simplified ECL D-Latch

The circuit of figure 5.11 can be extended to provide the D-latch function required for a divider. A simplified schematic of an ECL D Latch is shown in Figure 5.12. Current source I1 is used to bias the transistors into their linear region. The clock differential pair, transistors Q1 and Q2, is then used to switch this current into either the tracking or the latch pair. If the  $CK$  input is raised more than a few tens of millivolts above the  $\bar{CK}$  input then the majority of the bias current, I1, is transferred into the tracking pair and the outputs  $Q$  and  $\bar{Q}$  follow the input voltages  $D$  and  $\bar{D}$ . If the differential input voltage is reversed then the bias current is transferred into the latch pair and the output voltage remains fixed regardless of the values present at the inputs. The latch is implemented with the cross-coupled pair consisting of transistors Q5 and Q6. These transistors form a bistable element which is used to store the data input. Transistors Q7 and Q8 are required to buffer the output and to provide a single  $V_{be}$  drop so that the input transistors in the next stage do not saturate. The truth table for this circuit is shown in Table 5.3.

$D_n$	$CK_n$	$Q_{n+1}$
0	0	$Q_n$
0	1	0
1	0	$Q_n$
1	1	1

Table 5.3: Truth Table for the circuit in figure 5.12

This is the truth table of a D-type latch and if two of these latch elements are combined as illustrated in figure 5.13 then a frequency divider can be realised:

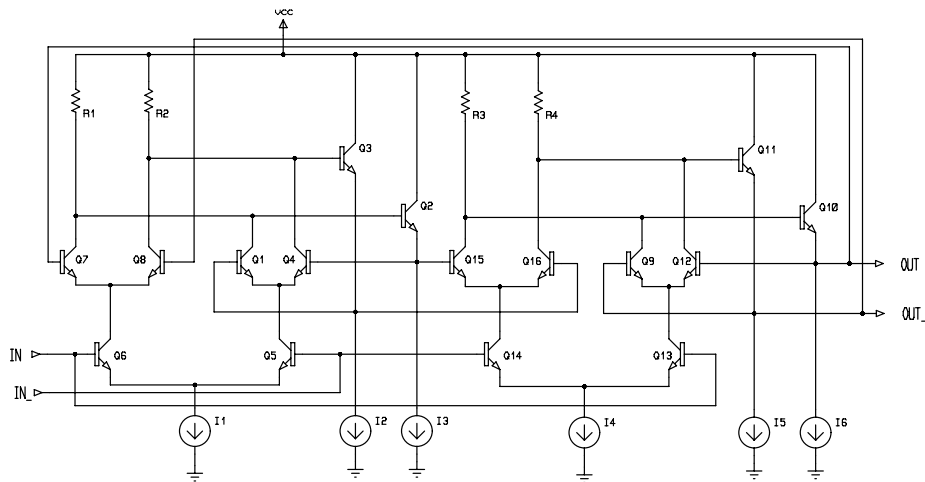
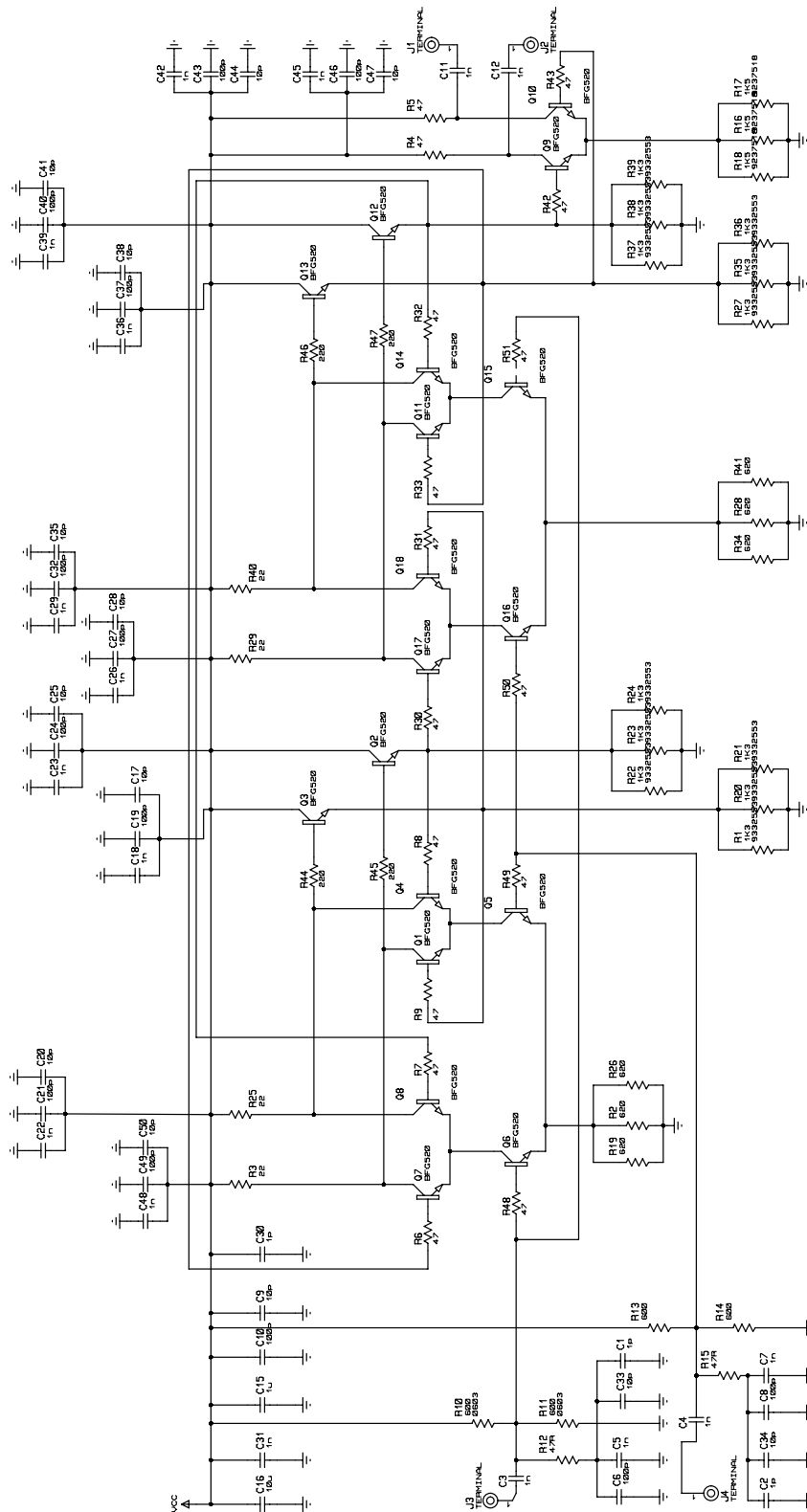


Figure 5.13: Simplified ECL frequency divider schematic

A digital frequency divider based on this design has been constructed using discrete components. Infineon BFG520 transistors were used as these devices have previously exhibited excellent residual noise performance in number of amplifiers our research group has built. To enable ease of measurement it was decided to produce a compact design using a 4-layer PCB where the layout was symmetrically optimised to reduce delay and ensure stability. This required extensive simulation and optimisation as well as the use of additional stability resistors. The maximum operational input frequency of the divider was measured to be 800 MHz with a single ended output power into  $50\Omega$  of 0 dBm. The complete divider circuit is illustrated in figure 5.14 on page 118. It consists of two interconnected D latch stages and an output buffer.



### 5.2.1 Residual Phase Noise Measurements

A residual phase noise measurement was taken on the digital divider, the measurement apparatus is shown in figure 5.15. Two frequency dividers are required because we are measuring a frequency translating device. As a result, the measured phase noise is the sum of the noise from each divider and it is therefore necessary to subtract 3 dB from the measured values.

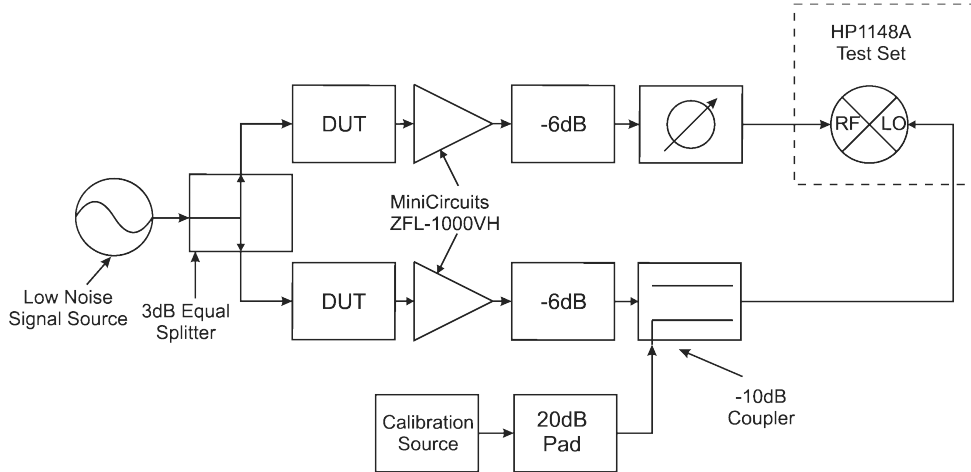


Figure 5.15: Digital divider residual phase noise measurement system

A variable frequency low noise signal generator is used to provide the input and this signal is equally split into two separate paths each containing a frequency divider. The output from each DUT is then fed into a low noise amplifier in order to raise the signal level and reduce the noise floor of the measurement system. Initially a 6 dB attenuator was placed at the output of each amplifier to protect the measurement system. A 10 dB coupler is placed in one arm of the system for calibration purposes and a variable phase shifter is placed in the other arm. Each arm is then connected to the low frequency phase detector input of the HP1148A test set. The components were shielded from RFI by placing them in an electrically screened box. The DUT's and the buffer amplifiers at their outputs were all powered from batteries to reduce unwanted interference. The noise generated by the input signal source is present in both phase detector paths and correlated at the phase detector input. This ensures that the source phase noise cancels at the phase detector input. The amplitude noise of the signal source is assumed to be relatively small such that it is suppressed by the phase detector. The measurement system was calibrated using a single side band spur, this is a very accurate calibration method as all the non-linearities and harmonics of the phase detector are accounted for [52].

A noise floor measurement was performed in order to establish a reference value for the residual phase noise present in the measurement system. This results is shown in the green trace of figure 5.16 on page 121. The red and blue traces represent the residual phase noise measurements of the divider at 443 MHz and 192 MHz respectively.

It can clearly be seen from these results that the flicker noise corner is above 10 kHz with a far from carrier noise floor of -155 dBc/Hz. The far out noise floor is comparable to that of a commercial ECL divider circuit, such as the Zarlink SP8402 [64]. However, the close to carrier noise in this design is much worse than the commercial Zarlink product. The SP8402 phase noise at a 100 kHz offset is better than -150 dBc/Hz.

It has been shown [65] that changes in the triggering voltage level are the origin of the phase noise present at the output of a digital frequency divider. These changes in triggering voltage are typically a result of the noise sources present in the active and passive devices which make up the divider as well as changes in device operating points as a result of temperature variations. It is therefore suggested that the increased close to carrier noise in our circuit may be a result of the series base resistors required for stability.

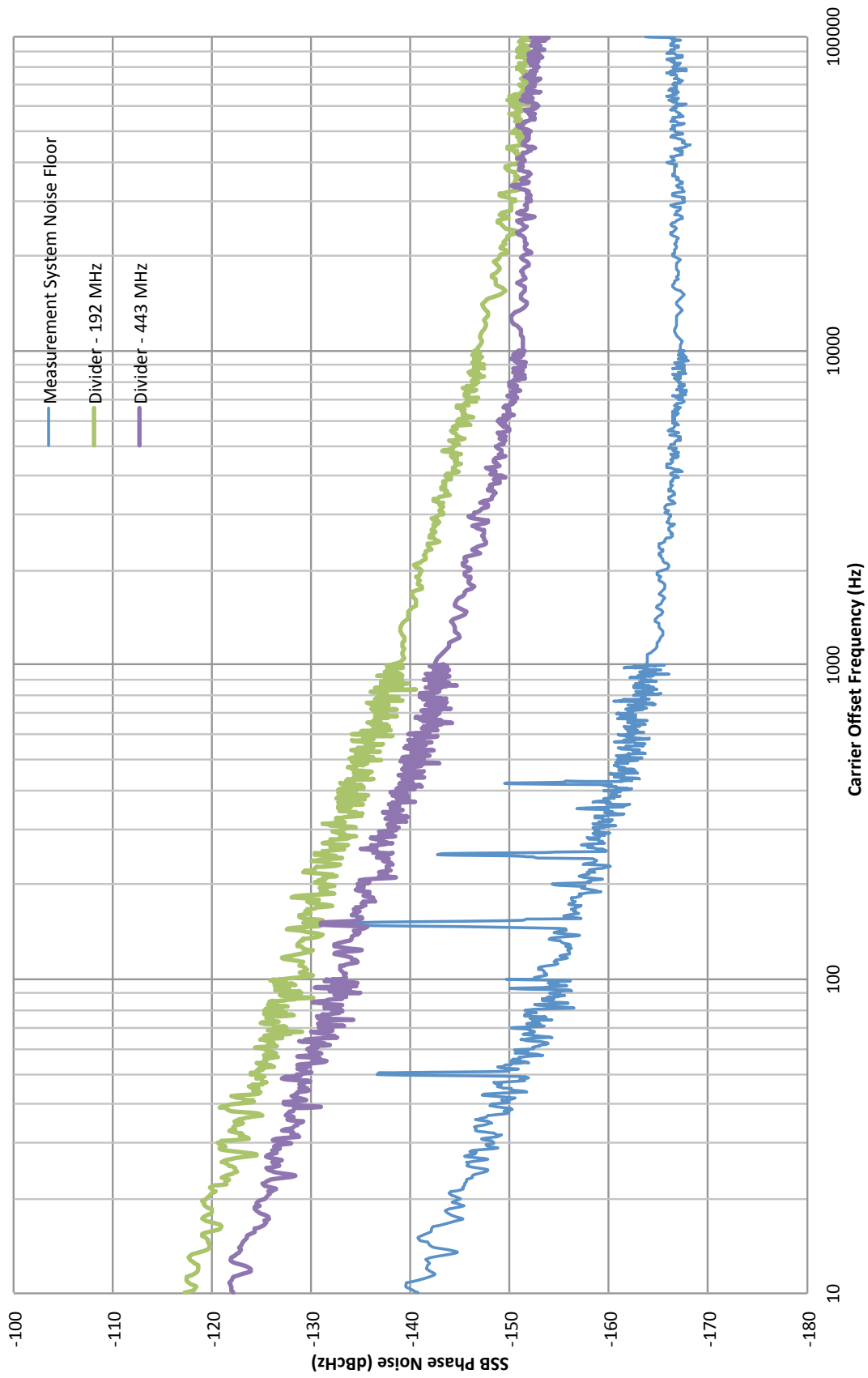


Figure 5.16: Discrete ECL digital divider residual phase noise measurements. The blue trace shows the noise floor of the measurement system. The green trace shows the divider phase noise with an input frequency of 192 MHz and the purple trace shows the divider phase noise with an input frequency of 443 MHz

# Chapter 6

## Conclusions and Further Work

The main objectives of this research have been to develop high Q resonators and a low noise measurement system for use in low noise oscillators. The following sub-sections summarise the main results in each chapter and provide some suggestions for future research.

### 6.1 High Q Distributed Bragg Resonator

A high quality factor X-Band distributed Bragg resonator has been developed. This resonator utilises an aperiodic arrangement of non  $\lambda/4$  low loss alumina plates mounted in a cylindrical waveguide. The dielectric plates and air waveguide dimensions were optimised using a genetic algorithm to achieve maximum quality factor by redistributing the energy loss within the cavity. An unloaded quality factor ( $Q_0$ ) of 196,000 was demonstrated at 9.94 GHz.

The resonant frequency of 9.94 GHz is in good agreement with the simulated result of 10 GHz. The unloaded quality factor of 196,797 is considerably lower than the simulated value of 400,000. The increased loss in the resonator is thought to be a result of the following factors:

- Increased side and end wall losses resulting from poor conductivity of the resonator shield.
- The introduction of discontinuities into the cavity as a result of the structures required to support the dielectric plates.
- An increase in the loss tangent of the Alumina plates from the manufacturer specified value.

- The simplistic end wall model used in the ABCD waveguide simulations. The FDTD-BOR field simulator indicated that the initial end wall model underestimated the end wall losses and as a result the genetic algorithm incorrectly sized the dielectric plates.

Theoretical simulations predicted that the Bragg resonator could offer broad electro-mechanical tuning if the length of the centre section can be varied. The initial attempt to build a tuneable structure failed and resulted in an enormously degraded quality factor. The author believes that it will be possible to build a tuneable resonator if a sealed structure can be devised that does not introduce significant discontinuities into the central resonant section of the Bragg structure.

The following additional recommendations are made for future research on this topic. A silver plated cavity should be constructed in order to determine the effect of the side and end wall losses. The coupling probes should be mounted at the ends of the cavity rather than in the side walls. This will reduce the discontinuities introduced by the probes, with the possible disadvantage of a reduced coupling coefficient. Finally, the genetic algorithm should be applied to the FDTD-BOR solver. This will allow realistic modelling of the end wall losses. A single field simulation takes several minutes to complete, it will therefore be necessary to modify the existing genetic algorithm so that a local gradient search technique is employed to refine the solutions located by the genetic algorithm. This approach will hopefully reduce the total number of generations required to find the optimal cavity dimensions.

## 6.2 Cross Correlation Residual Phase Noise Measurement System

A cross correlation residual phase noise measurement system was demonstrated with a noise floor in excess of -200 dBc/Hz for 100,000 correlations. This is an improvement of 20 dB when compared with the same system operating with a single channel. No additional AM suppression was required to achieve this result. However, the reduction in noise floor came at the expense of increased measurement time and system complexity.

Unfortunately the close to carrier noise performance of the system, at frequency offsets below 1 kHz, did not show the same level of suppression. This was thought to be a result of the high levels of spurs that were present in the

10 Hz to 1 kHz region. It may be possible to reduce or completely remove some of these spurs by removing the power supplies from the HP11848A units and running the equipment from batteries.

Future research on this topic should be directed towards evaluating the capability of this system for full phase locked oscillator phase noise measurements.

### **6.3 Residual Phase Noise Measurements of Microwave Components**

A Gallium Nitride (GaN) power amplifier has been designed with a noise figure of 4.2 dB and an estimated thermal noise floor of -176 dBc/Hz. Unfortunately the amplifier exhibited a flicker noise corner of 2 MHz. The flicker noise performance of this amplifier could be improved using circuit level techniques such as the Feedforward configuration.

A static digital frequency divider has been designed with a far from carrier phase noise floor of -155 dBc/Hz and a flicker noise corner around 10 kHz. The divider achieved a maximum operational input frequency of 800 MHz. The master-slave D-latch arrangement used in this circuit has the advantage that the output edge jitter is only a function of the slave latch [66]. It is therefore only necessary to optimise the noise performance of the slave latch. One way to achieve lower noise operation would be to increase the output voltage swing. Unfortunately, the output of each latch is DC coupled and a larger voltage swing will forward bias the collector base junction of the input stage transistors in the next latch. Future research on this topic should be directed towards developing a circuit topology that allows increased output voltage swing without compromising the maximum operational speed of the divider circuit.

### **6.4 General Research Recommendations**

The author believes that future research towards ultra low phase noise oscillators should focus on the development of extremely low residual phase noise amplifiers combined with flicker noise reduction techniques such as the Feedforward configuration. These amplifiers could then be combined with a high Q tuneable Bragg resonator structure to produce an oscillator with a phase

noise performance comparable to the cryogenically cooled Sapphire oscillators present in the literature.

A cross correlation phase noise measurements system similar to the instrument described in this thesis will then be required to measure the extremely low noise levels.

# Bibliography

- [1] J. A. McNeill and D. Ricketts, *The Designer's Guide Jitter in Ring Oscillators*. Springer Verlag, 2009.
- [2] "Analysis of clutter cancellation capability considering radar system phase noise effects," in *IEEE Antennas and Propagation Society International Symposium*, Jul. 1997, pp. 2442–2445.
- [3] R. Narayanan and M. Dawood, "Doppler estimation using a coherent ultrawide-band random noise radar," *IEEE Transactions on Antennas and Propagation*, vol. 48, no. 6, pp. 868–878, Jun. 2000.
- [4] W. P. Robins, *Phase noise in signal sources*, ser. theory and applications. Peter Peregrinus Ltd, 1984.
- [5] "The aging of bulk acoustic wave resonators, filters and oscillators," in *Proceedings of the 45th Annual Symposium on Frequency Control*, May 1991, pp. 77–101.
- [6] E. Rubiola, *Phase Noise and Frequency Stability in Oscillators (The Cambridge RF and Microwave Engineering Series)*, 1st ed. Cambridge University Press, Nov. 2008.
- [7] D. B. Leeson, "A simple model of feedback oscillator noise spectrum," *Proceedings of the IEEE*, vol. 54, no. 2, pp. 329–330, Feb. 1966.
- [8] J. Everard, *Fundamentals of RF Circuit Design with Low Noise Oscillators*, 1st ed. Wiley-Blackwell, Dec. 2000.
- [9] U. L. Rohde, A. K. Poddar, and G. Bock, *The Design of Modern Microwave Oscillators for Wireless Applications: Theory and Optimization*. John Wiley and Sons, 2005.

- [10] “IEEE Standard Definitions of Physical Quantities for Fundamental Frequency and Time Metrology - Random Instabilities,” *IEEE Standard 1139-2008*, 2008.
- [11] P. J. Fish, *Electronic Noise and Low Noise Design*. The Macmillan Press, 1993.
- [12] A. Van Der Ziel, “Thermal Noise at High Frequencies,” *Journal of Applied Physics*, vol. 21, no. 5, pp. 399–401, 1950.
- [13] K. Theodoropoulos, “Residual Phase Noise Modelling of Silicon Bipolar Amplifiers and Ultra Low Phase Noise Ceramic Dielectric Resonator Oscillators,” Ph.D. dissertation, University of York, Department of Electronics, University of York, Sep. 2009.
- [14] A. Van Der Ziel, “Unified presentation of 1/f noise in electron devices: fundamental 1/f noise sources,” *Proceedings of the IEEE*, vol. 76, no. 3, pp. 233–258, Mar. 1988.
- [15] M. B. Weissman, “1/ f noise and other slow, nonexponential kinetics in condensed matter,” *Reviews of modern physics*, vol. 60, no. 2, pp. 537–571, 1988.
- [16] K. Theodoropoulos and J. Everard, “Residual phase noise modeling of amplifiers using silicon bipolar transistors,” *IEEE Transactions on Ultrasonics, Ferroelectrics, and Frequency Control*, vol. 57, no. 3, pp. 562–573, Mar. 2010.
- [17] “An X-Band GaAs FET Oscillator Using a Dielectric Resonator,” in *37th Annual Symposium on Frequency Control*, 1983, pp. 481–484.
- [18] S. J. Fiedziuszko, I. C. Hunter, T. Itoh, Y. Kobayashi, T. Nishikawa, S. N. Stitzer, and K. Wakino, “Dielectric materials, devices, and circuits,” *IEEE Transactions on Microwave Theory and Techniques*, vol. 50, no. 3, pp. 706–720, Mar. 2002.
- [19] C. McNeilage, J. H. Searls, E. N. Ivanov, P. R. Stockwell, D. M. Green, and M. Mossamaparast, “A review of sapphire whispering gallery-mode oscillators including technical progress and future potential of the technology,” in *Proceedings of the IEEE Frequency Control Symposium and Exposition*, Aug. 2004, pp. 210–218.

- [20] M. E. Tobar, J. Krupka, E. N. Ivanov, and R. A. Woode, "Anisotropic complex permittivity measurements of mono-crystalline rutile between 10 and 300 K," *Journal of Applied Physics*, vol. 83, no. 3, pp. 1604–1609, 1998.
- [21] C. A. Flory and R. C. Taber, "High performance distributed Bragg reflector microwave resonator," *IEEE Transactions on Ultrasonics, Ferroelectrics, and Frequency Control*, vol. 44, no. 2, pp. 486–495, Mar. 1997.
- [22] C. A. Flory and H. L. Ko, "Microwave oscillators incorporating high performance distributed Bragg reflector microwave resonators," *IEEE Transactions on Ultrasonics, Ferroelectrics, and Frequency Control*, vol. 45, no. 3, pp. 824–829, May 1998.
- [23] C. J. Maggiore, A. M. Clogston, G. Spalek, W. C. Sailor, and F. M. Mueller, "Low-loss microwave cavity using layered-dielectric materials," *Applied Physics Letters*, vol. 64, no. 11, pp. 1451–1453, 1994.
- [24] J. Krupka, A. Cwikla, M. Mrozowski, R. N. Clarke, and M. E. Tobar, "High Q-factor microwave Fabry-Perot resonator with distributed Bragg reflectors," *IEEE Transactions on Ultrasonics, Ferroelectrics, and Frequency Control*, vol. 52, no. 9, pp. 1443–1451, Sep. 2005.
- [25] M. E. Tobar, J.-M. Le Floch, D. Cros, J. Krupka, J. D. Anstie, and J. G. Hartnett, "Spherical Bragg reflector resonators," *IEEE Transactions on Ultrasonics, Ferroelectrics, and Frequency Control*, vol. 51, no. 9, pp. 1054–1059, Sep. 2004.
- [26] J. Krupka, M. E. Tobar, J. G. Hartnett, D. Cros, and J.-M. Le Floch, "Extremely high-Q factor dielectric resonators for millimeter-wave applications," *IEEE Transactions on Microwave Theory and Techniques*, vol. 53, no. 2, pp. 702–712, Feb. 2005.
- [27] J. Breeze, J. Krupka, and N. M. Alford, "Enhanced quality factors in aperiodic reflector resonators," *Applied Physics Letters*, vol. 91, no. 15, 2007.
- [28] J.-M. Le Floch, M. E. Tobar, D. Mouneyrac, D. Cros, and J. Krupka, "High-Q Cylindrical Alumina Resonator Based on Bragg Confined Mode of Azimuthal Mode Number Greater Than Zero," in *Frequency Control*

- Symposium, 2007 Joint with the 21st European Frequency and Time Forum. IEEE International*, 2007, pp. 678–680.
- [29] C. A. Balanis, *Advanced Engineering Electromagnetics*. John Wiley & Sons, 1989.
- [30] D. M. Pozar, *Microwave Engineering*, 3rd ed. John Wiley & Sons, 2005.
- [31] J. H. Holland, *Adaptation in Natural and Artificial Systems: An Introductory Analysis with Applications to Biology, Control, and Artificial Intelligence*. A Bradford Book, Apr. 1992.
- [32] T. Baeck, D. B. Fogel, and Z. Michalewicz, Eds., *Evolutionary Computation 1: Basic Algorithms and Operators*. Taylor & Francis, Jan. 2000.
- [33] S. Luke, *Essentials of Metaheuristics*. lulu.com, Mar. 2011.
- [34] J. Shaffer, R. Caruna, and L. Eshelman, *A Study of the Control Parameters Affecting Online Performance of Genetic Algorithms for Function Optimisation*. Proceedings of the third international conference on Genetic algorithms, 1989.
- [35] K. Yee, “Numerical solution of initial boundary value problems involving maxwell’s equations in isotropic media,” *IEEE Transaction on Antennas and Propagation*, vol. 14, no. 3, pp. 302–307, May 1966.
- [36] A. Taflove, *Computational electrodynamics : the finite-difference time-domain method*. Boston: Artech House, 1995.
- [37] L. Tarricone, *Grid computing for electromagnetics*. Boston: Artech House, 2004.
- [38] Y. Chen, R. Mittra, and P. Harms, “Finite-difference time-domain algorithm for solving Maxwell’s equations in rotationally symmetric geometries,” *IEEE Transactions on Microwave Theory and Techniques*, vol. 44, no. 6, pp. 832–839, Jun. 1996.
- [39] D. Kajfez, A. Elsherbeni, and A. Mokaddem, “Higher order modes in dielectric resonators,” in *Antennas and Propagation Society International Symposium*, 1996, pp. 306–309.

- [40] A. Z. E. V Rodriguez-Pereyra and C. E. Smith, "A Body Of Revolution Finite Dfference Time Domain Method With Perfectly Matched Layer Absorbing Boundary," *Progress In Electromagnetics Research*, vol. 24, pp. 257–277, 1999.
- [41] K. S. Yee, K. Shlager, and A. H. Chang, "An algorithm to implement a surface impedance boundary condition for FDTD," *IEEE Transactions on Antennas and Propagation*, vol. 40, no. 7, pp. 833–837, Jul. 1992.
- [42] J. H. Beggs, R. J. Luebbers, K. S. Yee, and K. S. Kunz, "Finite-difference time-domain implementation of surface impedance boundary conditions," *IEEE Transactions on Antennas and Propagation*, vol. 40, no. 1, pp. 49–56, Jan. 1992.
- [43] J. G. Maloney and G. S. Smith, "The use of surface impedance concepts in the finite-difference time-domain method," *IEEE Transactions on Antennas and Propagation*, vol. 40, no. 1, pp. 38–48, Jan. 1992.
- [44] C. Wang, B.-Q. Gao, and C.-P. Deng, "Accurate study of Q-factor of resonator by a finite-difference time-domain method," *IEEE Transactions on Microwave Theory and Techniques*, vol. 43, no. 7, pp. 1524–1529, Jul. 1995.
- [45] C. M. Furse and O. P. Gandhi, "Why the DFT is faster than the FFT for FDTD time-to-frequency domain conversions," *IEEE Microwave and Guided Wave Letters*, vol. 5, no. 10, pp. 326–328, 1995.
- [46] D. M. Pozar, "Microwave Resonators," in *Microwave Engineering*. John Wiley & Sons, 2005, pp. 282–287.
- [47] C. A. Balanis, "Circular Cross-Section Waeguides and Cavities," in *Advanced Engineering Electromagnetics*. John Wiley & Sons, 1989, pp. 492–498.
- [48] J. K. A. Everard, "Low-noise power-efficient oscillators: theory and design," *IEE Proceedings G Electronic Circuits and Systems*, vol. 133, no. 4, pp. 172–180, Aug. 1986.
- [49] E. Rubiola and V. Giordano, "Improved interferometric method to measure near-carrier AM and PM noise," *IEEE Transaction on Instrumentation and Measurement*, Apr. 1999.

- [50] W. F. Walls, "Cross-correlation phase noise measurements," in *Proc 46th IEEE Frequency Control Symposium*, 1992, pp. 257–261.
- [51] G. Cibiel, M. Régis, E. Tournier, and O. Llopis, "AM noise impact on low level phase noise measurements," *IEEE Transactions on Ultrasonics, Ferroelectrics, and Frequency Control*, vol. 49, no. 6, pp. 784–788, 2002.
- [52] Agilent, *HP 3048A Phase Noise Measurement System Reference Manual*, Agilent Technologies, Sep. 1989.
- [53] E. Rubiola and F. Vernotte. (2010, Feb.) The cross-spectrum experimental method. [Online]. Available: <http://arxiv.org/pdf/1003.0113v1>
- [54] R. G. Lyons, *Understanding Digital Signal Processing (3rd Edition)*, 3rd ed. Prentice Hall, Nov. 2010.
- [55] J. Everard and K. Theodoropoulos, "Ultra-Low Phase Noise Ceramic based Dielectric Resonator Oscillators," in *IEEE International Frequency Control Symposium and Exposition*, Jun. 2006, pp. 869–874.
- [56] J. K. A. Everard and C. D. Broomfield, "Reduced transposed flicker noise in microwave oscillators using GaAs-based feedforward amplifiers," *IEEE Transactions on Ultrasonics, Ferroelectrics, and Frequency Control*, vol. 54, no. 6, pp. 1108–1117, Jun. 2007.
- [57] Agilent. Fundamentals of RF and Microwave Noise Figure Measurements. [Online]. Available: <http://www.home.agilent.com>
- [58] D. A. Howe and A. Hati, "Low-noise x-band oscillator and amplifier technologies: comparison and status," in *Proceedings of the 2005 IEEE International Frequency Control Symposium and Exposition*, 2005, pp. 481–487.
- [59] C. Broomfield and J. Everard, "Flicker noise reduction using GaAs microwave feedforward amplifiers," *Proceedings of the IEEE/EIA International Frequency Control Symposium and Exhibition, 2000.*, pp. 525–530, 2000.
- [60] V. Sokolov, J. Kruchowski, M. Vickberg, B. Buhrow, S. Schuster, J. Bublitz, B. Gilbert, and E. Daniel, "An X-band hybrid MIC feedforward amplifier for low residual noise operation," *Microwave Symposium Digest, 2005 IEEE MTT-S International*, 2005.

- [61] L. Wang, Y.-M. Sun, J. Borngraeber, A. Thiede, and R. Kraemer, “Low Power Frequency Dividers in SiGe:C BiCMOS Technology,” in *The 6th Topical Meeting on Silicon Monolithic Integrated Circuits in RF Systems*, San Diego, USA, Jan. 2006.
- [62] “Modeling Phase Noise in Frequency Dividers,” *IEEE Transactions on Ultrasonics, Ferroelectrics, and Frequency Control*, vol. 37, no. 4, pp. 307–315, Jul. 1990.
- [63] M. Kurisu, M. Ohuchi, A. Sawairi, M. Sugiyama, H. Takemura, and T. Tashiro, “A Si bipolar 21-GHz/320-mW static frequency divider,” *IEEE Journal of Solid-State Circuits*, vol. 26, no. 11, pp. 1626–1631, Nov. 1991.
- [64] (2005, Sep.) Zarlink SP8402 Very Low Phase Noise Divider. [Online]. Available: <http://www.zarlink.com/zarlink/sp8402-datasheet-sep2005.pdf>
- [65] V. Kroupa, “Jitter and phase noise in frequency dividers,” *IEEE Transactions on Instrumentation and Measurement*, vol. 50, no. 5, pp. 1241–1243, 2001.
- [66] S. Levantino, L. Romanò, S. Pellerano, C. Samori, and A. L. Lacaita, “Phase Noise in Digital Frequency Dividers,” *IEEE Journal of Solid-State Circuits*, vol. 39, no. 5, pp. 775–784, May 2004.

# Appendix A

## List of Publications

The following publications have resulted as part of this work:

### Journal Publications

S. Bale and J. Everard, "High-Q X-band distributed Bragg resonator utilizing an aperiodic alumina plate arrangement," *IEEE Trans. Ultrason. Ferroelectr. Freq. Control*, vol.57, no.1, pp.66-73, Jan. 2010.

### Conference Publications

Simon. Bale, D. Adamson, B. Wakley, J. Everard, "Cross Correlation Residual Phase Noise Measurements using Two HP3048A Systems and a PC Based Dual Channel FFT Spectrum Analyser," presented at the *European Frequency and Time Forum Conference.*, Noordwijk, Netherland, 2010.

S. Bale and J. Everard, "High Q X-band distributed Bragg resonator utilising an aperiodic alumina plate arrangement," in *Frequency Control Symposium, 2009 Joint with the 22nd European Frequency and Time forum. IEEE International.*, Besancon, France, 2009, pp.232-236.

# High-Q X-Band Distributed Bragg Resonator Utilizing an Aperiodic Alumina Plate Arrangement

Simon Bale, *Student Member, IEEE*, and Jeremy Everard, *Member, IEEE*

**Abstract**—This paper describes a high-Q X-band distributed Bragg resonator that uses an aperiodic arrangement of non- $\lambda/4$  low loss alumina plates mounted in a cylindrical waveguide. An ABCD parameter waveguide model was developed to simulate and optimize the cavity. The dielectric plates and air waveguide dimensions were optimized to achieve maximum quality factor by redistributing the energy loss within the cavity. An unloaded quality factor ( $Q_0$ ) of 196 000 was demonstrated at 9.93 GHz.

## I. INTRODUCTION

HIGH-QUALITY factor microwave resonators are an important component in many communications and RADAR systems as well as the associated test equipment. They are essential elements in, for example, low-phase-noise oscillators, low-insertion-loss narrow band filters and frequency discriminators. There are several types of resonator structure that are typically used at microwave frequencies. These include the empty metal cavity resonator, the dielectric resonator and the whispering gallery mode (WGM) resonator. The unloaded quality factor ( $Q_0$ ) of an empty metal cavity resonator is limited by the conduction losses in the side and end walls of the shield. The maximum unloaded quality factor attainable from a dielectric resonator is defined by the loss tangent ( $\tan \delta$ ) of the dielectric material as well as the losses introduced by the shield used to enclose the resonator. The effect of the wall losses on the Q-factor of a dielectric resonator is highly dependent on the distance between the resonator and the walls as well as the resonant mode used. Dielectric resonators are typically operated using the  $TE_{01\delta}$  mode. Providing the walls are sufficiently far from the resonator, then the effect of the wall losses on the Q-factor is minimal. Modern dielectric resonators are capable of providing Q-factors of between 10 000 and 30 000 at 10 GHz. The performance of the dielectric loaded cavity can be further improved by using a WGM resonator. This type of structure confines the field energy to the outer edge of a ring of dielectric material and the quality factor is almost entirely defined by the loss tangent of the dielectric material. At microwave frequencies room temperature quality factors

in the region of 200 000 are achievable using sapphire [1] and 100 000 using monocrystalline rutile [2].

The distributed Bragg resonator can offer a substantial increase in quality factor when compared with traditional microwave resonators. It is a structure formed by replacing the end and/or sidewalls of an empty metal cavity with alternating layers of air and dielectric material. The sudden change in dielectric constant at each air dielectric interface causes a partial reflection of the incident electromagnetic wave. If several air-dielectric layers are combined, then more of the energy is reflected back into the central air region of the cavity and kept away from the lossy metal end walls. Fig. 1 illustrates the structure of a typical Bragg reflector.

Two distinct classes of distributed Bragg resonator can be identified in the literature and these are the periodic reflector and the aperiodic reflector. In a periodic reflector, each of the dielectric plates and air sections are one-quarter of the guide wavelength ( $\lambda_g/4$ ) in thickness to maximize their reflectivity [3]. Flory and Taber [3] and Flory and Ko [4] demonstrate experimental results for 9.0 GHz and 13.2 GHz sapphire resonators consisting of interpenetrating concentric rings and plates with quality factors of 650 000 and 450 000, respectively. Maggiore *et al.* [5] demonstrated a distributed Bragg sapphire resonator with stated Qs of  $5.31 \times 10^5$  at 18.99 GHz. Krupka *et al.* [6] demonstrated a Fabry-Perot resonator operating at 39 GHz consisting of 2 pairs of quarter-wavelength single-crystal quartz Bragg reflectors. It achieved a Q-factor of 560 000. Tobar *et al.* [7] demonstrated a Teflon spherical Bragg resonator with a stated Q of 22 000 at 13.86 GHz. Later Krupka *et al.* [8] demonstrated spherical Bragg resonators that were constructed from single-crystal YAG and quartz. The quartz resonator produced a Q-factor of  $1.04 \times 10^5$  at 26.26 GHz and the YAG resonator produced a Q of  $6.4 \times 10^4$  at 27.63 GHz.

The research group at York has also developed a very simple square-layered alumina Bragg resonator and a cylindrical-fused silica Bragg resonator [9]. Fig. 2 shows a photograph of the square-layered alumina Bragg cavity, which at the time produced a Q of 55 000 at 10 GHz due to poor material quality. This was constructed using a copper-coated printed circuit board for the sidewalls and end walls. Small metal pins were then inserted through the walls to support the dielectric plates.

In a recent paper, Breeze *et al.* [10] state that the majority of the losses in a periodic Bragg reflector occur in the first quarter wave layer and that, by redistributing the

Manuscript received May 20, 2009; accepted September 10, 2009. We thank BAE Systems, the Royal Academy of Engineering, and the University of York for supporting this work.

The authors are with the Department of Electronics, University of York, York, UK (e-mail: sjbale@ieee.org).

Digital Object Identifier 10.1109/TUFFC.2010.1380

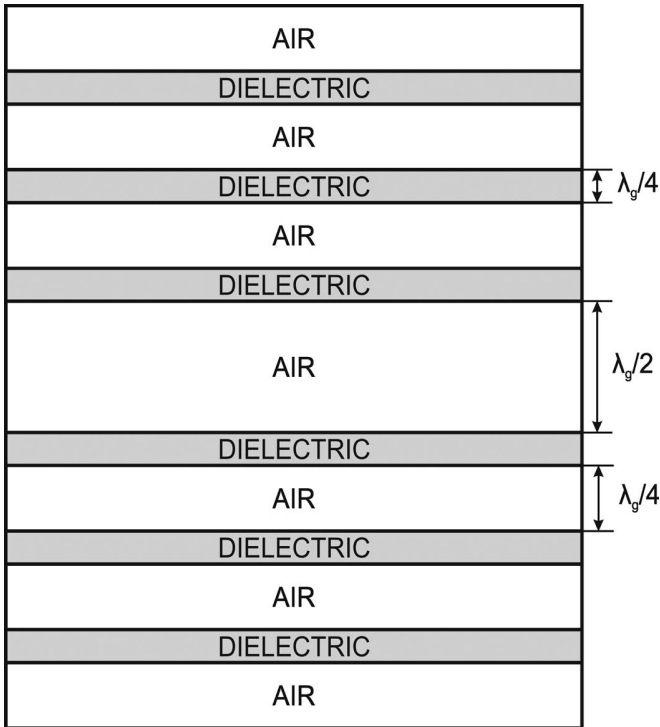


Fig. 1. The structure of a periodic Bragg resonator.

energy into the lower loss air regions, an increase in quality factor can be achieved. They demonstrate (through simulation) that by using an aperiodic arrangement of hollow dielectric spheres with thicknesses that asymptotically approach quarter wave reflectors as the cavity end walls are reached, a spherical Bragg resonator can be designed with a quality factor in excess of  $10^7$  at 10 GHz. Floch *et al.* [11] also demonstrate the development of a simple non-Maxwellian model that allows the design of Bragg resonators with dielectric reflectors of an arbitrary thickness.

In this work, which is an extension of a paper submitted to the joint EFTF-IFCS 2009 conference [12], we present the design, simulation, and measurement results for an X-band cylindrical distributed Bragg resonator that uses an aperiodic arrangement of non- $\lambda/4$  low-loss alumina plates. The paper is ordered as follows. Section II describes the resonator modeling where an ABCD parameter waveguide model is developed to ascertain and optimize the potential quality factor that can be achieved from periodic and aperiodic Bragg reflector resonators. Section III describes the simulation results for a 10-GHz periodic Bragg resonator. Section IV describes the optimization procedure and simulation results for a 10-GHz aperiodic Bragg resonator. Finally, Section V describes the measurements results from a 10-GHz aperiodic Bragg resonator.

## II. RESONATOR MODELING AND DESIGN

The model described in the following sections represents a cylindrical resonator structure, although the equations



Fig. 2. A square-layered alumina periodic Bragg resonator. The sidewalls and end walls are constructed from copper-coated printed circuit board. Metal pins were inserted through the sidewalls to support the dielectric plates.

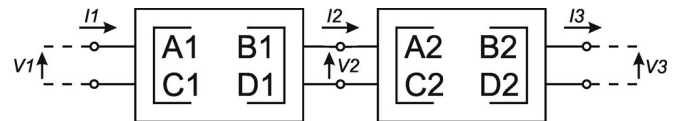


Fig. 3. A cascade connection of two 2-port ABCD matrices.

could easily be modified to represent a rectangular structure. A cylindrical structure was chosen because it offers a simple mechanical construction and lower loss. The cavity has been designed to operate using the  $TE_{011}$  mode at 10 GHz. This is the mode typically chosen for high-Q cavities because it exhibits a low inherent loss [13]. It is possible to obtain an increase in Q by designing the cavity to operate using a higher order mode, such as  $TE_{012}$ , but this has the disadvantage of increasing the cavity volume.

In our model, each air and dielectric section of the Bragg structure is considered to be a separate waveguide, which we represent using a 2-port network. These 2 port networks are then cascaded to form the complete Bragg resonator. The ABCD parameter set is used to describe the 2 port networks because the series cascade connection of these networks reduces to a simple matrix multiplication. Fig. 3 illustrates the cascade connection of a pair of 2 port networks represented using ABCD parameters. The directions of the port voltages and currents are also shown.

The resulting matrix equation for the cascade connection illustrated by Fig. 3 is

$$\begin{bmatrix} V_1 \\ I_1 \end{bmatrix} = \begin{bmatrix} A_1 & B_1 \\ C_1 & D_1 \end{bmatrix} \begin{bmatrix} A_2 & B_2 \\ C_2 & D_2 \end{bmatrix} \begin{bmatrix} V_3 \\ I_3 \end{bmatrix}. \quad (1)$$

The ABCD matrix must now be defined for each section of the resonator. The ABCD matrix for a lossy transmission line of length  $l$  meters with complex propagation constant  $\gamma$  and characteristic impedance  $Z_0$  is

$$\begin{bmatrix} V_1 \\ I_1 \end{bmatrix} = \begin{bmatrix} \cosh \gamma l & Z_0 \sinh \gamma l \\ \frac{1}{Z_0} \sinh \gamma l & \cosh \gamma l \end{bmatrix} \begin{bmatrix} V_2 \\ I_2 \end{bmatrix}. \quad (2)$$

To represent each section of the resonator correctly using this equation, it is necessary to calculate the complex propagation constant and wave impedance for each reflector section. These calculations are performed assuming the wave is traveling in a cylindrical waveguide. The complex propagation constant  $\gamma$  is defined by

$$\gamma = \alpha + j\beta, \quad (3)$$

where  $\alpha$  is the attenuation coefficient measured in units of nepers per meter and  $\beta$  is the phase constant.

The phase constant for the dielectric and air sections can be calculated from

$$\beta = \sqrt{\omega^2 \mu \varepsilon - \left( \frac{\chi'_{mn}}{a} \right)^2}, \quad (4)$$

where  $\varepsilon$  is the permittivity of the material filling the guide,  $\omega$  is the angular frequency, and  $a$  is the cavity radius;  $\chi'_{mn}$  represents the  $n$ th zero of the derivative of the Bessel function of the first kind of order  $m$ . In the case of the TE<sub>01</sub> mode, the value of  $\chi'_{mn} \approx 3.8318$ .

#### A. Air Sections

The only loss in the air-filled sections of the guide is a result of the conductive sidewalls. This can be calculated using the perturbation method as described in [14], and the resulting equation is shown in (5). This equation represents the attenuation coefficient, in units of Npm<sup>-1</sup>, for a transverse electric (TE) mode with circumferential mode number  $m$  and radial mode number  $n$  in a cylindrical waveguide of radius  $a$  operating at frequency  $f$ :

$$(\alpha_c)_{mn}^{\text{TE}_z} = \frac{R_s}{a\eta \sqrt{1 - \left( \frac{f_c}{f} \right)^2}} \left[ \left( \frac{f_c}{f} \right)^2 + \frac{m^2}{(\chi'_{mn})^2 - m^2} \right], \quad (5)$$

where  $\eta$ , given by (6), is the wave impedance for a plane wave inside an unbounded infinite medium with permittivity  $\varepsilon$  and permeability  $\mu$ :

$$\eta = \sqrt{\frac{\mu}{\varepsilon}}. \quad (6)$$

The surface loss resistance of the guide walls is represented by  $R_s$ , and this is a function of the wall conductivity  $\sigma$ . The value of  $R_s$  can be calculated using

$$R_s = \sqrt{\frac{\omega \mu}{2\sigma}}. \quad (7)$$

The lower cut of frequency of the guide is given by  $f_c$ , and its value can be calculated using

$$f_c = \frac{\chi'_{mn}}{2\pi a \sqrt{\mu \varepsilon}}. \quad (8)$$

The only remaining term required to describe the ABCD matrix for the air-filled sections is the guide wave impedance  $Z_0$ . This can be calculated for a transverse electric mode using

$$Z_{\text{TE}} = \frac{\eta}{\sqrt{1 - \left( \frac{f_c}{f} \right)^2}}. \quad (9)$$

#### B. Dielectric Sections

The total loss in the dielectric sections,  $\alpha_t$ , can be considered as the sum of the sidewall conducting loss,  $\alpha_c$ , and the dielectric losses,  $\alpha_d$ :

$$\alpha_t = \alpha_c + \alpha_d. \quad (10)$$

The conductive sidewall losses can be calculated using (5), but the loss in the dielectric must be treated differently. The attenuation due to the lossy dielectric,  $\alpha_d$ , can be calculated from the complex propagation constant as shown in [15]. If the loss is small, then the phase constant in the dielectric section can be assumed to be constant. The attenuation due to dielectric loss is given by (11)

$$\alpha_d = \frac{\omega^2 \mu \varepsilon \tan \delta}{2\sqrt{\omega^2 \mu \varepsilon - \left( \frac{\chi'_{mn}}{a} \right)^2}}, \quad (11)$$

where  $\tan \delta$  is the loss tangent of the dielectric and  $\varepsilon$  is the relative permittivity of the dielectric.

#### C. Metal End Walls

The loss in the metal end walls of the cavity can be approximated by considering the complex propagation constant,  $\gamma$ , and intrinsic wave impedance,  $\eta$ , for a plane wave in a good conductor. As is described in [16], the complex propagation constant inside a good conductor can be approximated by

$$\gamma = j\omega \sqrt{\mu \varepsilon} \sqrt{\frac{\sigma}{j\omega \varepsilon}}. \quad (12)$$

This can be manipulated into the form

$$\gamma = (1 + j) \sqrt{\frac{\omega \mu \sigma}{2}}. \quad (13)$$

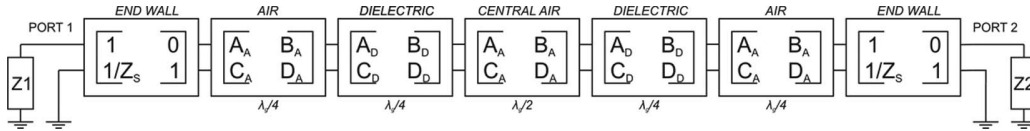


Fig. 4. A waveguide ABCD parameter model for a 2-plate Bragg resonator. The air and dielectric plate reflector thicknesses of this structure are all  $\lambda_g/4$  in length.

TABLE I. PERIODIC BRAGG RESONATOR SIMULATION PARAMETERS.

Parameter	Value
Dielectric section length	2.41 mm
Air section length	7.87 mm
Central section length	15.73 mm
Dielectric permittivity	9.75
Dielectric loss tangent	$1 \times 10^{-5}$
Cavity radius	60 mm
Wall conductivity	$6.1 \times 10^{-7} \text{ Sm}^{-1}$

TABLE II. THE SIMULATED UNLOADED QUALITY FACTOR FOR PERIODIC BRAGG RESONATORS WITH VARYING NUMBERS OF DIELECTRIC PLATES.

Number of dielectric plates	Unloaded quality factor ( $Q_0$ )
2	125785
4	289854
6	322579
8	327867
10	327867

The intrinsic wave impedance,  $\eta$ , for a plane wave in a general lossy medium is given by

$$\eta = \frac{j\omega\mu}{\gamma}. \quad (14)$$

If we substitute (13) into (14), then after several manipulations, we can write

$$\eta = Z_s = (1 + j)\sqrt{\frac{\omega\mu}{2\sigma}}. \quad (15)$$

Eq. (15) describes the wave impedance inside a good conductor. It can be seen that the real and imaginary parts of (15) can be modeled as an impedance consisting of a series connected resistance and inductance. In terms of ABCD parameters, this can be written as

$$\begin{bmatrix} V_1 \\ I_1 \end{bmatrix} = \begin{bmatrix} 1 & 0 \\ 1/Z_s & 1 \end{bmatrix} \begin{bmatrix} V_2 \\ I_2 \end{bmatrix}. \quad (16)$$

Using (2) to (15), it is now possible to characterize a dielectric, air, and metal end-wall section of the Bragg resonator entirely in terms of its ABCD parameters. This model offers several advantages when compared with a full-field simulation. It is possible to model a Bragg resonator with any number of dielectric and air sections of arbitrary lengths. The computation requirements are minimal, and the resonant frequency and quality factor for a given mode can be extracted very rapidly using standard circuit simulation techniques. One disadvantage of the model is that it considers each mode in isolation, and therefore, to calculate the resonant frequencies of other modes, additional simulations are required.

### III. PERIODIC RESONATOR SIMULATION

An S-Parameter simulation of a microwave periodic Bragg resonator has been performed using the model described in the previous section. The cavity radius was assumed to be 60 mm, and the lengths of the air and dielectric reflector sections were set to one-quarter of the guide wavelength ( $\lambda_g/4$ ) for a  $\text{TE}_{01}$  mode at 10 GHz. The value of the guide wavelength was calculated using

$$\lambda_g = \frac{2\pi}{\beta}, \quad (17)$$

where  $\beta$  is the phase constant for the  $\text{TE}_{mn}$  mode of interest, which can be calculated using (4).

A block diagram of the simulation structure for a 2-plate resonator is shown in Fig. 4. The value of the end-wall impedances was calculated using (15). The value of the port impedances  $Z_1$  and  $Z_2$  were set large enough such that value of the end-wall termination was not reduced. This enabled the unloaded quality factor,  $Q_0$ , to be simulated. A summary of the parameters used in the simulation is shown in Table I.

In a periodic Bragg resonator, the  $Q$ -factor will begin to saturate as the number of dielectric plates is increased. This saturation is a result of the exponential decay of the electric field as the cavity end walls are approached [3]. To ascertain the maximum  $Q$  obtainable from a periodic Bragg resonator, several simulations were performed with our dielectric using increasing numbers of dielectric plates. The results are shown in Table II.

It can be seen from the results in Table II that the unloaded quality factor begins to saturate when more than 6 plates are used. The quality factor of the periodic Bragg design could be further improved by increasing the cavity radius to reduce the wall loss. However, this has the undesirable effect of increasing the number of spurious modes.

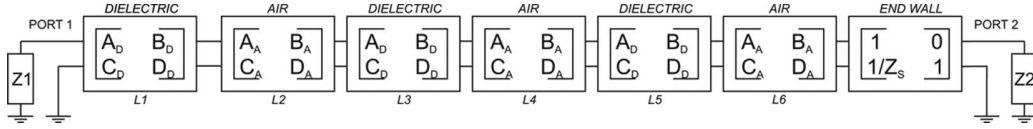


Fig. 5. A waveguide ABCD parameter model for half of a 6-plate Bragg resonator. The air and dielectric plate thicknesses of this structure are optimized to maximize the magnitude of the input reflection coefficient ( $S_{11}$ ).

TABLE III. DIELECTRIC AND AIR SECTION REFLECTOR THICKNESSES FOR AN OPTIMIZED 6-PLATE BRAGG RESONATOR.

Section identifier	Material	Length (mm)
L1	Dielectric	1.512
L2	Air	11.023
L3	Dielectric	1.887
L4	Air	9.300
L5	Dielectric	2.253
L6	Air	8.060
LC	Air	17.033

#### IV. APERIODIC RESONATOR SIMULATION

Breeze *et al.* [10] have demonstrated that a significant improvement in the quality factor of a Bragg resonator can be achieved by using an aperiodic plate arrangement to redistribute the energy inside the cavity into the lower loss air sections. To ascertain the reflector thicknesses required for maximum Q in our resonator, a numerical optimization procedure was adopted.

In this new model, only half of the Bragg resonator is considered because the structure is symmetrical. The structure to be simulated is illustrated in Fig. 5. The value of the port impedance,  $Z_1$ , was set equal to the wave impedance inside an air section. This ensures that we are representing a wave traveling from the central air region toward a dielectric plate. The value of terminating impedance,  $Z_2$ , is less critical due to the small impedance to ground presented by the end wall. However, its value must be large enough to avoid reducing the end-wall impedance.

The air and dielectric section thicknesses were initially set to the values used in the periodic design as shown in Table I. The reflector section lengths were then optimized until the magnitude of the input reflection coefficient at port one ( $S_{11}$ ) reached a maximum. Table III illustrates the optimal air and dielectric section thicknesses for a 6-plate resonator.

When an optimal set of plate thicknesses was found, 2 half-resonators were combined, and then the central air section was reintroduced. The final stage of the optimization required that length of the central resonant region be adjusted to restore the desired resonance to the correct frequency. This was achieved by calculating the additional phase shift required to restore the phase of the input reflection coefficient to  $180^\circ$  using

$$\delta_d = 180^\circ - \angle S_{11}. \quad (18)$$

The additional length that needs to be added to the central section,  $\delta_L$ , was then calculated using

$$\delta_L = \frac{\lambda_g \delta_d}{360}. \quad (19)$$

A simulation of the complete Bragg structure was then performed. Using this optimization algorithm, it has been possible to design a cavity with a simulated unloaded quality factor of 400 000 at 10 GHz. This is a 24% improvement when compared with the equivalent periodic Bragg resonator.

To ascertain how the optimization procedure had redistributed the energy inside the cavity, the voltage standing wave patterns were plotted for the 6 plate periodic and aperiodic resonators. Each waveguide section was subdivided into  $n$  smaller sections with the same constituent parameters but a reduced length. An ABCD matrix was generated for each of these subsections using

$$\begin{bmatrix} V_1 \\ I_1 \end{bmatrix} = \begin{bmatrix} \cosh\left(\frac{\gamma l}{n}\right) & Z_0 \sinh\left(\frac{\gamma l}{n}\right) \\ \frac{1}{Z_0} \sinh\left(\frac{\gamma l}{n}\right) & \cosh\left(\frac{\gamma l}{n}\right) \end{bmatrix} \begin{bmatrix} V_2 \\ I_2 \end{bmatrix}. \quad (20)$$

The reduced-length sections were then combined to form the original resonator. This enabled the voltage distribution to be extracted by calculating the voltages at the nodes connecting the smaller subsections.

The voltage standing wave distribution inside the 10-GHz periodic Bragg resonator is shown in Fig. 6. The vertical lines indicate the locations of the edges of the dielectric plates. It can be seen in Fig. 6 that the voltage peaks occur inside the dielectric plates. The voltage standing wave distribution inside the aperiodic Bragg resonator is shown in Fig. 7. If we compare these figures, it can be seen that the voltage peaks in the aperiodic resonator occur in the lower loss air sections outside of the dielectric plates.

#### V. CURRENT RESULTS

Using the model and simulation results described in the previous section, a cylindrical Bragg resonator has been constructed that uses an aperiodic arrangement of alumina plates.

The resonator has been designed to operate using the  $TE_{011}$  low loss mode with a resonant frequency of 10 GHz. A cross-sectional view of the cavity is shown in Fig. 8. This initial design consists of 6 dielectric plates mounted in an aluminum shield. Wire loop probes were used to

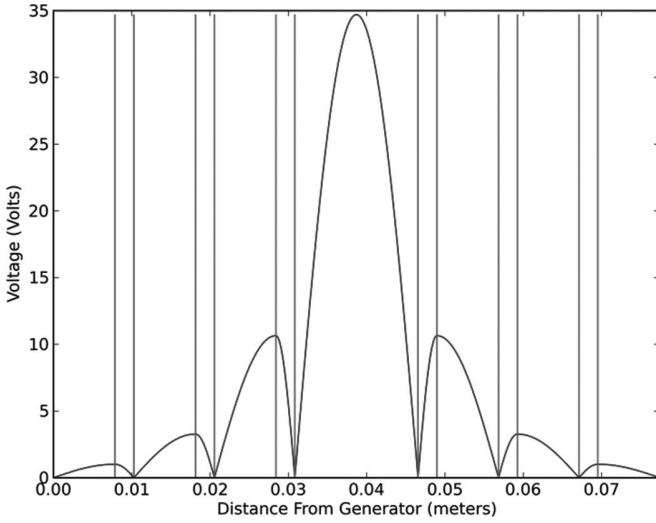


Fig. 6. Voltage standing wave distribution inside the periodic Bragg resonator.

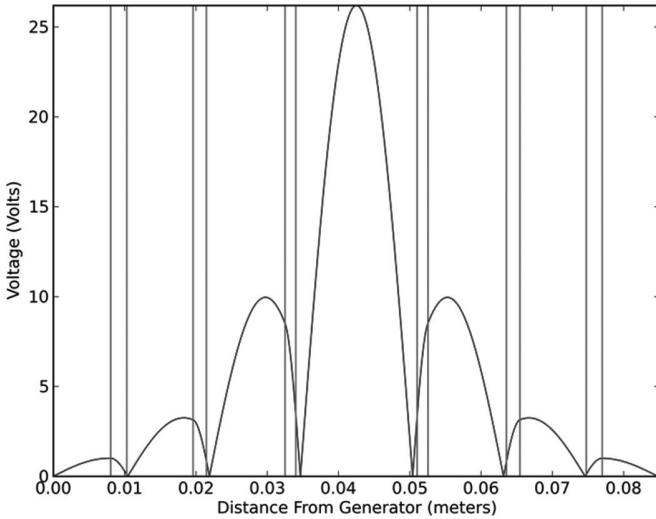


Fig. 7. Voltage standing wave distribution inside the aperiodic Bragg resonator.

couple energy into the cavity. Fig. 9 shows a photo of the central air-filled resonant section and the wire loop coupling probes.

A plot of the forward transmission coefficient scattering parameter ( $S_{21}$ ) is shown in Fig. 10. The wanted resonance can be seen at the center of this plot. Several spurious modes are also clearly visible. A narrow band plot of the wanted resonance is shown in Fig. 11. It can be seen that the resonator has a center frequency of 9.94 GHz with a loaded quality factor  $Q_L$  of 126810 and an insertion loss  $S_{21}$  of  $-8.98$  dB. If we assume equal input and output coupling, then the unloaded quality factor  $Q_0$  can be calculated using

$$Q_0 = \frac{Q_L}{(1 - S_{21})}, \quad (21)$$

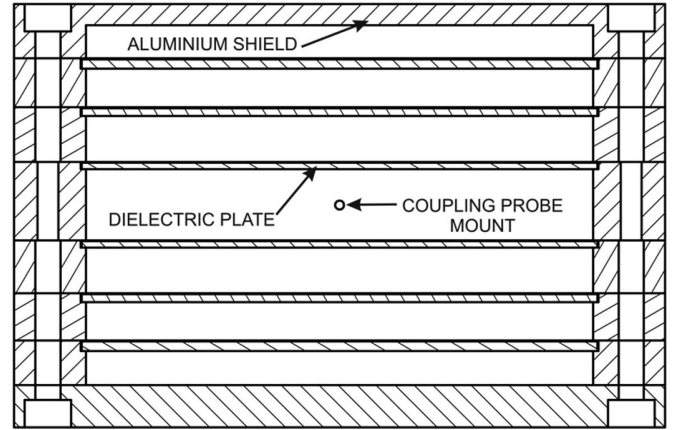


Fig. 8. A cross-section view of the 6-plate aperiodic Bragg resonator.

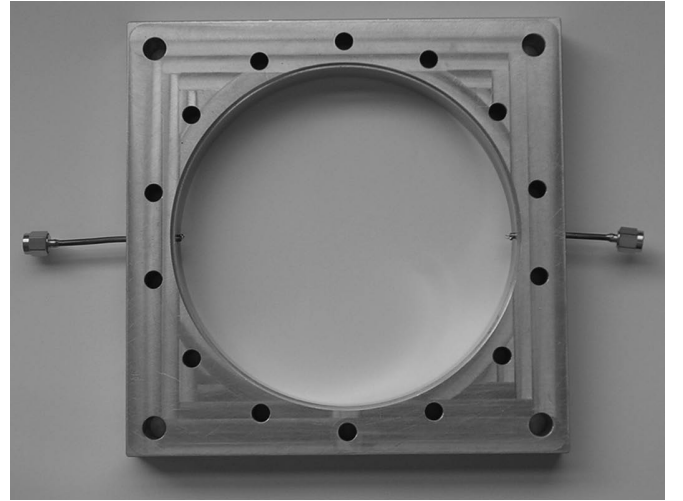


Fig. 9. Aperiodic Bragg resonator, central air-filled section.

where  $Q_L$  is the loaded quality factor and  $S_{21}$  is the insertion loss as a voltage ratio. Substituting the values above gives an unloaded quality factor  $Q_0$  of 196797.

## VI. CONCLUSIONS

The resonant frequency of 9.94 GHz is in good agreement with the simulated result of 10 GHz. It can be seen in Fig. 10 that there are no spurious resonances within  $\pm 50$  MHz of the wanted resonance. The closest low-loss unwanted mode is approximately 50 MHz lower than the wanted resonance; other low-loss modes can also be seen 200 MHz higher in frequency. It is still possible to use this resonator in an oscillator, possibly with the inclusion of a lower Q broadband filter if required. This resonator may also find application as a discriminator for noise detection and reduction and in high-Q filters.

The unloaded quality factor of 196797 is considerably lower than the simulated value of 400000. The increased loss in the resonator is thought to be due to an increase

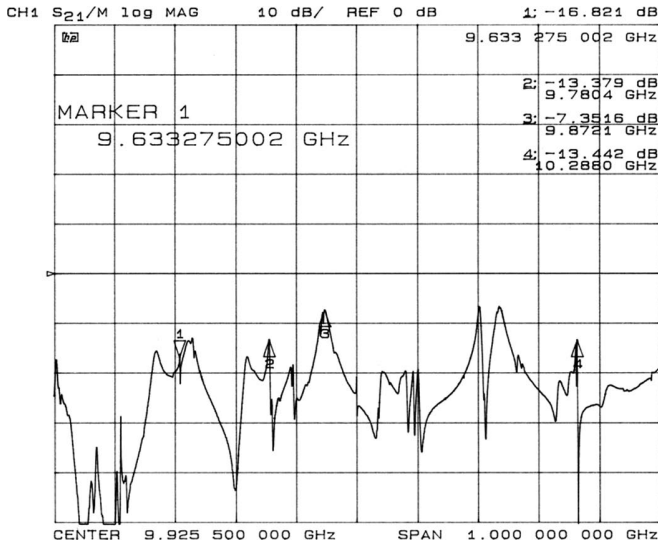


Fig. 10. A plot of the forward transmission coefficient ( $S_{21}$ ) for the 6-plate aperiodic Bragg resonator. A frequency span of 1 GHz is shown.

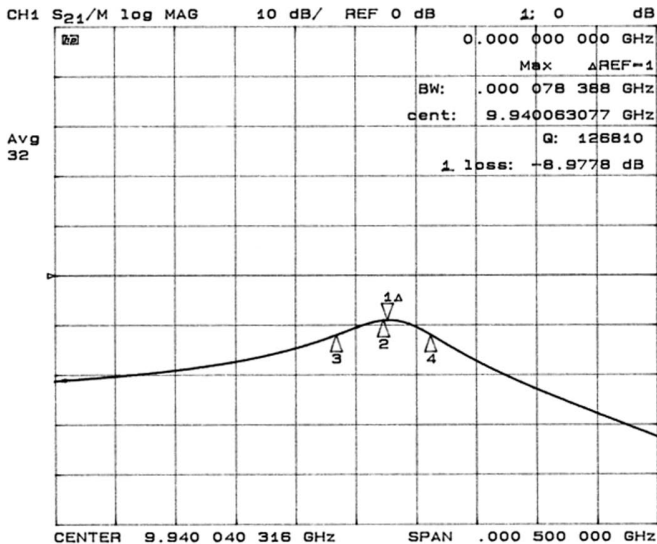


Fig. 11. A plot of the forward transmission coefficient ( $S_{21}$ ) for the 6-plate aperiodic Bragg resonator. A frequency span of 500 kHz is shown.

in wall losses resulting from the poor conductivity of the resonator shield and to an increase in the loss tangent of the alumina plates and the introduction of discontinuities as a result of the structures required to support the dielectric plates.

#### ACKNOWLEDGMENTS

We would also like to thank Professor N. McN. Alford and J. Breeze for helpful discussions regarding aperiodic Bragg resonators.

#### REFERENCES

- [1] C. McNeilage, J. H. Searls, E. N. Ivanov, P. R. Stockwell, D. M. Green, and M. Mossamaparast, "A review of sapphire whispering

- gallery-mode oscillators including technical progress and future potential of the technology," in *Proc. IEEE Frequency Control Symp.*, Montreal, QC, Canada, Aug. 2004, pp. 210–218.
- [2] M. E. Tobar, J. Krupka, E. N. Ivanov, and R. A. Woode, "Anisotropic complex permittivity measurements of mono-crystalline rutile between 10 and 300 K," *J. Appl. Phys.*, vol. 83, no. 3, 1998.
- [3] C. A. Flory and R. C. Taber, "High performance distributed Bragg reflector microwave resonator," *IEEE Trans. Ultrason. Ferroelectr. Freq. Control*, vol. 44, no. 2, pp. 486–495, Mar. 1997.
- [4] C. A. Flory and H. L. Ko, "Microwave oscillators incorporating high performance distributed Bragg reflector microwave resonators," *IEEE Trans. Ultrason. Ferroelectr. Freq. Control*, vol. 45, no. 3, pp. 824–829, May 1998.
- [5] C. J. Maggiore, A. M. Clogston, G. Spalek, W. C. Sailor, and F. M. Mueller, "Low-loss microwave cavity using layered dielectric materials," *Appl. Phys. Lett.*, vol. 64, no. 11, pp. 1451–1453, 1994.
- [6] J. Krupka, A. Cwikla, M. Mrozowski, R. N. Clarke, and M. E. Tobar, "High Q-factor microwave Fabry-Perot resonator with distributed Bragg reflectors," *IEEE Trans. Ultrason. Ferroelectr. Freq. Control*, vol. 52, no. 9, pp. 1443–1451, Sep. 2005.
- [7] M. E. Tobar, J. L. le Floch, D. Cros, J. Krupka, J. D. Anstie, and J. G. Hartnett, "Spherical Bragg reflector resonators," *IEEE Trans. Ultrason. Ferroelectr. Freq. Control*, vol. 51, no. 9, pp. 1054–1059, Sep. 2004.
- [8] J. Krupka, M. E. Tobar, J. G. Hartnett, D. Cros, and J. M. le Floch, "Extremely high-Q factor dielectric resonators for millimeter-wave applications," *IEEE Trans. Microw. Theory Tech.*, vol. 53, no. 2, pp. 702–712, 2005.
- [9] J. Mills, "Design and simulation of novel high Q dielectric resonators," M.Eng. thesis, York Univ., York, UK, 1999.
- [10] J. Breeze, J. Krupka, and N. M. Alford, "Enhanced quality factors in aperiodic reflector resonators," *Appl. Phys. Lett.*, vol. 91, no. 15, 2007.
- [11] J. M. le Floch, M. E. Tobar, D. Cros, and J. Krupka, "High Q-factor distributed bragg reflector resonators with reflectors of arbitrary thickness," *IEEE Trans. Ultrason. Ferroelectr. Freq. Control*, vol. 54, no. 12, pp. 2689–2695, Dec. 2007.
- [12] S. Bale and J. Everard, "High Q X-band distributed Bragg resonator utilising an aperiodic alumina plate arrangement," presented at the EFCS-IFTF 2009 Joint Conf., Besancon, France, 2009.
- [13] D. M. Pozar, *Microwave Engineering*, 3rd ed. New York: Wiley, 2005, pp. 284–287.
- [14] C. A. Balanis, *Advanced Engineering Electromagnetics*. New York: Wiley, 1989, pp. 485–488.
- [15] D. M. Pozar, *Microwave Engineering*, 3rd ed. New York: Wiley, 2005, pp. 97–98.
- [16] D. M. Pozar, *Microwave Engineering*, 3rd ed. New York: Wiley, 2005, pp. 18–19.



**Simon J. Bale** was born in Blackpool, UK, in 1981. He obtained his M.Eng. degree in electronics from the University of York, York, UK, in 2004. He is currently studying for his Ph.D. in RF and microwave electronics at the University of York where he is working on high-Q microwave resonators and ultra-low-phase noise oscillators.



**Jeremy K. A. Everard** (M'90) obtained his B.Sc.Eng. degree from the University of London (King's College), London, UK, in 1976, and his Ph.D. degree from the University of Cambridge, Cambridge, UK, in 1983.

He worked in industry for 6 years at the GEC Marconi Research Laboratories, Great Baddow, Chelmsford, UK; M/A-Com, Dunstable, UK; and Philips Research Laboratories, Redhill, UK, on radio and microwave circuit design. At Philips he ran the Radio Transmitter Project Group.

Dr. Everard then taught RF and microwave circuit design, optoelectronics, and electromagnetism at King's College London for 9 years

while leading the Physical Electronics Research Group. He became University of London Reader in Electronics at King's College London in 1990 and Professor of Electronics at the University of York, York, UK, in September 1993. In September 2007, he was awarded a five-year research chair in low-phase noise signal generation sponsored by BAE Systems and the Royal Academy of Engineering.

In the RF/microwave area, his research interests include the theory and design of low-noise oscillators using inductor capacitor (LC); surface acoustic wave (SAW); crystal, dielectric, transmission line, helical, and superconducting resonators; flicker noise measurement and reduction in amplifiers and oscillators; high-efficiency broadband amplifiers; high Q printed filters with low radiation loss; broadband negative group delay circuits; and monolithic microwave integrated circuit implementations.

His research interests in optoelectronics include all optical self-routing switches that route data-modulated laser beams according to the destination address encoded within the data signal; ultra-fast three-wave optoelectronic detectors, mixers, and phase-locked loops; distributed fiber optic sensors; and terahertz transmitters and receivers.

Dr. Everard has published papers on oscillators, amplifiers, resonators and filters, all optical switching, optical components, optical fiber sensors, and mm-wave optoelectronic devices and the book *Fundamentals of RF Circuit Design with Low Noise Oscillators* (Wiley). He has coedited and coauthored the book *GaAs Technology and its Impact on Circuits and Systems* (IEE), and he has contributed to a book on optical fiber sensors. He has filed patent applications in many of these areas. Dr. Everard is a member of the Institution of Electrical Engineers (IET), London, UK.

# Cross Correlation Residual Phase Noise Measurements using Two HP3048A Systems and a PC Based Dual Channel FFT Spectrum Analyser

24th European Frequency and Time Forum  
13-16 April 2010

Simon J. Bale<sup>(1)</sup>, David Adamson<sup>(2)</sup>, Brett Wakley<sup>(1)</sup>, Jeremy Everard<sup>(1)</sup>

(1) Department of Electronics  
University of York  
Heslington  
York, UK  
Email: [sjb508@ohm.york.ac.uk](mailto:sjb508@ohm.york.ac.uk)

(2) Formerly at the National Physical Laboratory  
Hampton Road  
Teddington  
Middlesex, UK  
Email: [david@adamsonadventures.co.uk](mailto:david@adamsonadventures.co.uk)

## ABSTRACT

This paper describes a cross correlation residual phase noise measurement system based on two HP3048A systems and a dual channel FFT spectrum analyser consisting of a PC card containing two 16bit (125MS/Sec) A to D converters. A measurement system noise floor of -200 dBc/Hz is achieved for 100,000 correlations. Residual phase noise measurements are also performed on low noise L-Band microwave amplifiers, developed at York. The key features of the cross correlation technique and the different window functions required during measurement are discussed.

## INTRODUCTION

Residual noise can be described as the noise added to a signal when it's processed by a two port network. It consists of both AM and PM components but in this paper we will primarily be dealing with the measurement of the PM component. A conventional residual phase noise measurement system is illustrated in Fig. 1. A low noise sinusoidal signal source is used to provide a reference signal at the input to the measurement system. This signal is then split into two separate paths that provide the drive signals to a phase detector which is typically a double balanced mixer. It is assumed that the source phase noise is correlated at the inputs to the phase detector and therefore cancels. A phase shifter is used to adjust the delay in one of the paths such that the signals mix in quadrature. This is the point at which a mixer is most sensitive to any phase fluctuations between its input signals. Finally, the output of the mixer is low pass filtered to remove any unwanted RF components before being amplified and fed to an FFT analyser. The FFT analyser then plots the spectral density of the phase noise at the output of the mixer.

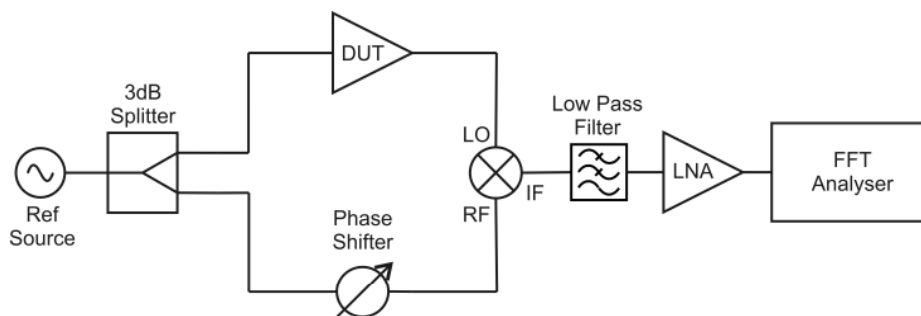


Fig. 1. Simplified single channel residual phase noise measurement system.

The noise floor of a system utilising this single channel measurement technique is highly dependent on and limited by the noise floors of the mixer, filters and low noise amplifier (LNA)[1]. This type of system can have a residual phase noise floor in the region of -180 dBc/Hz at high offset frequencies[2].

## THE CROSS CORRELATION TECHNIQUE

The cross correlation technique can be used to suppress the mixer, filter and baseband LNA noise from the measurement results [1]. Using this method the uncorrelated noise in each channel can be suppressed by a factor of  $\sqrt{N}$ , where  $N$  is the number of cross correlations. In this type of system two independent channels are used and their outputs are fed to a cross spectrum analyser. Fig. 2 shows the simplified diagram of a cross correlation residual phase noise measurement system.

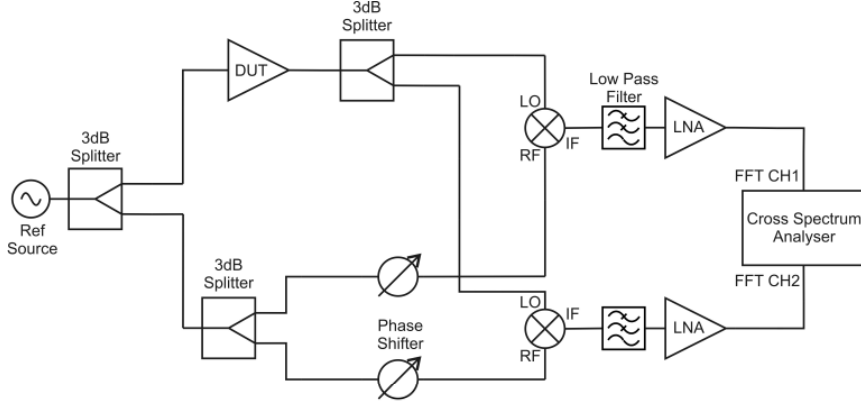


Fig. 2. Simplified cross correlation residual phase noise measurement system.

It can be seen that the reference signal is split into two paths, the first passes through the device under test (DUT). The signal at the output of the DUT is then split again where it provides the LO inputs to a pair of mixers. The second path from the reference source also passes through a 3 dB splitter whose outputs are used to provide the additional quadrature signals required to drive the mixers. This arrangement ensures that the noise added by the DUT is correlated in both channels while the noise generated by the mixers, filters and LNA remains un-correlated.

As described by Rubiola in[3], the noise present at the output of each mixer can be modelled using two noisy signals as shown in (1) and (2).

$$x(t) = a(t) + c(t) \xrightarrow{FFT} X(f) = A(f) + C(f) \quad (1)$$

$$y(t) = b(t) + c(t) \xrightarrow{FFT} Y(f) = B(f) + C(f) \quad (2)$$

Where  $a(t)$  and  $b(t)$  represent the uncorrelated instrument noise present in each channel and  $c(t)$  represents the correlated DUT noise. Taking the cross spectrum of these two signals and average over  $N$  samples we can write:

$$\overline{S_{XY}} = \frac{1}{N} \sum_{n=1}^{n=N} [X_n \times Y_n^*] \quad (3)$$

Where  $n$  represents the sample index and  $*$  implies the conjugate. If we then substitute (1) and (2) into (3) we can write:

$$\overline{S_{XY}} = \frac{1}{N} \sum_{n=1}^{n=N} [(A_n + C_n) \times (B_n + C_n)^*] \quad (4)$$

After multiplying out the brackets we can write (5):

$$\overline{S_{XY}} = \frac{1}{N} \sum_{n=1}^{n=N} [(A_n B_n^*) + (A_n C_n^*) + (C_n B_n^*) + (C_n C_n^*)] \quad (5)$$

If we assume that there is no correlation between the noisy signals  $a(t)$ ,  $b(t)$  or  $c(t)$  then as the number of averages increases the uncorrelated terms in the cross spectrum -  $AB$ ,  $AC$  and  $CB$  will all approach zero. The only remaining term,  $CC$ , represents the power spectral density of the correlated DUT noise.

## MEASUREMENT SYSTEM

The main components of our measurement system are two HP 11848A phase noise test sets. These form part of the HP 3048A phase noise measurement system and they integrate a phase detector, LNA, PLL and several stages of filtering into a single unit. They exhibit a low single channel noise floor of below  $-180$  dBc/Hz at carrier offsets greater than 10 kHz[2]. They are also fully computer controllable using Visual Basic software developed at the UK National Physical Laboratory (NPL) by David Adamson - (Co-Author).

A dual channel high speed data capture card with a 16 bit resolution and maximum sampling rate of 125 MSamples/Sec is used to capture the noise output from the 11848A units. A software based cross spectrum analyser has also been developed using the Java programming language. This fully multi-threaded software allows spectrum auto-correlation and cross-correlation as well as the application of multiple time domain windows to the sampled data. A block diagram of the complete measurement, including calibration components, is shown in Fig. 3. The components integrated into the HP 11848A units are shown enclosed inside the red dashed rectangles.

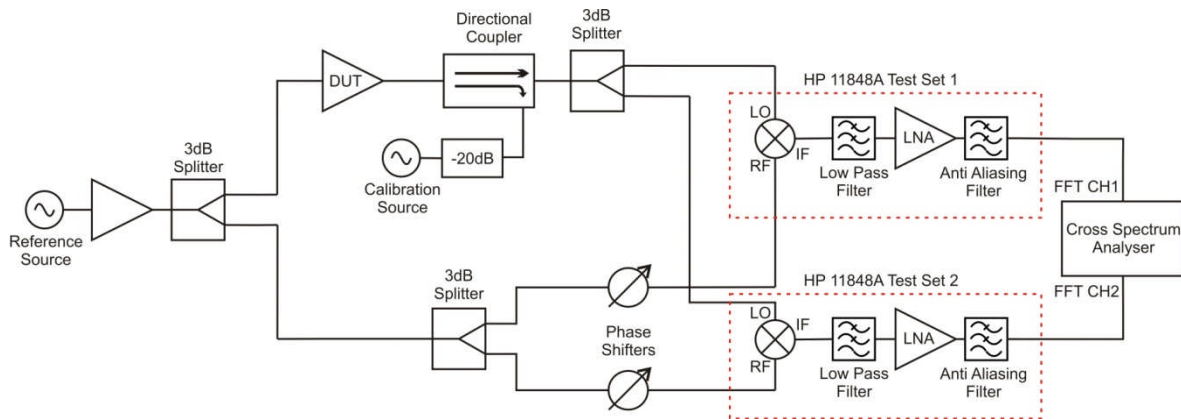


Fig. 3. Cross correlation residual phase noise measurement system including calibration components.

The reference source is provided by a battery powered ultra low phase noise dielectric resonator oscillator (DRO) developed at York. This oscillator exhibits PM and AM noise levels of less than  $-173$  dBc/Hz at carrier offset greater than 10 kHz. Its low level of AM noise is particularly beneficial when making sensitive phase noise measurements. This is because a typical saturated double balance microwave usually only offers around 20dB to 30dB of AM noise suppression[4]. Once this has been exhausted the source AM noise will directly add to the residual phase noise and corrupt the measurement results. A power amplifier is connected to the output of the reference oscillator to increase the signal level to a value large enough to saturate the mixers. Finally, a selection high quality, double shielded, microwave cables were using to interconnect the various components.

## Calibration

Calibration is achieved by injecting a tone into the measurements system via the directional coupler connected to the output of the DUT. With reference to Fig. 3, it can be seen that the calibration tone will appear as a spur at the output of each mixer. The spur frequency and carrier to spur amplitude ratio at the output of the directional coupler are noted and then the level of the calibration spur at the mixer outputs is measured using the cross spectrum analyser.

The accuracy of the calibration and resulting phase noise measurements is, in part, limited by the accuracy achieved during the measurement of the calibration spur. In order to minimise the high side lobe levels that will be present in a un-windowed spectrum we must apply a window function to the time domain data before transformation into the frequency domain.

For calibration purposes the amplitude accuracy of the calibration spur measurement is the most important factor. The Flat Top window, is an ideal candidate for this measurement. Time domain and frequency domain plots for this window function are shown in Fig. 4.

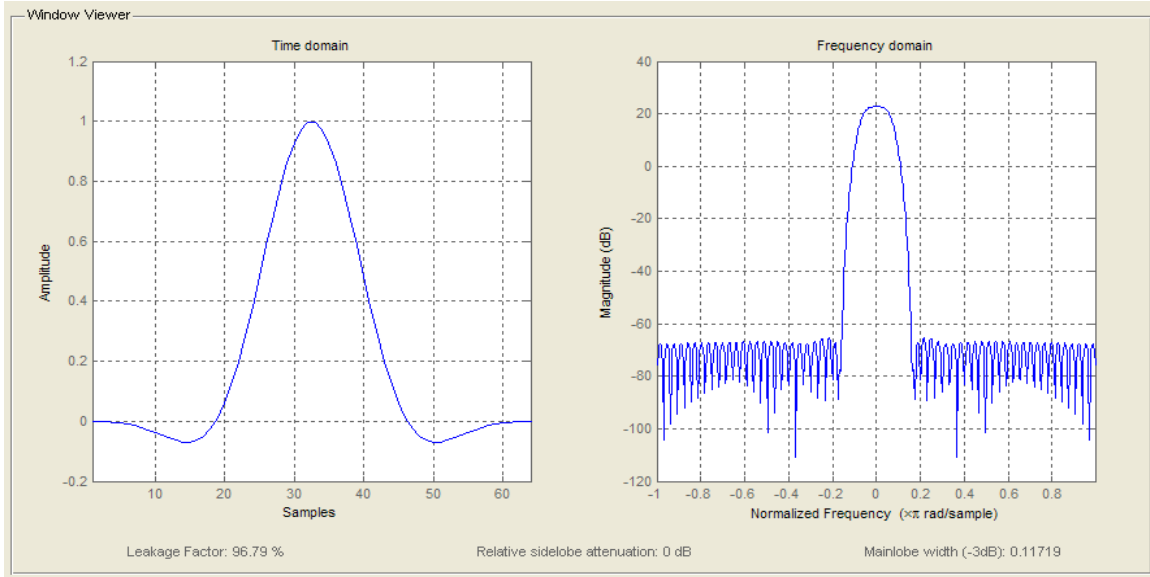


Fig. 4: Time domain (left) and frequency domain (right) plots of the flat top window function. Created using the Matlab Window Visualisation Tool.

When the calibration measurements have been completed the tone is removed and the coupled port of the directional coupler is terminated in  $50 \Omega$ . The measured noise can then be converted to single sideband phase noise,  $L(f)$ , using (6).

$$L(f) = S_{\phi} + K_1 - K_2 - 6 \quad (6)$$

Where  $S_{\phi}$  is the double side band phase noise spectral density,  $K_1$  is the carrier to sideband spur ratio and  $K_2$  is the amplitude of the calibration spur - all parameters are in decibels. The subtraction of an additional 6 dB is necessary in order to account for the fact that we are measuring double side band phase noise at the output of the mixers. The primary advantage of calibrating the instrument in this way is that the calibration is performed under the actual measurement conditions with the DUT in place. It should also be noted that ideally a calibration spur should be injected at every measurement frequency of interest; however, the frequency response of the HP11848A units is sufficiently flat this is not necessary.

In order to check the validity of the calibration a second independent calibration technique was used. This was developed by Dr. Bob Longstone at BAE Systems. The DUT was initially replaced with the series connection of a 44 dB attenuator and a 44 dB amplifier. This arrangement artificially increases the system noise floor to a value that can be calculated using (7) :

$$L(f) = -177 + N_A - P_i \quad (7)$$

Where  $N_A$  is the noise figure of the combined amplifier and attenuator and  $P_i$  is the power available at the input to the attenuator. If we substitute in the combined noise figure of 48.5 dB and an input power of 20 dBm then the theoretical phase noise floor can be calculated to be -148.5 dBc/Hz at offsets above the flicker noise corner. The measured noise floor was -148.4 dBc/Hz which is in good agreement with the theory.

## SYSTEM NOISE FLOOR

The system noise floor is measured by removing the DUT from the equipment setup shown in Fig. 3 and replacing it with a straight through connection. The phase shifters were adjusted so that DC level at the output of each mixer was at a minimum. In order that the source phase noise did not de-correlate at large offset frequencies the group delay of each

channel was measured to ensure that the phase shift between the mixer input ports was only  $90^\circ$  and not a multiple of  $360^\circ + 90^\circ$ . The measurement was performed at a frequency of 1.25 GHz with mixer LO and RF port input powers of 16.1 dBm and 16.9 dBm respectively. The use of high power levels ensures that the mixers are truly saturated and minimises the signal channel noise floor of each HP 11848A unit. The signal processing was performed at a sampling rate of 2 MSamples/Sec with a data frame length of 262,144 points. This equated to a resolution bandwidth of 7.63 Hz. In order to minimise the FFT noise bandwidth no additional data windowing was performed. That is to say that the data was effectively multiplied by a uniform window resulting in a noise bandwidth identical to the resolution bandwidth.

After the calibration had been performed the residual noise floor was measured for increasing numbers of cross correlations. Fig. 5 details residual phase noise floor and acquisition time for each of these measurements. The final measurement of 100,000 cross correlations has an increased resolution bandwidth because the number of data points acquired in each frame was reduced in order to shorten the measurement time.

Fig. 5. Residual phase noise floor of the measurement system at 20 kHz offset.

Number of Cross Correlations	System Noise Floor at 20 kHz Offset (dBc/Hz)	Measurement time (Seconds)	Resolution Bandwidth (Hz)
100	< -185 dBc/Hz	73	7.63 Hz
1000	< -190 dBc/Hz	730	7.63 Hz
10,000	< -195 dBc/Hz	7300	7.63 Hz
100,000	< -200 dBc/Hz	3620	122.07 Hz

Fig. 6, Fig. 7 and Fig. 8 show plots of residual phase noise floor for 1000, 10,000 and 100,000 cross correlations respectively. The blue and red (upper) traces are the noise floors for each independent channel and the green (lower) trace is the dual channel cross correlated noise floor. It should be noted that due to the large variance of the measured noise the top of noise line was used to provide a conservative estimate for the noise floor. If we compare these three figures, the reduction in noise floor is clearly visible as the number of correlations increase. The phase noise floor is reducing by approximately 5 dB for every factor of 10 increases in the number of correlations and this is in good agreement with the theory. Unfortunately the close to carrier noise, at frequency offsets below 1 kHz, does not show the same level of suppression. This is thought to be a result of the high levels of spurs that are present in the 10 Hz to 1 KHz region.

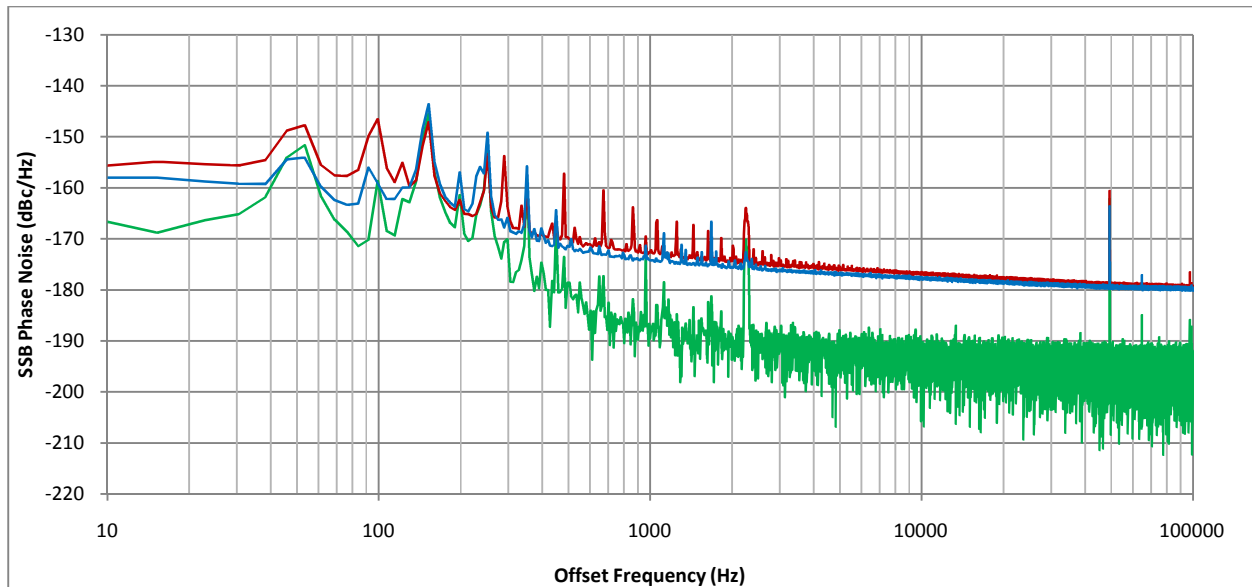


Fig. 6. Residual phase noise floor of the measurement system after 1000 cross correlations.

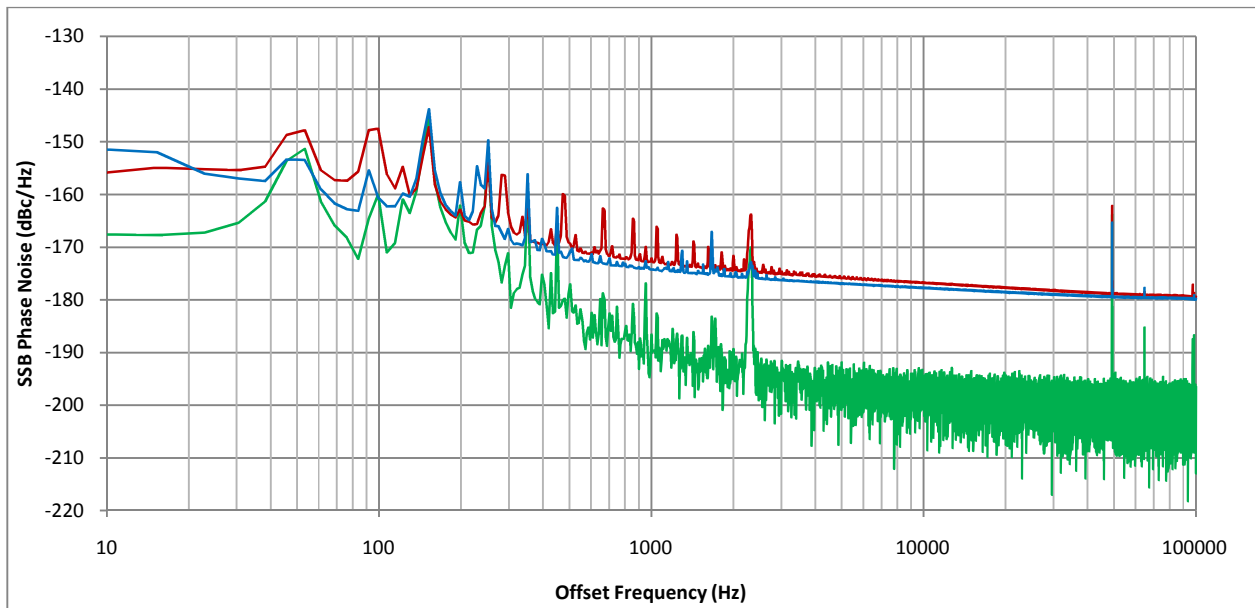


Fig. 7. Residual phase noise floor of the measurement system after 10,000 cross correlations.

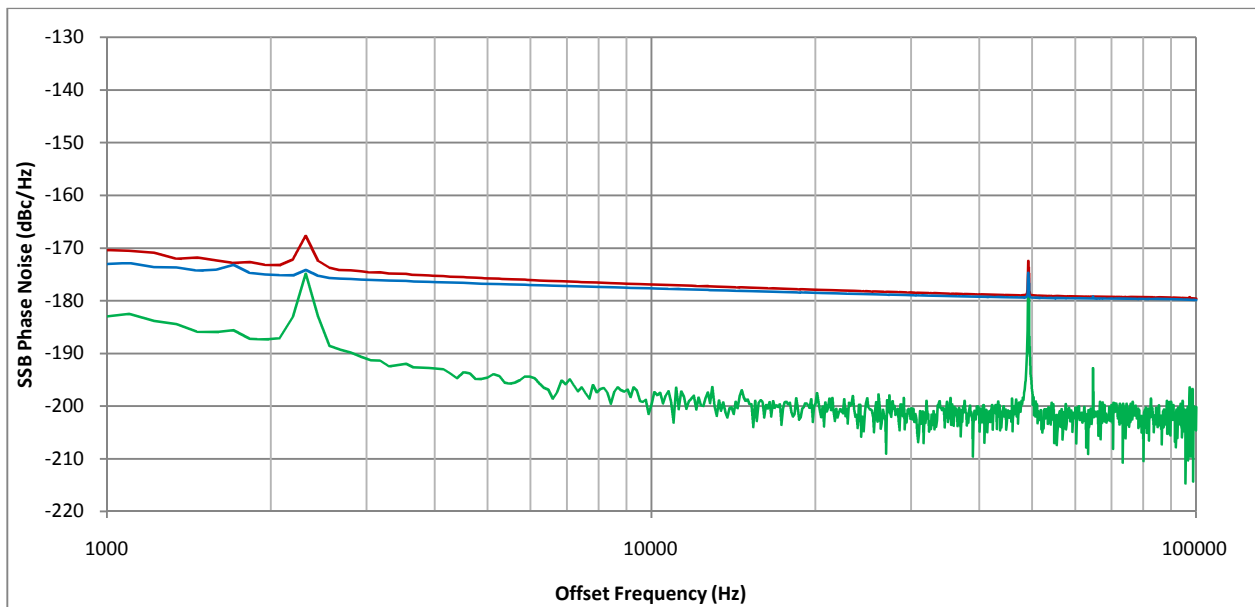


Fig. 8. Residual phase noise floor of the measurement system after 100,000 cross correlations. This measurement was made with an increased resolution bandwidth of 122.07 Hz in order to reduce the measurement time.

## AMPLIFIER MEASUREMENTS

A measurement of a 1.25 GHz medium power silicon amplifier has been performed, this amplifier had a noise figure of 8 dB. The amplifier was powered using batteries in order to reduce the potential for additional interference. A power level of 17.2 dBm was provided to its input and the theoretical far from carrier residual phase noise floor was calculated using (7) as -186.2 dBc/Hz. Fig. 9, Fig. 10 and Fig. 11 show plots of the amplifiers residual phase noise for 100, 1000 and 5000 cross correlations respectively.

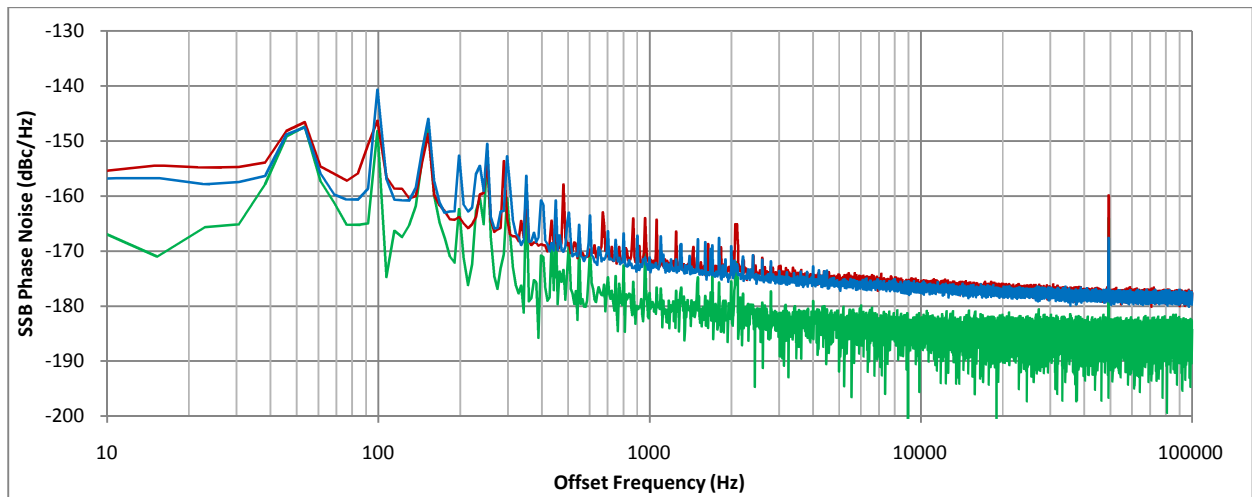


Fig. 9. Residual phase noise floor of a 1.25 GHz amplifier after 100 cross correlations.

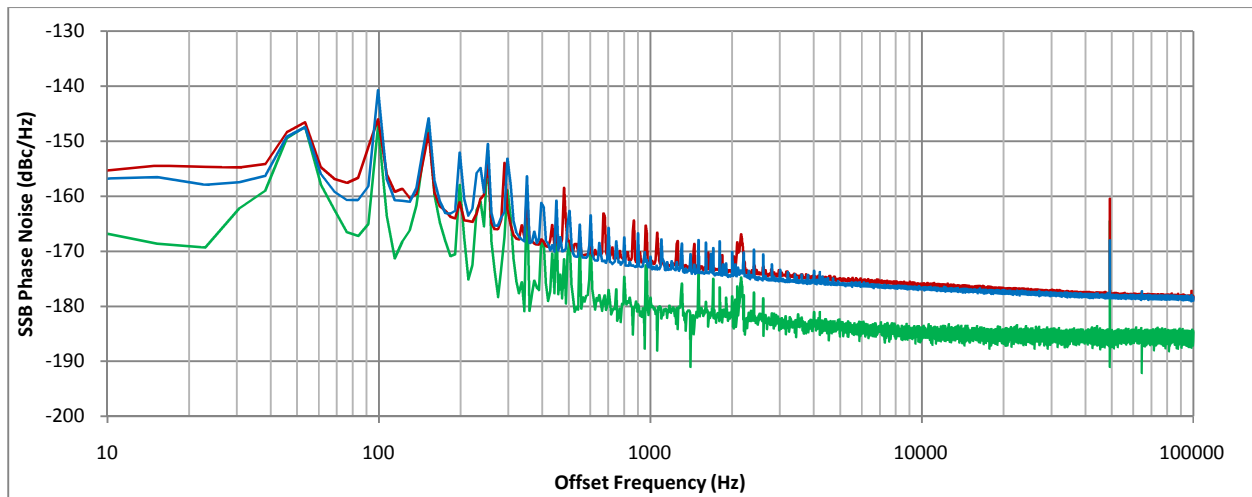


Fig. 10. Residual phase noise floor of a 1.25 GHz amplifier after 1000 cross correlations.

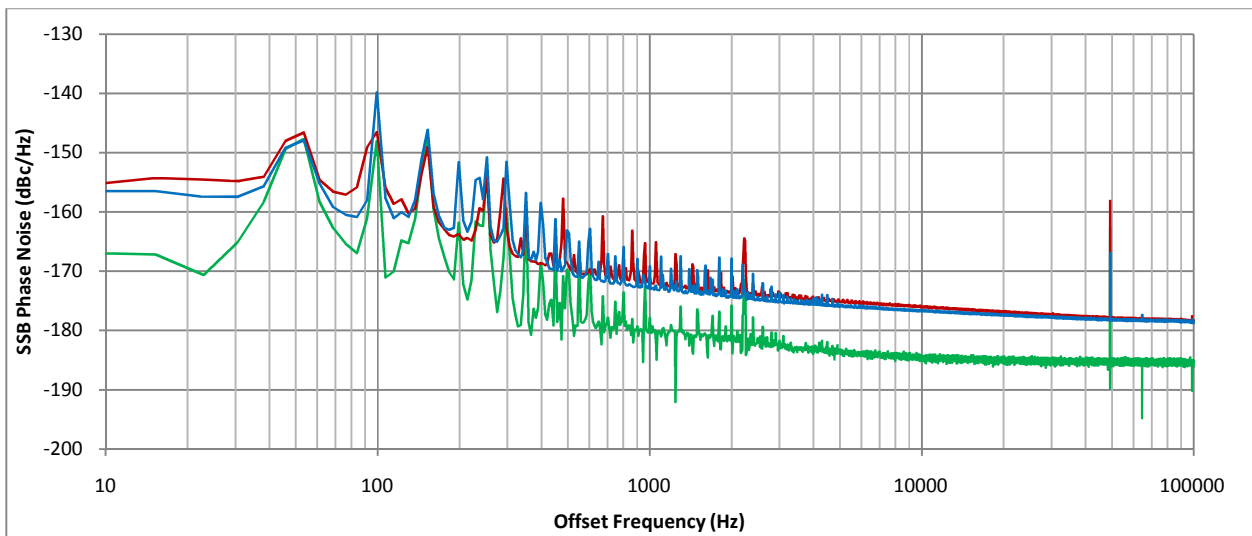


Fig. 11. Residual phase noise floor of a 1.25 GHz amplifier after 5000 cross correlations.

With reference to Fig. 9 it can be seen that after 100 correlations the measured noise still has a large variance. This is because the uncorrelated instrument noise is present in the measurement data. However, as the number of correlations increases it can clearly be seen that the measured noise is converging to an absolute value. At offsets above 10 KHz the residual phase noise is approximately -185 dBc/Hz, this is good agreement with the theoretical value of -186.2 dBc/Hz.

## CONCLUSIONS

A cross correlation residual phase noise measurement system has been constructed with a noise floor of -200dBc/Hz for 100,000 correlations. This is an improvement of 20 dB when compared with the same system operating with a single channel. No additional AM suppression was required to achieve this result. However, the reduction in noise floor comes at the expense of increased measurement time and system complexity.

## ACKNOWLEDGMENTS

We wish to thank BAE Systems, the Royal Academy of Engineering and the University of York for supporting this work. We would also like to thank the UK National Physical Laboratory (NPL) for the provision of one HP 11848A unit and the Visual Basic software for control of the HP 3048 phase noise measurement system. Finally we would like to acknowledge Dr. Bob Temple and Agilent for help and discussions regarding the circuit descriptions of the HP 3048 phase noise measurement system.

## REFERENCES

- [1] W. F. Walls, "Cross-correlation phase noise measurements," in *Proc. IEEE Frequency Control Symposium.*, 1992, pp. 257–261.
- [2] Hewlett Packard. (1989, Sept 01). *HP 3048A Phase Noise Measurement System Reference Manual* [online]. Available: <http://cp.literature.agilent.com/litweb/pdf/03048-90002.pdf>
- [3] E. Rubiola and F. Vernotte. (2010, Feb 27). *The cross-spectrum experimental method* [online]. Available: <http://arxiv.org/>, document arXiv:1003.0113v1 [physics.ins-det].
- [4] Hewlett Packard. (1990, Jun 01). *HP 3048A Phase Noise Measurement System Operating Manual* [online]. Available: <http://cp.literature.agilent.com/litweb/pdf/03048-61004.pdf>
- [5] *HP 11848A Phase Noise Interface Service Manual*, 1st ed., Hewlett-Packard Company., Spokane., Washington, 1987.
- [6] M. Sampietro, L. Fasoli, and G. Ferrari, "Spectrum analyzer with noise reduction by cross-correlation technique on two channels," *Rev. Sci. Instrum.*, vol. 70, no. 5, May 1999.